# Measurement of Light's Orbital Angular Momentum

Martin P.J Lavery, B.Sc

Submitted in fulfilment of the requirements for the Degree of Doctor of Philosophy

October 29, 2013

# Abstract

The desire to increase the amount of information that can be encoded onto a single photon has driven research in many areas of optics. One such area is the study of the orbital angular momentum (OAM) carried by a light beam. These beams have helical phase-fronts and carry an orbital angular momentum of $\ell\hbar$ per photon, where the integer $\ell$ is unbounded, giving a large state space in which to encode information. In the work that follows I discuss the development of new methods to measure the OAM carried by a light beam. An adaptation of a previously outlined interferometric technique is presented, resulting in a compact, robust measurement tool while dramatically reducing the number of degrees of freedom required for alignment. A new approach to sorting OAM is discussed, inspired by the simple example of the discrimination of plane waves focussed by a lens within direction space. This new approach is a telescopic system comprising two bespoke optical elements that transform OAM states into transverse momentum states; the various stages of development are outlined. Further to the development of this technique, investigations into the effects of misalignment and atmospheric turbulence on a communication link are presented. Outwith the area of optical communications, it is shown that by analysing the orbital angular momentum of light scattered from a spinning object we can observe a frequency shift many times greater than the rotation rate.

# Contents

# List of Figures

# List of Tables

# Acknowledgements

A Ph.D. in physics is seldom a solitary journey. Throughout the almost four years one spends completing their required body of work, many others help and support the process. I'm no different and would like to take this chance to thank the many people that have helped me on my journey over the last few years.

To the EPSRC and DARPA, for providing the funds, allowing me complete my studies.

To Miles, for his constant interest and support with my projects. He has opened up a countless number of amazing opportunities for me to travel, meet great scientists and conduct research that I have a real passion for.

To all my co-authors, your wide and intricate knowledge of many different fields has been integral to success of my Ph.D.

To the optics group, a truly wonderful collective of fun, smart and inspired people that have provided a great environment to work within. All the cake, present almost on a daily basis, is also pretty awesome.

To Graham, for being a constant backbone to most of the experimental research that is carried out in the optics group, teaching and supporting every member of the team.

To the MacRobertson, Milton-Chang, SPIE, and Mobility scholarships, that have allowed me to experience working in different research groups in both Europe

and the United States of America.

To my parents, for their constant love and support through all my levels of education, and for instilling in me a drive to work hard and attempt to succeed at what ever task is presented.

# Author's Declaration

I hereby declare that this thesis is the result of my own work, except where explicit reference is made to the work of others, and has not been presented in any previous application for a degree at this or any other institution.

Martin Philip John Lavery

# Publications

1. **Efficient Sorting of Orbital Angular Momentum States of Light**, G.C.G Berkhout, **M.P.J Lavery**, J. Courtial, M.W. Beijersbergen, and M.J. Padgett, *Physical Review Letters*, 105(15) (2010).

2. **Measuring orbital angular momentum superpositions of light by mode transformation**, G.C.G Berkhout, **M.P.J Lavery**, M.J. Padgett, and M.W. Beijersbergen, *Optics Letters* 36(10), 1863 - 1865 (2011).

3. **Measurement of the light orbital angular momentum spectrum using an optical geometric transformation**, **M.P.J Lavery**, G.C.G. Berkhout, J. Courtial and M.J. Padgett, *Journal of Optics* 13, 064006 (2011).

4. **Robust interferometer for the routing of light beams carrying orbital angular momentum**, **M.P.J. Lavery**, A. Dudley, A. Forbes, J. Courtial and M.J. Padgett, *New Journal of Physics* 13, 093014 (2011).

5. **Refractive elements for the measurement of the orbital angular momentum of a single photon**, **M.P.J. Lavery**, D.J. Robertson, G.C.G Berkhout, G.D. Love, M.J. Padgett and J. Courtial, *Optics Express* 20 (3), 2110-2115 (2012).

6. **Influence of atmospheric turbulence on optical communications us-**

**ing orbital angular momentum for encoding**, M. Malik, M. O'Sullivan, B. Rodenburg, M. Mirhosseini, J. Leach, **M.P.J. Lavery**, M.J. Padgett and R.W. Boyd, *Optics Express* 20 (12), 13195 (2012).

7. **Influence of atmospheric turbulence on states of light carrying orbital angular momentum**, B. Rodenburg, **M.P.J. Lavery**, M. Malik, M.N. O'Sullivan, M. Mirhosseini, D. J Robertson, P. Miles, and R. W Boyd, *Optics Letters* 37 (17), 3735-3737 (2012).

8. **Efficient measurement of an optical orbital-angular-momentum spectrum comprising more than 50 states**, **M.P.J. Lavery**, D.J. Robertson, A. Sponselli, J. Courtial, N.K. Steinhoff, G.A. Tyler, A.E. Willner, and M.J. Padgett, *New Journal of Physics* 15 (1), 013024 (2013).

9. **Efficient sorting of Bessel beams**, A. Dudley, T. Mhlanga, **M.P.J Lavery**, A. McDonald, F.S. Roux, M.J. Padgett, and A Forbes, *Optics Express* 21 (1), 165-171 (2013).

10. **Detection of a spinning object using light s orbital angular momentum**, **M.P.J. Lavery**, F.C. Speirits, S.M. Barnett and M.J. Padgett, *Science*, 341, 6145, 537-540, 2013.

11. **Direct Measurement of Quantum State Rotations**, M. Malik, M. Mirhosseini, **M.P.J. Lavery**, J. Leach, M.J. Padgett and R.W. Boyd, submitted for publication in May 2013.

"The important thing is not to stop questioning.

Curiosity has its own reason for existing."

— Albert Einstein

# 1

# The orbital angular momentum of light

Since the mid 19th century the fact that light beams can carry a momentum in addition to their energy has been recognised as a fundamental property of electromagnetic fields, described by Maxwell's equations [64]. This momentum means that when a light beam is absorbed by a surface, it exerts a radiation pressure, $P$, with a value $P = I/c$, where $I$ is the Irradiance of the incident light beam.

While studying Maxwell's equations, Poynting derived an expression for light

carrying angular momentum. Poynting considered the rotation of the electromagnetic field, which occurs for circular polarised light beams, comparing this rotation to the mechanical rotation of a revolving shaft, which suggested that circularly polarised light does also carry angular momentum. In his formulation he showed that the angular momentum to energy ratio is $1/\omega$, where $\omega$ is the angular frequency of the light [83]. Noting that this effect is small, Poynting himself felt that a mechanical observation would be extremely unlikely. It took until 1930s before an experiment was carried out by Beth, demonstrating this angular momentum in the laboratory [14]. He showed that circularly polarised light transmitted through a half waveplate caused it to rotate. Key to this experiment was that the waveplate was suspended from a quartz fibre to reduce the frictional forces. The rotation arose because the handiness of circularly polarised light was reversed by the waveplate, and hence the angular momentum was also reversed. This change in the light's momentum resulted in a torque on the waveplate, causing it to rotate.

These early works stem from a purely classical interpretation of a light beam, and do not require a quantised electromagnetic field. However, it is common for modern physicists to describe the interaction of light and matter in terms of photons rather then electromagnetic waves. One can quantify the momentum carried by a light beam as the momentum per photon, where the magnitude is expressed as $\hbar k$ and $\hbar$ for linear and angular momentum respectively. When the momentum and energy ratios above are considered, these quantised expressions lead to the same results as those obtained under the classical interpretation, known to Maxwell and Poynting.

In the quantum interpretation of a light beam, one can consider circular polarisation as arising from an individual photon spinning in either the left or right

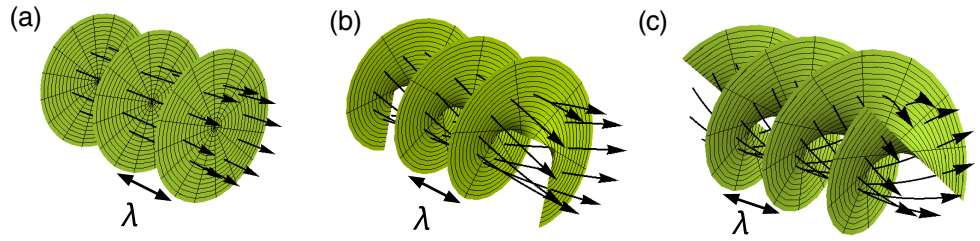


Figure 1.1: The local ray direction, shown as arrows, is perpendicular to the wave front, shown as a green surface, of a light beam. (a) For a beam with $\ell = 0$, all the vectors are parallel with the beam axis. For a higher order beam there is a azimuthal component to the Poynting vector, show for the case where (a) $\ell = 1$ and (c) $\ell = 2$. The angular deviation between $\ell = 0$ case and higher orders is the skew angle of the rays.

handed direction. Such spin is referred to as spin angular momentum, of value $\sigma\hbar$, where $\sigma = \pm 1$ depending on sense of circular polarisation. However, even in the 1930s there was indication that more complex momentum states could be carried by light. When considering photons, photons are produced during an atomic transitions, and for the case of dipole transitions the change in angular momentum is $\hbar$. Hence, emitted light that is circularly polarised is consistent with momentum conservation. In 1932 Darwin considered the case of higher order transitions where the momentum transfer is greater than $\hbar$ [27]. He suggested that in the case where the light is emitted a short radius away from the centre of mass of the atom, the linear momentum of the emitted photon would lead to an additional torque acting on the centre of mass. This extra angular momentum is what we would now call orbital angular momentum.

Beyond higher order transitions, in 1992 Allen *et al.*, while working in Leiden, considered the orbital angular momentum (OAM) present in Laguerre-Gaussian (LG) laser beams [1]. Laguerre-Gaussian beams are characterised by having helical

phase fronts which by necessity contain a phase singularity at their centre. These phase singularities had been studies since the 1970s when they were the subject of much research in both acoustic and optical fields [71, 13, 22, 6]. However, in none of these earlier work had the angular momentum associated with helically phased beams been identified. LG beams are described by two integer values $\ell$ and $p$, and in the waist plane of the beam has the complex amplitude

$$\Psi_{\ell,p}(r,\phi) = \quad C_{\ell p}\left(\frac{\sqrt{2}r}{w}\right)^{\frac{|\ell|}{2}} L_p^{|\ell|}\left(\frac{2r^2}{w^2}\right) \times \exp\left[\frac{-r^2}{w^2}\right] \exp\left[i\ell\phi\right], \tag{1.1}$$

where $w_0$ is the waist size, $L_p^{|\ell|}$ is the Laguerre polynomial for the variables $\ell$ and $p$, and $C_{\ell p}$ is the amplitude normalisation term [8, 2]. These two variables can take a wide range of values, as $\ell$ is unbounded and $p$ can be zero or take any positive integer value.

The key term in this complex amplitude is $\exp[i\ell\phi]$ determining the azimuthal phase profile of these beams. From Equation 1.1, one can derive expressions for the energy and momentum within such a beam, described by the spatially dependent form of the Poynting vector, see figure 1.1. Within a ray optical picture, the Poynting vector determines the direction of a local ray emanating from a particular position on the wave-front [82]. Helically phased beams have a skew of these local rays and each ray carries a linear momentum. When averaged over the whole beam, this linear momentum leads to an azimuthal component of the beams momentum that results in an angular momentum in the direction of propagation. If one considers the helical phase front, at a fixed radius, in azimuthal coordinates, it is simply a phase ramp of constant gradient. At a given radius from the beam axis, such a phase ramp has a base length of $2\pi r$ and a height of $\ell\lambda$, where $\lambda$ is the

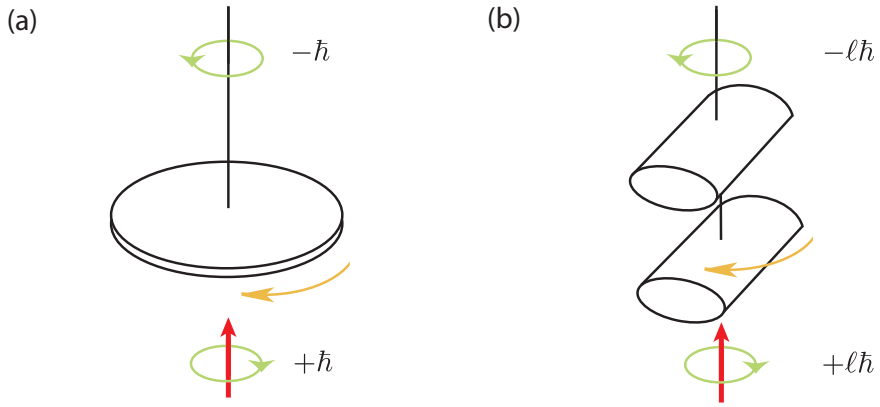


Figure 1.2: (a) Shows the rotational torque applied to a $\pi/2$ waveplate as circularly polarised light is transmitted through the plate as the polarisation state changes from left-handed into right-handed. (b) Suspended cylindrical lenses undergo a rotation when a helical beams is passed through the lenses as the OAM values is converted from $\ell\hbar$ into $-\ell\hbar$.

wavelength of the light, hence the skew angle of the local rays is

$$\beta = \frac{\ell\lambda}{2\pi r} = \frac{\ell}{kr}, \tag{1.2}$$

where $k$ is the wavenumber associated with the beam. If one considers the linear momentum, $\mathbf{P}$, carried by a single skewed local ray, incident on surface at an angle, $\beta$, the OAM carried by the beam is

$$|\mathbf{L}| = |\mathbf{r} \times \mathbf{P}| = |\mathbf{r} \times \hbar\mathbf{k}\sin\beta| = \ell\hbar. \tag{1.3}$$

Allen and colleagues reasoned that such beams carry an OAM to energy ratio of $\ell/\omega$, giving an OAM of $\ell\hbar$ per photon.

We note that unlike the spin angular momentum which has only two orthogonal values $\sigma = \pm 1$, OAM has a unbounded number of states described by $\ell$. However,

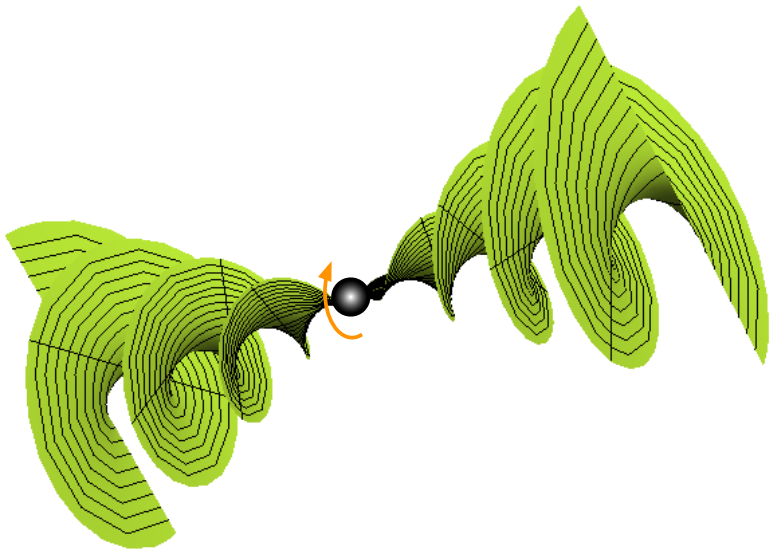

Figure 1.3: Focussed helically-phased beam trapping a dielectric bead. A partially absorbing bead absorbs the OAM resulting in torque.

one should also recognise that the low loss transmission of high OAM beam requires optical transmission systems with high Fresnel number.

An experiment, analogous to Beth's approach to measuring spin angular momentum, was postulated by Allen *et al.* where two cylindrical lenses are used to reverse the handiness of the phase profile, hence changing the momentum carried by the beam. Such a change in momentum, should result in a torque being applied to the lenses resulting in a rotational motion, figure 1.2. However, attempts to show this effect at the macroscopic level have proved challenging.

Even though the torque induced by orbital angular momentum is too small to rotate large objects, in the microscopic regime the story is quite different. Soon after the initial work by Allen *et al.*, He *et al.* considered the transfer of orbital angular momentum to trapped microscopic absorbing particles within optical tweezers (figure 1.3) [43]. Optical tweezers trap particles due to the intensity gradient in the

focused light beam. Due to this gradient force, dielectric particles are attracted to the centre of the region of high field strength, which then allows the trapping and movement of micro-scale particles [4]. When trapping particles using a helically-phased beam and with a beam waist similar to the size of the particle, the centre of attraction corresponds to the location of the phase singularity at the centre of the beam. These early studies into the torque applied by beams carrying OAM used black micron-sized CuO particles, which were seen to spin when trapped using a plane polarised LG beam. In later studies, the torque due to OAM was combined with that due to the spin angular momentum of circular polarised light and by changing the relative sense of the two components the particle's rotation could be sped up, slowed down or even stopped [37, 88].

Aside from the obvious mechanical uses of beams carrying OAM, one of the next key studies was the conservation of OAM during the process of second harmonic generation (SHG). In SHG a non-linear crystal effectively combines photons of a particular energy to generate a new photon with twice that energy. In this process it was observed that OAM is conserved such that the second harmonic output had twice the OAM of the input light [29]. Such second order processes, like SHG, are reversible. In the reverse of SHG the energy of a single pump photon is split into two new photons, a process called parametric down-conversion [17]. In 2001 Mair *et al.* tested the conservation of OAM for down-conversion, which is commonly used for the preparation of entangled photons [62]. The work by Mair *et al.* showed that one down-converted photon could take one of many $\ell$ values and when the OAM of this photon is summed with its entangled parter it showed that the OAM was conserved (figure 1.4). Their overall results were indicative of quantum entanglement, allowing investigations into this entanglement in higher

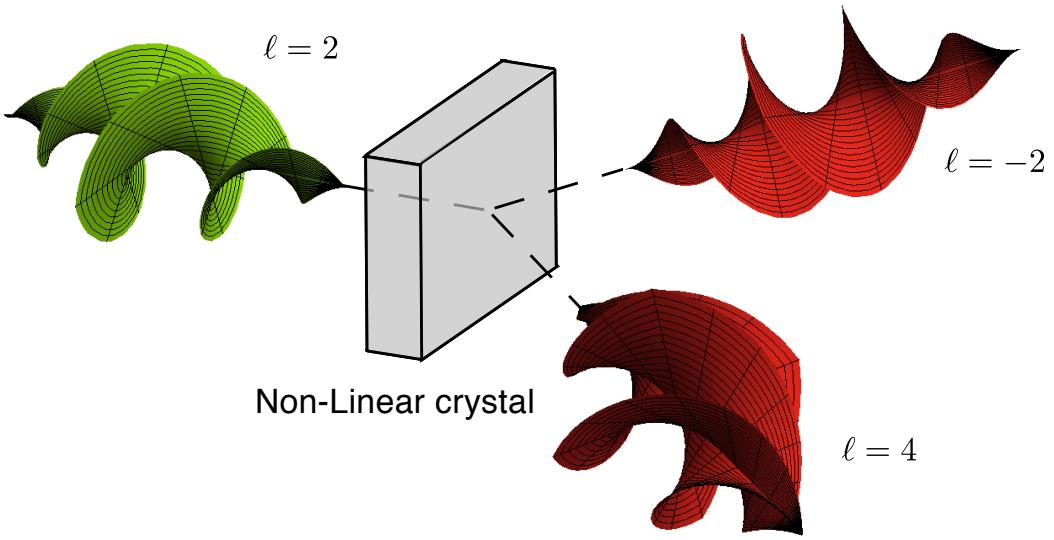


Figure 1.4: A photon carrying a particular OAM, when passed through a non-linear crystal the energy of that photon, will be split into two photons each with half the energy of the input photon. Momentum is conserved in this process, hence the sum of the OAM of both photons will be the OAM of the input photon. These photons can take one of many possible values, above the specific case of $\ell = 4$ and $\ell = -2$ is depicted.

dimensional Hilbert spaces.

Any state of complete polarisation can be described as a superposition of two orthogonal states of circular polarisation. A Poincaré sphere is a common method to visualise these superpositions, where the north and south poles correspond to left and right circularly polarised light. Linear polarisation is an equal superposition of left and right states, hence are represented around the equator of the Poincaré sphere, where the orientation of the linear polarisation is determined by the relative phase between the components in the superposition. An analogous sphere can be constructed for LG modes, for a two state subset of the unbounded LG state-space, where the north and south poles correspond to $\pm\ell$ respectively [78]. Equal superpositions of $\pm\ell$ result in petal type laser modes, where a change

of the relative phase of the component modes leads to rotation of the mode. This analogy between spin angular moment and OAM allows many tests of quantum mechanics, extensively studied for polarisation, to be generalised for subsets of OAM state-spaces.

The discrete and unbounded nature of OAM, where $\ell$ can theoretically take any integer value, has made this optical property an area of interest for many researchers attempting to transmit ever larger amounts of data across our optical communications networks [103]. Free-space links utilising OAM are currently receiving the most interest, where several schemes have already been developed [40, 99, 93], and more are likely to be developed in the near future. In 2004, Gibson *et al.* demonstrated the detection of eight modes over a range of fifteen meters, as at this range atmospheric turbulence only has a small effect on the mode quality of the transmitted beams [40]. For longer range links, compensation for atmospheric turbulence is an important consideration, as the OAM arises from the spatial phase structure of the beam and phase aberrations like those from turbulence degrade the mode quality [80, 97, 84, 81]. More recently Wang *et al.* presented a scheme using OAM multiplexing along with other more common methods of multiplexing to push the data rates for their link up to 2.56 Tbit $s^{-1}$ [99]. The use of OAM is also not limited to optical frequencies, as Tamburini *et al.* have demonstrated the use of specifically shaped radio antennas to increase the bandwidth of a radio link, with some promising results [93].

Researchers are not only considering OAM as a method to increase the bandwidth of communications links, it is also being seen as a method to make these links more secure. The larger alphabet which OAM provides, has the potential to increase the security of cryptographic keys transmitted with a quantum key dis-

tribution (QKD) system [16]. Groblacher *et al.* demonstrated such a QKD system using three OAM modes, known as qutrits, showing an increased coding density for enhanced security [41]. Malik *et al.* recently presented a scheme using eleven OAM modes, increasing the security further and considering the effect of atmospheric turbulence on such a system [63].

The importance of maintaining the spatial phase profile of these beams is a key concern when attempting to transmit light carrying OAM in free-space, or within optical fibre. Due to the inherent multimode nature of OAM beams and the requirement for high Fresnel number, one needs a fibre which has a large mode bandwidth. In most multimode optical fibre, the complex mode coupling which occurs essentially scrambles the input light as the energy of an incident input mode is coupled into other propagation modes supported by that fibre. However, teams at the University of St. Andrews, Friedrich-Schiller-University Jena and Lieden University are attempting over come the scrambling affects of multimode fibres [21, 20, 33, 60]. A different approach is being taken at Boston University, they are developing new type of optical fibre and have demonstrated propagation of three OAM modes in such a fibre over a length more than a kilometre [18]. Developments in OAM supporting fibre are sure to continue, and will potentially lead to OAM becoming an important method of high bandwidth multiplexing in future.

In this thesis I outline my contribution to the field of optics, specifically concentrating on the study of light's OAM. I have attempted to understand and resolve the remaining issues in the detection and transmission of OAM as a property for use within communications systems. Aside from communications inspired research, I will further present findings into the remote sensing of rotating bodies through the use of beams carrying OAM.

# 2

# The measurement of orbital angular momentum

As discussed in the previous chapter the orbital angular momentum (OAM) carried by light is seen widely as an extremely useful optical characteristic, with applications in many areas of optics. However, this advantage presents a greater challenge in the methods required to make a measurement, as the use of $N$ modes means there is an $N$ dimensional state space to be considered. The perfect detection of all the $N$ potential states is required to finally resolve this issue of measuring

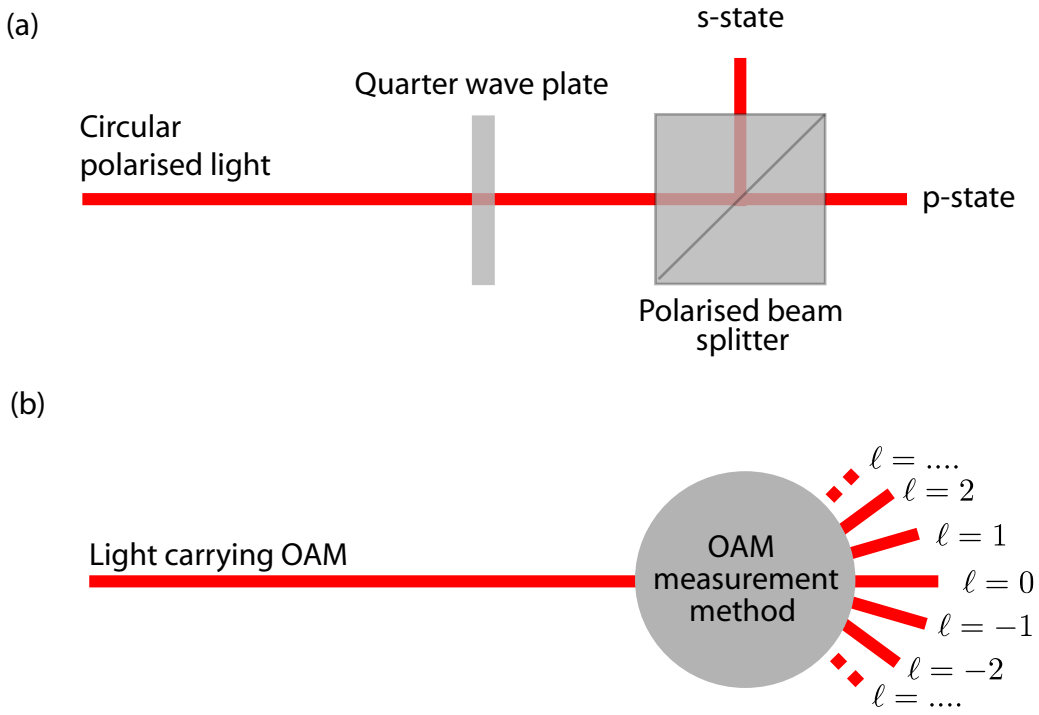


Figure 2.1: (a) A quarter-waveplate coverts circularly polarised light is into a linear state, the orientation of which is determined by the handedness of the original polarisation. A polarising beam splitter, transmits p-polarised light and reflects s-polarised light giving two outputs, allowing for the determination of the polarisation state. (b) A helically phased beam carries an OAM with a value of $\ell\hbar$ per photon. $\ell$, in principle, can take any integer value, offering a large range of potential outputs.

OAM. This issue is one yet to be completely resolved where the development of a simple and 100% efficient method for the measurement of OAM is desired.

In this chapter we will review the current methods which have been investigated for the measurement of OAM. These experimental techniques include measuring the torque applied to microscopic particles [43], counting the spiral interference fringes [77] and propagations through specifically chosen apertures [45, 9], among many others. All the current attempts have their strengths and weaknesses, how-

ever there has yet to be a simple solution as efficient as the polarising beam splitter is for measuring spin angular momentum (figure 2.1).

As discussed in chapter 1, He *et al.* considered the transfer of orbital angular momentum to trapped microscopic absorbing particles within optical tweezers (figure 2.2) [43]. Optical tweezers trap particles through the use of a force proportional to the intensity gradient in the focused light beam: dielectric particles are attracted to the regions of high field strength, which allows the trapping and movement of micro-scale particles [4]. When trapping using a helically-phased beam, with a beam waist similar to the size of the particle, the centre of attraction corresponds to the vortex location of the beam. The early studies into the torque applied by beams carrying OAM used black micron-sized CuO particles, which were seen to spin when trapped using a plane polarised LG beam. In later studies, the torque due to OAM was combined with that due to the spin angular momentum of circular polarised light [37, 88].

A dielectric particle will partially absorb the light incident on it, hence absorbing any angular momentum in either the form of SAM or OAM, resulting in a torque on the particle. In beams with a helical phase structure the torque applied acts in addition to the torque applied from circular polarisation. When simply considering the paraxial limit, the interaction with the particle is affected by both the polarisation and helicity of the beam, causing a torque

$$\Gamma = \frac{P_{abs}}{\lambda} \left( \ell + \sigma_z \right), \tag{2.1}$$

where $P_{abs}$ is the power absorbed by the dielectric bead, $\lambda$ is wavelength the light and $\sigma_z$ is the handedness of the polarised light. The application of torque to a

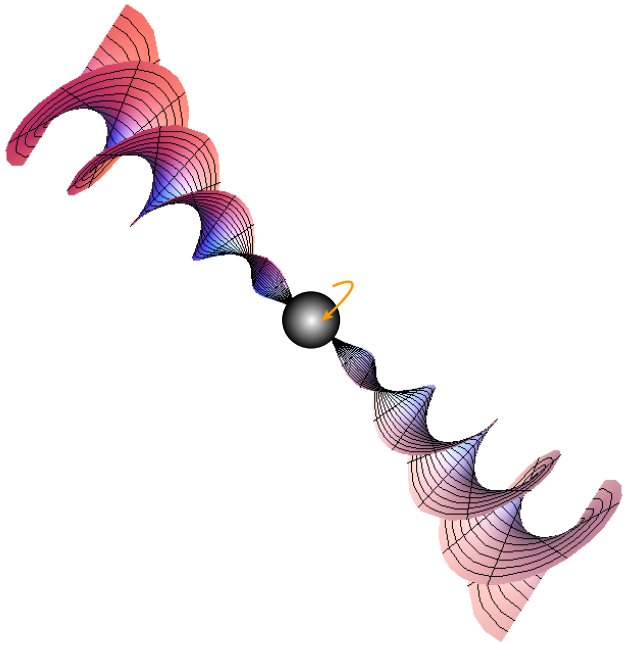

Figure 2.2: Focussed helically-phased beam trapping a dielectric bead. A partially absorbing bead absorbs the OAM resulting in torque.

particle is not restricted to the case of many incident photons, as every photon in the beam carries an OAM of $\ell\hbar$. The total torque applied to a particle, within the paraxial approximation, can be determined as the photon flux multiplied by the angular momentum of the helical beam. In the case of LG beams, the total angular momentum per photon is $(\ell + \sigma_z)\,\hbar$. It was shown by Simpson *et al.* that the torque due to OAM of $\ell = 1$ and that due to a polarisation of $\sigma = -1$ can cancel each other [88].

Particles trapped in optical tweezers are usually in a viscous material, normally water, which will cause a rotational drag resulting in slower spinning. In the simplest case, this drag is proportional to the angular velocity of the particle. A measurement of the optical torque can be made when an equilibrium of the rational drag and applied torque is reached. This measurement can be captured using a high speed digital camera or a photo diode at the edge of the trapped particle measuring a flashing as the particle spins. From this rotation and knowledge of the viscous medium, the torque is calculated and can then be used in equation (2.1) to calculate a measurement of the number $\ell$.

After the initial experiment by He *et al.*, beams carrying OAM have become useful as optical spanners [88] and many other tasks. This method can be used to determine the OAM of an unknown input beam through the measurement of the rotation speed, when the viscous drag of the liquid and polarisation state of the light are known [43]. However, this is not an optically efficient method to determine the OAM as it requires a high power laser source to cause a measurable rotation of the absorbing material.

As we have already mentioned, beams carrying OAM have a helical phase structure, one can reveal this structure through interference which will result in spiral

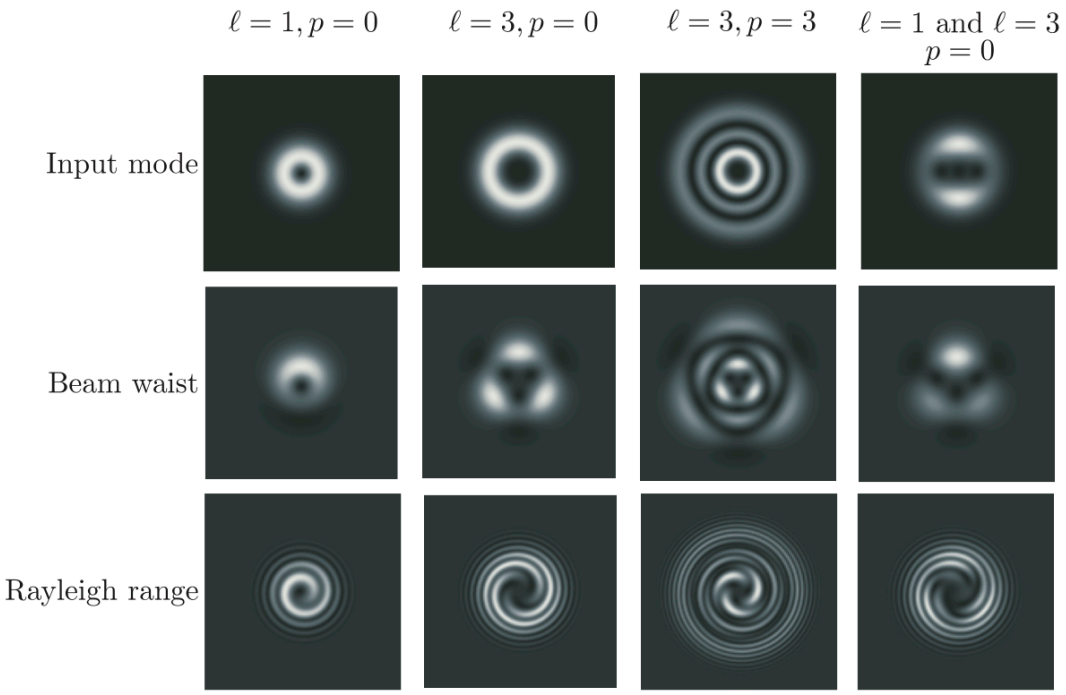


Figure 2.3: Interference of a LG beam (LG beams are examples of beams carrying OAM where $\ell$ is the azimuthal component and $p$ is the radial component) with a uniform plane-wave in the plane of the beam waist and at the Rayleigh range. These interferograms are shown for several input modes which contain helically phased modes with no radial component $p$ in rows one and two. Row three shows the effect of a mode containing radial lobes and in column four a superposition of two different helical phased beams.

fringes [77], see figure 2.3. This interference approach yields phase information of an input beam and can be used in many experiments, for example experiments involving speckle fields [75] and beams with offset vortex positions [90].

The basic principle behind this technique is simple: in a Mach-Zehnder or similar interferometer (shown in figure 2.4), a plane-wave reference beam is interfered with a co-linear helically-phased source beam. This co-linear path means that the observed fringes are purely a consequence of the relative phase structure of the source beam. When using a helically phased input, with a phase structure of

$\exp(i\ell\phi)$, each fringe corresponds to one step through $2\pi$ and by simply counting the number of these fringes the value $\ell$ can be determined, as seen in figure 2.3. The pattern observed is dependent on the curvature of the phase front; when the curvature is matched, petal patterns are observed, as seen at the beam waist, and when there is a difference in curvature spiral fringes are observed. In the case of Laguerre-Gaussian laser modes, the modes contain both a helical phase term $\ell$ and a radial term $p$, where the radial components are seen as radial nodes in the interferogram, the number of these is equal to $p + 1$, which is seen in column three of figure 2.3. Superpositions of Laguerre-Gaussian laser modes result in interleaved spiral fringes, seen in column four of figure 2.3.

Interferometric methods allow the OAM content to be easily determined. These are very useful techniques and have many applications, but due to the requirement to image the interferograms, they are not suitable for cases where small numbers of detected photons need to suffice.

The interference methods can be applied to more complex structures by generating a detailed phase map of the source. The areas of darkness within a interference pattern can lead to ambiguity about the phase value at this point, as this darkness maybe a result of lack of intensity as opposed destructive interference. Changing the phase of the plane-wave reference gives further information about these areas.

Each pixel in an image can be considered as an individual intensity measurement. An intensity reading is made for every pixel for each step in phase, usually 16 or 32 steps. When these steps are taken over a range of $2\pi$, the intensity of each point will change sinusoidally, the start point of this sinusoid represents the phase of that particular pixel (figure 2.4).

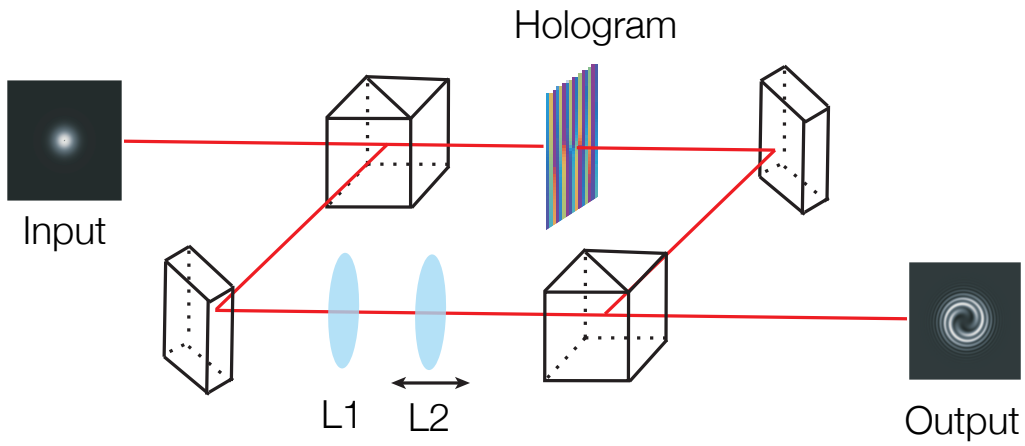


Figure 2.4: Schematic of a Mach-Zehnder type interferometer where a beam containing OAM is generated in one arm of the interferometer through the use of a hologram. The fringe pattern is changed from a petal pattern to a spiral fringe pattern by changing the distance between lens L1 and L2, as this alteration changes the curvature of the phase front in the reference arm.

Computationally this can be carried out very quickly, allowing for example the tracking of vortex positions in speckle fields, thereby enabling studies into the topology of vortex lines in these fields [12, 54, 73, 74, 75].

The requirement for a suitable reference beam places strict limitations on the areas where two-beam interference techniques can be used. For many cases where one would like to make a measurement of OAM, this is troublesome and in some cases impossible, for example in the detection of sources from astronomical objects.

A technique that does not require a reference beam is that of diffraction from apertures [45, 9]. A very elegant example of this was investigated by Hickmann *et al.*, where a helically phased beam incident on a triangular aperture results in a triangular lattice of constructive interference spots, the number and orientation of which is related to the $\ell$ value of the input (figure 2.6)[45]. This method can be modelled by considering the Fraunhofer diffraction pattern from the aperture, i.e.

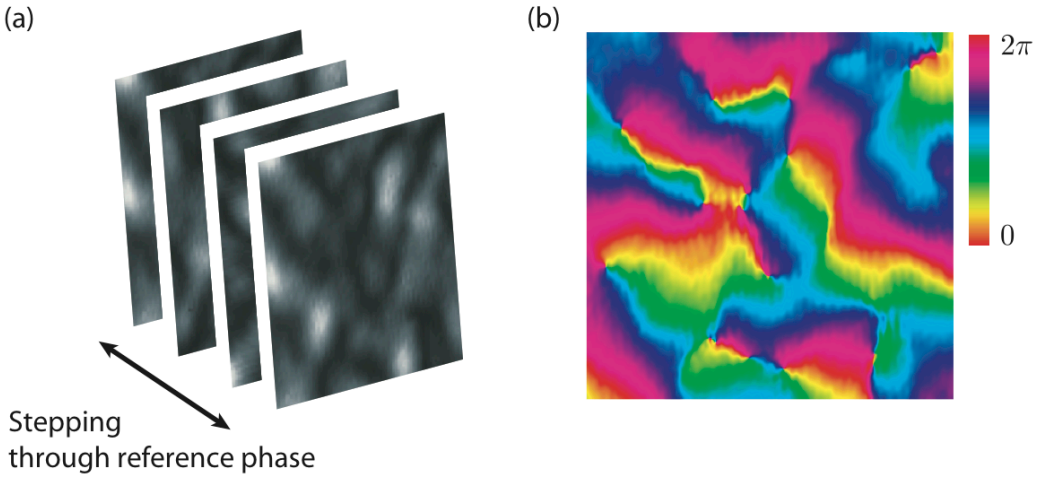


Figure 2.5: (a) A stack of intensity images where the phase of the reference beam changes in known steps of $2\pi/N$, allowing the phase of the intensity field to be determined. (b) Colour representation of the measured phase profile of a speckle field. Any phase change of $2\pi$ around a closed loop contains a vortex with topological charge $\ell = \pm 1$.

the squared modulus of the 2D Fourier transform of the amplitude in the transverse plane immediately behind the aperture.

This problem is not too distant from Fraunhofer diffraction being studied by undergraduates around the world, but had never been considered for beams containing a phase singularity. The observed interference effects arise from the light diffracted at the each side of the aperture, and in the case of helically-phased beams there is a change in phase along the edges of the triangle which is directly related to the $\ell$ value of the input beam. This detailed phase structure at the edge causes an interference pattern which is a function of $\ell$, where an increase in the mode index results in a new layer of spots within the interference pattern, as can be seen in figure 2.6. The triangular pattern is rotated with respect to the aperture. This rotation occurs due to the helical nature of the input mode and the direction of this rotation is reversed when the sign of $\ell$ is changed.

The use of a single aperture presents an elegant method to measure the OAM value of an input mode. This approach is not limited to the use of triangular apertures and has recently been shown to work with a hexagonal aperture, generating lines of constant intensity, the number of which correspond to the $\ell$ mode index of the input mode [59]. This method has also been used to measure fractional vortex charges [68], proving its effectiveness as a measurement technique.

An alternative aperture-based approach was independently developed by Berkhout *et al.*, using a circle of pinholes to generate diffraction patterns where their pattern structure depends on the input beam's mode structure [9] (figure 2.7). The positioning of these pinholes was inspired by the design of telescope arrays, to allow the detection of the OAM content of light from astronomical sources. These sets of pinholes are know as a multipoint interferometer (MPI). It was also shown

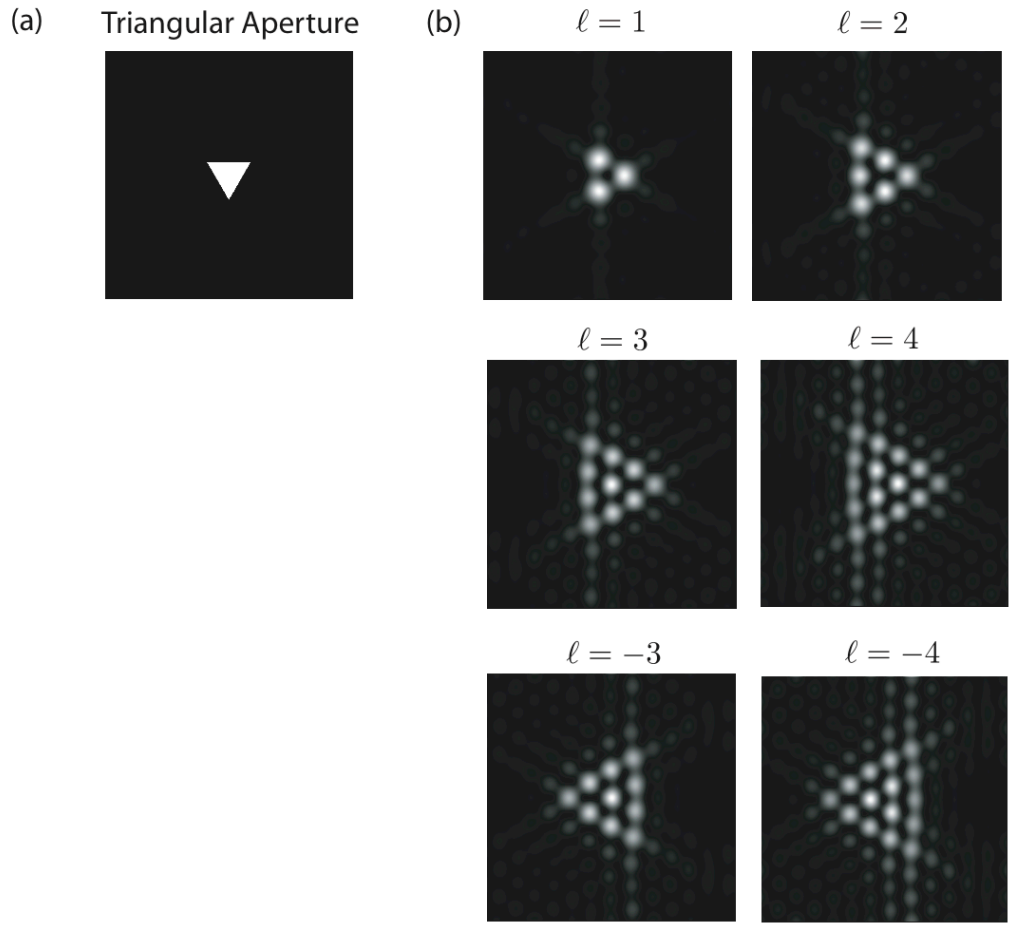


Figure 2.6: (a) Triangular aperture. (b) The far-field diffraction pattern generated by LG beams clipped by the aperture for various $\ell$ values. Simulated images to replicate the original results present by Hickmann *et al.* [45]

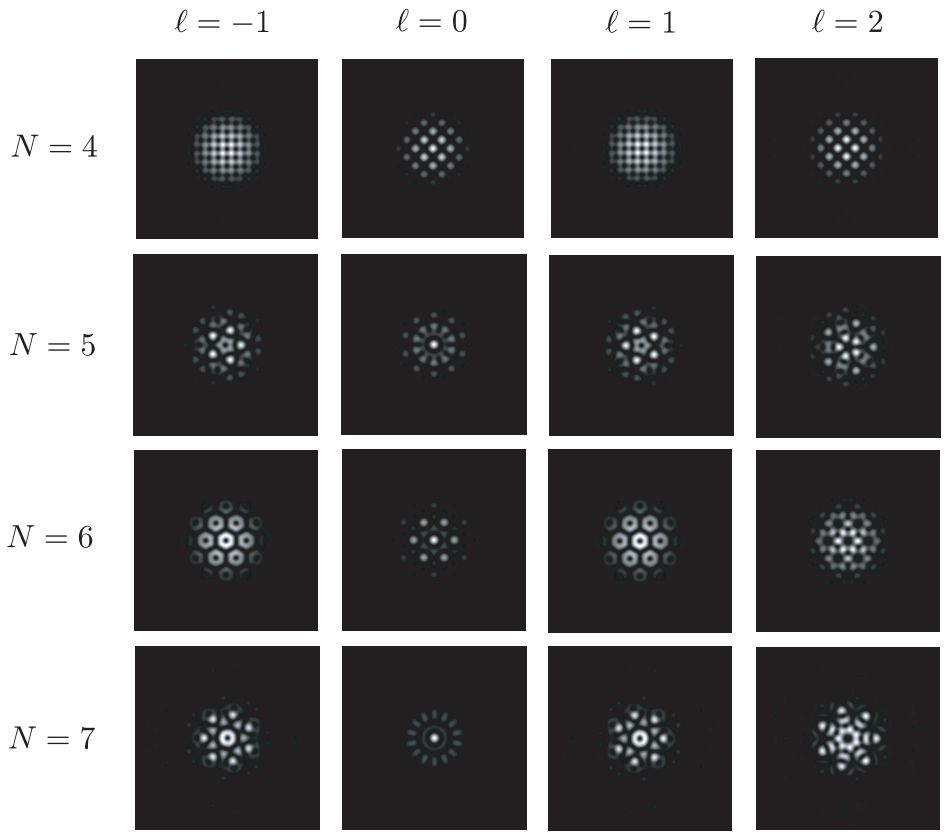


Figure 2.7: Diffraction patterns seen when a helically phased beam with topological charge is passed through a N-pinhole multi-point interferometer (MPI). Images courtesy of G.C.G Berkhout [9].

experimentally to measure the OAM state of partially coherent light [9].

The use of a set of pinholes illuminated with a beam with the vortex at the centre results in a sampling of the phase at fixed locations around the beam axis. Each pinhole can be considered to be a point light source. This again can be analysed by considering the Fraunhofer limit, yielding the far-field intensity pattern,

$$I_\ell^N \propto \left| \sum_{n=0}^{N-1} \exp(-i\ell\alpha_n) \times \exp\left( i\frac{ka}{z}(x\cos\alpha_n + y\sin\alpha_n) \right) \right|^2 \tag{2.2}$$

where $I_\ell^N$ is the far-field intensity of the MPI, $N$ is the number of pinholes, $k$ is the wave number, $a$ is the radius of the circle of pinholes and $\alpha_n = 2\pi n/N$ is the azimuthal co-ordinate of the $n$th point.

The ability of this approach to detect OAM is very dependent on the number of pinholes used, which can been seen in figure 2.7. This dependence can be understood in terms of the phase sampling that occurs at each of the pinholes. In the case of two or three pinholes, any phase difference between the pinhole positions in a helically phased beam could also simply be due to a suitably inclined plane-wave. This method is therefore only truly effective when four or more pinholes are arranged around the centre of the input mode's beam axis. In the specific case of four pinholes the MPI acts to distinguish between odd and even OAM states. The orientation of the diffraction patterns changes when inverting the mode index.

Either the Hickmann *et al.* or the Berkhout *et al.* aperture-based methods are a very attractive option when a simple solution for the measurement of the OAM content of a specific source is required. However, these techniques are based on pattern recognition for the determination of the mode index of the light, which is difficult to automate. These methods also require the use of a large number

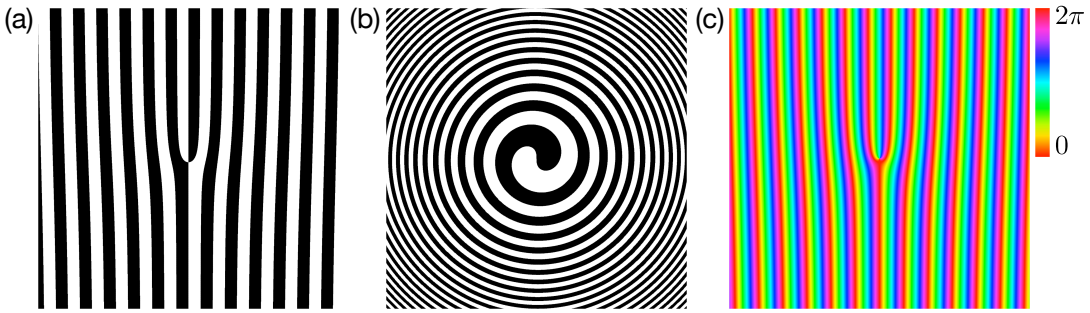


Figure 2.8: Three main types of holograms have been used to generate OAM. These types of hologram are (a) a blazed diffraction grating, (b) a spiral zone plate and (c) an unblazed hologram.

of photons in the same state to make a measurement of OAM and are therefore inherently inefficient processes to make such a measurement.

Optical systems, in general, will function in reverse, hence a method to generate OAM can be used as a method to measure OAM. In 1992, the generation of beams carrying OAM was first achieved through the use of a pair of cylindrical lenses [1]. Later Beijersbergen *et al.* developed helical phase plates [8] to do the same task. Prior to Allen and co-workers recognition of the OAM within helically-phased beams it was shown by Bazhenov *et al.* and Heckenberg *et al.* that computer-generated holograms could be used to generate beams containing phase singularities [6, 44].

Holograms have now become a standard tool for the generation of beams carrying OAM. In 1990, Bazhenov *et al.* took an approach based on a diffraction grating producing multiple orders with the desired phase structure [6]. These holograms can be understood as the phase of the product of the vortex term $\exp(i\ell\phi)$ and a phase-ramp term $\exp(ik\sin(\alpha)x)$, filtered ("blazed") such that points whose phase

is in the upper half of all possible phase values are coloured black, the remainder are coloured white (figure 2.8 (a)) . The effect of such a blazing is to distribute the phase into all possible diffraction orders. The $\ell$-forked pattern was inspired by the interference pattern between a beam containing a phase singularity and a tilted plane wave, producing this distinctive pattern [6].

In 1992, Heckenberg *et al.* focused on the concept of a spiral zone plate as the basis for the holograms they investigated. These spiral zone plates consisted of binary concentric circles with a singularity in the centre, which act in exactly the same way as a Fresnel zone plate but with a dislocation in the centre [44]. The number of interleaved circles defines the charge of the singularity generated. These zone plates can be understood as the phase of the product of the vortex term $\exp(i\ell\phi)$ and a lens term $\exp(ikr^2/(2f))$, blazed just like Bazhenov *et al.*'s phase patterns (figure 2.8 (b)). These gratings have proved effective in generating singularities, but they suffer from a lack of separation of the different diffraction orders.

In Bazhenov *et al.*'s approach, different diffraction orders travel in different directions, and can therefore be separated through Fourier filtering. The method, using unblazed holograms, has become one of the most common methods to generate vortex beams (figure 2.8 (c)). More recently the use of digital diffractive elements, in the form of spatial light modulators (SLMs) has allowed the interactive generation of beams containing singularities.

Mair *et al.* showed that this generating method can be reversed, coupling a particular diffraction order into a single mode fibre [61]. In this method the hologram, in combination with the fibre's entrance aperture, becomes a filter for OAM. It was used by Mair *et al.* to demonstrate the entanglement of the OAM of pairs

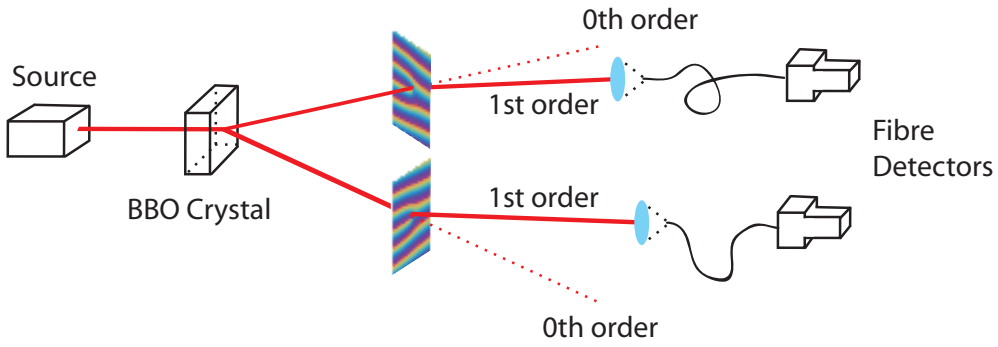


Figure 2.9: Schematic overview of the setup that is used to couple entangled photons from a BBO downconversion crystal which carry a specific OAM content. A photon with the correct $\ell$ value becomes a Gaussian mode in the first order, which then gives a reading at the fibre detector.

of photons produced from a non-linear crystal. This approach is currently extensively used for the detection of the OAM at the single-photon level quantum optics experiments [47, 56, 85, 32].

The concept was extended by Molina-Terriza *et al.* to couple multiple values of $\ell$ into multiple diffraction orders allowing for a larger bandwidth of detection [67]. However, this method requires many photons in the same state, as light can only be coupled into the fibre when the correct hologram is displayed. This restriction means that for an unknown helical beam, many holograms must be cycled through to test for the correct $\ell$ value.

OAM as a basis for high-bandwidth free-space communications has become an area of interest, with many researchers studying the stability of vortices through atmospheric turbulence. It is also seen a possible method to communicate with space-based receivers [80, 97]. Gibson *et al.* developed a free-space communicator based on two interleaved $\ell$-forked holograms generating a $3 \times 3$ grid of diffraction

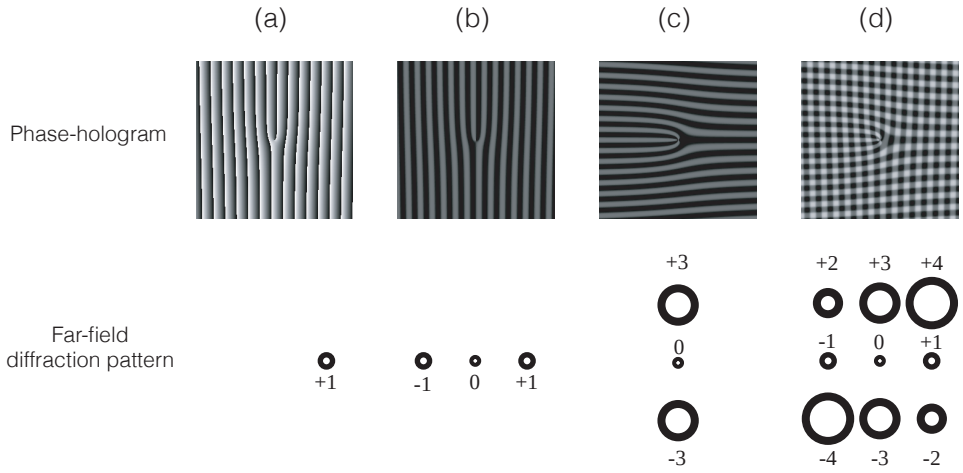


Figure 2.10: (a) A blazed $\ell$-forked hologram, which when illuminated with a Gaussian beam will generate an $\ell = 1$ beam in the first order. (b) The blazed hologram can be further optimised to give an equal power weighing to the first and negative first orders. (c) A rotation of $\pi/2$ radians gives the same rotation in the position of the diffraction orders, as shown above the charge can be increase to a higher $\ell$ (d) The modulo-$2\pi$ addition of the patterns shown in (b) and (c) gives the desired pattern of nine orders, generating a range of $\ell$-valued beams.

orders, each of which tests for a different $\ell$ of an incoming beam [40]. The system was shown to measure the OAM content for eight $\ell$ modes over a range of fifteen meters, and was also shown to measure superpositions of these eight modes.

This process of combining two diffractive phase elements, where each diffractive element corresponds to a different $\ell$ value, was outlined by Khonina *et al.* in 2000 [50]. The work by Gibson *et al.* is similar to that of Mair *et al.*, where a $\ell$-forked hologram converts an $\exp(i\ell\phi)$ beam into a beam with a planar phase-front. A hologram can be optimised to generate specific diffraction for positive orders. Gibson *et al.* made use of this effect by optimising the hologram to produce the $-1$,0, and 1 orders, see figure 2.10, giving $\pm\ell$ in the first and negative first orders, respectively, in the horizontal direction (figure 2.10 (b)). When a beam carrying

OAM is incident, this will allow the detection of the corresponding $\ell$ mode. The same optimisation process can also be achieved in the vertical direction, where the direction of the phase ramp is simply rotated by 90°. To allow the detection of many modes simultaneously, these two patterns were superimposed, resulting in each horizontal order having a number of vertical diffraction orders, such that the $\ell$ value of the orders are added. For example, if the positive first order of each hologram is $\ell = 1$, the first vertical order corresponding to the first horizontal order will have a value of $\ell = 2$, and the negative first vertical order corresponding to $\ell = 0$.

Using combinations of horizontal and vertical forks produces a grid of potential $\ell$ readings. When an input beam of the form $\exp(i\ell\phi)$ is incident on this pattern, a spot will appear in the centre of the diffraction order for which the $\ell$ values of the beam and the diffraction order add to zero (figure 2.11). It should be noted that the central grid location contains the original beam. Gibson *et al.* used this light for system alignment.

For any input the power of the input is spread evenly across all of the nine diffracted orders, hence the efficiency of the method scales with the reciprocal of the number of modes being detected. A superposition of $\ell$ modes can be determined as two or more bright central spots, the relative intensity of which determines the mode weighting in the superposition. The system was tested for several cases of a beam misalignment and use of a selective aperture, resulting in an observed spectrum of OAM [98, 35].

Gibson *et al.* showed the detection of eight modes over a range of fifteen meters, as at this range atmospheric turbulence only has a small effect on the mode quality of the transmitted beams. Beams carrying a vortex charge of $\ell = \pm 1$ are quite

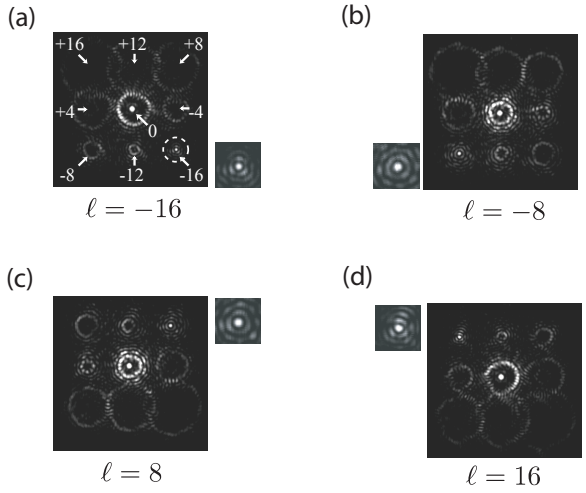


Figure 2.11: The far field observed when OAM modes with an $\ell = -16, -8, 8, 16$ are passed through a hologram similar to that shown in figure 2.10 (d). Images courtesy of G Gibson [40].

resilient to atmospheric distortion as a single-charge singularity cannot simply disappear. However, this is not the case for higher-order charges. Beams with an azimuthal index of $|\ell| > 1$ are highly sensitive to aberrations, which cause the collapse of a high-order singularity [24]. In optical communications reliant on high-order vortex beams, these atmospheric aberrations pose considerable concerns.

This interleaved hologram approach offers the ability to easily measure the OAM of many states simultaneously, and is relatively simple in its experimental implementation. However, the loss of a large proportion of the input light into other diffracted beams inherently makes this quite an inefficient detection method, unsuitable for single-photon measurements. In classical terms, beams carrying OAM do have the ability to increase the potential bandwidth of free-space communications but the effect of turbulence on the beams carrying the information currently limits the distance at which OAM could be transmitted in this way.

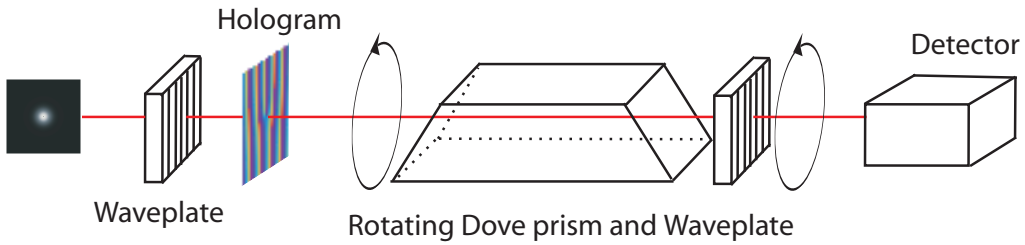


Figure 2.12: Experimental setup for the rotation of a mm-wavelength beam using a Dove prism.

The measurement of the Doppler effect is used as a method to determine the speed at which a light source is travelling. Garetz and Arnold [39] demonstrated that circularly polarised light experiences a frequency shift of $\Delta\omega = \sigma\Omega$, where $\sigma$ determines the handedness of the circular polarisation, when passed through a half wave-plate which is rotating at an angular frequency of $\Omega$.

Nienhuis [70] theoretically predicted that spinning of a cylindrical lens in a mode converter, at a frequency of $\Omega/2$, will result in a frequency shift in the beam of $\ell\Omega$. In 1998, Courtial *et al.* proposed an experimental method whereby spinning a beam carrying OAM at high speed will result in a Doppler shift in the observed frequency of a microwave source [23]. Specifically rotating a beam with an azimuthal profile $\exp(i\ell\phi)$ at an angular frequency $\Omega$ will result in a frequency shift of $\Omega\ell$.

Courtial *et al.* combined their earlier works with that of Garetz and Arnold [39]. This time, the beam (phase, intensity and polarisation) was rotated by a Dove prism in combination with a half-waveplate (figure 2.12). As a Dove prism is spun, this will cause a spinning of the beam where the transmitted intensity and phase rotate at twice the angular velocity of the prism. As discussed previously, a half-waveplate was used to rotate the polarisation vectors again at twice the angular

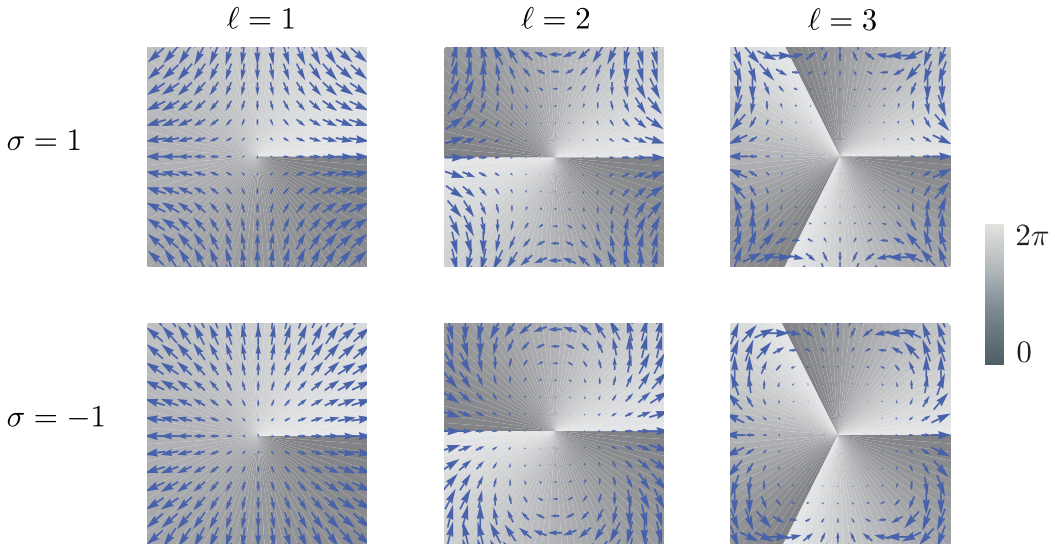


Figure 2.13: Vector plots of the transverse electric field.

velocity, resulting in the entire beam being rotated without any rotation of the source required. This effect results directly from the total angular momentum carried by the beam, defined as $J = \hbar(\ell + \sigma)$, giving a total frequency shift of $\Delta\omega = \Omega J$. When the difference in frequency was measured, it was found to closely match the prediction between clockwise and counterclockwise spin, of $\omega_{cw} - \omega_{ccw} = 2\Omega J = 2\Omega(\ell + \sigma)$.

The observed Doppler shift can be further understood through the consideration of the field distribution of the circularly polarised LG beams. A $(\ell + \sigma)$-fold rotational symmetry is seen in the field distribution, see figure 2.13, and for every $2\pi$ rotation of the beam the electric field undergoes a change of $\ell + \sigma$ cycles. The angular momentum will then, as expected, cause a change in the frequency of the spinning electric field.

A well-defined change in frequency suggests a method to accurately make a measurement of the OAM and SAM, as the change in frequency is well defined for

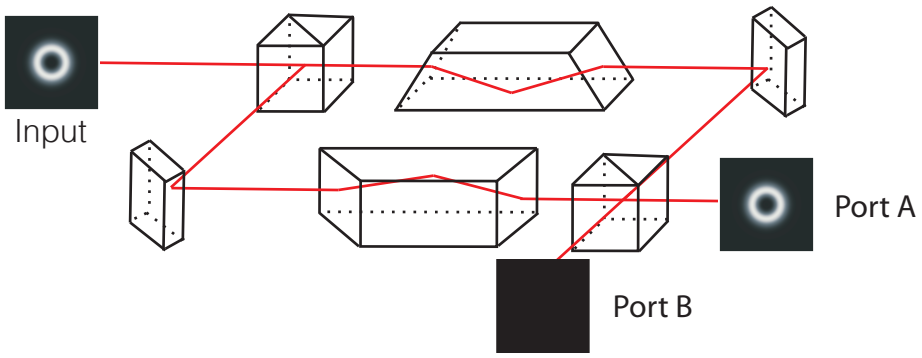


Figure 2.14: An experimental setup for a Dove prism interferometer. The layout is the same as a standard Mach-Zehnder interferometer, except a Dove prism is placed in each arm resulting in a rotation of the beam in one arm with respect to the other. This rotation will cause complete constructive interference in either port $A$ or $B$ depending on the input mode value.

a particular combination of OAM and SAM. The experimental procedure requires the high speed rotation of optical components which is challenging and not suitable for all circumstances. Vibrations induced by the mechanical rotation result in procession of the beam, this makes the effect much harder to observe at optical frequencies compared to microwave frequencies.

A method to sort OAM at the single photon-level was outlined by Leach *et al.* based on a Mach-Zehnder interferometer containing a Dove prism in each arm [58], see figure 2.14. This allowed for the sorting of beams with particular $\ell$ values into one of the output arms of the interferometer without any loss of the helical structure of the beams. The process is also theoretically 100% efficient. It was proposed that a cascaded set of such interferometers would allow the detection of many OAM states, but requires $N-1$ of them to do so, which is technically very challenging.

The key component in the interferometer is a Dove prism, which flips the

transverse cross section of any input beam [101]. An interferometer of this type is required to have complete constructive interference in one output port, $A$, and complete destructive interference in output port, $B$, for a particular OAM mode. When the two Dove prisms are rotated with respect to each other by an angle of $\pi/2$, the transmitted beam is rotated by an angle of $\pi$ and the relative phase difference between the two arms of the interferometer is $\Delta\psi = \ell\pi$ (figure 2.15). By appropriately adjusting the path length of the interferometer, constructive interference will occur in one of the two output ports for even $\ell$-valued states and in the opposite port for odd $\ell$-valued states. The light which is constructively interfered still carries OAM, allowing this light to be passed into a second interferometer to be further sorted.

The interferometer is not limited to sorting odd from even, as altering the angular rotation between each of the Dove prisms will change the modes which are sorted into the output ports $A$ and $B$. When the two Dove prisms are rotated by an angle of $\alpha/2$ with respect to each other, the beams transmitted through the two arms of the interferometer will be rotated with respect to each other by an angle of $\alpha$. For $\alpha = \pi/2$, the phase difference between the two beams is $\alpha/2 = \pi/4$ which means that modes with mode index $\ell = 0, \pm4, \pm8, ...$ go into port $A$ and beams with a mode index of $\ell = 0, \pm2, \pm6, \pm10, ...$ go into port $B$.

However, for the case of odd modes there is no net rotation of the Dove prisms that can sort the odd modes any further. To resolve this issue, Leach *et al.* proposed the use of a hologram at the odd output of the first stage which increases the $\ell$ value by $\Delta\ell = 1$, producing a beam with an even value of $\ell$. It was later proposed by Wei and Xue that this issue can be tackled by simply adjusting the path length in subsequent interferometers which has the same effect of adjusting

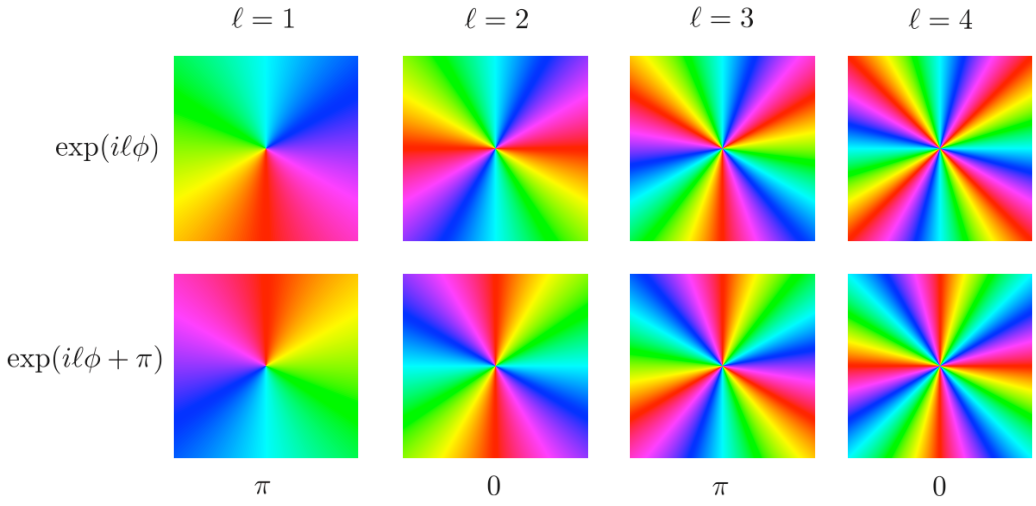


Figure 2.15: The phase profiles of several helical beams are shown in row one with no rotation and in row two a rotation of $\pi$. It can be seen that even modes will constructively interfere as the profiles are identical, and that odd mode will destructively interfere as the phase profiles are the inverse of each other.

the mode value from an odd to an even mode. This proposal allows the output mode from the stage-one interferometer to be further separated, allowing, in theory, any mode value to be determined [102].

This interferometric method presents a theoretically very efficient method for OAM measurement. However, the use of many cascaded interferometers is technically challenging. The use of just the first stage, the odd-from-even sorter, interferometer has been applied to demonstrate amplitude damping [31] and in the development of a linear optical CNOT gate for OAM [28]. The interferometric approach offers many advantages where the non-destructive sorting of OAM is required, such as a logic gate within Quantum Computing.

Even though the issues surrounding the measurement of OAM have not been completely resolved, many of the methods outlined in this chapter have proved themselves to be very useful for the task. It should be noted that this chapter

is not a complete treatise on the techniques that have been developed for the measurement of OAM. Methods converting OAM into SAM through the use q-plates, Principal Component Analysis, and decomposition of beams carrying OAM into basis set of Bessel beams, among others have had varying success resolving the issues surrounding the measurement of OAM [49, 89, 26, 69, 31]. An ideal solution is the development of the equivalent of a polarising beam splitter for OAM, giving 100% detection efficiency at the single photon level. The Dove-prism interferometer method outlined by Leach *et al.* is the only method that can reach this target theoretically. However, to measure OAM over a wide mode range using this approach is technically very challenging [58]. Spiral fringe interference patterns [77], and a hologram selector approach [61] are the most tried and tested methods, as these have been utilised by many, but each has its weaknesses.

# 3

# Robust interferometer for the routing of light beams carrying orbital angular momentum

In this chapter the development of a compact, robust interferometer to route OAM is discussed. The interferometer is an adaptation of a routing method, based on a Mach-Zehnder interferometer with a Dove prism in each arm, previously outlined by Leach *et al.* [58]. In this adaptation many of the previously required degrees of freedom are removed reducing the complexity of the device. This development of

this approach was carried out in collaboration with fellow graduate student Angela Dudley, where I developed the system design, following from this the experimental work and data collections was carried out jointly between us. Further support through the project was given by Johannes Courtial, Andrew Forbes and Miles J Padgett [52].

When the two Dove prisms are orientated with respect to each other by an angle of $\theta$, there is a relative phase difference between the two arms in the interferometer of $\Delta\psi = 2\ell\theta$ (figure 3.1 (a)). In the specific case of $\theta = 90°$, constructive interference will occur at one of the two output ports for even $\ell$-valued states and then for odd $\ell$-valued states in the other output port. In principle, this routing can be achieved with 100 % efficiency and with no loss of the input beams helical phase structure. It was proposed that a cascaded set of such interferometers would allow the detection of many OAM states, but requires $N-1$ of them to do so, but maintaining the alignment of many such interferometers has proved technically challenging, as discusses in chapter 2.

A previous attempt to make this interferometric technique more robust was outlined by Slussarenko *et al.* where they reconfigured the Mach-Zehnder interferometer as a Sagnac interferometer [89]. This approach reduces the number of alignment degrees of freedom within the interferometer, but requires additional polarisation optics.

The technique outlined by Leach *et al.* requires that the beams transmitted through each Dove prism are co-linear at the output of the interferometer ($BS_2$ in figure 3.1 (a)). This alignment was previously achieved by the accurate positioning of the Dove prisms, mirrors and beam splitters within the interferometer [58, 31, 28]. A Dove prism has a mirror plane, around which the transverse cross section

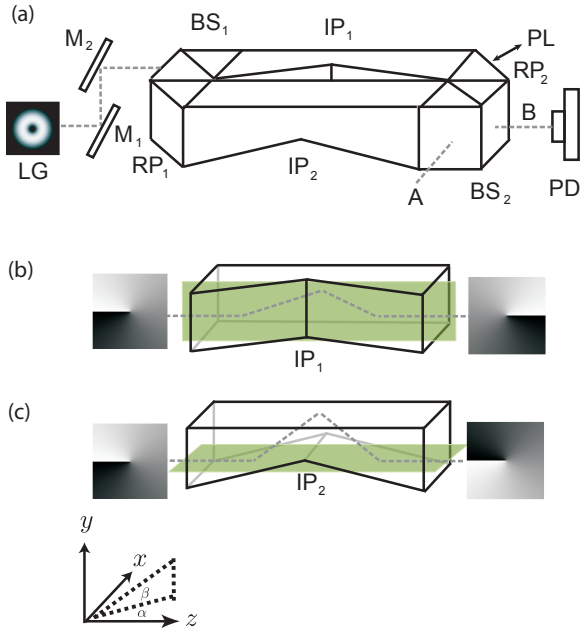


Figure 3.1: (a) Schematic of the robust odd-even OAM router (M: mirror, BS: beam-splitter, RP: right-angled prism, IP: inverting prism, PL: piezoelectric, A: output port A, B: output port B, PD: photo-diode). (b) and (c) illustrate the effect of the prisms on their own. It can be seen that the beams behind the two prisms are rotated by 180° with respect to each other. A Dove prism has a mirror plane, indicated in green, around which any transmitted beam is flipped.

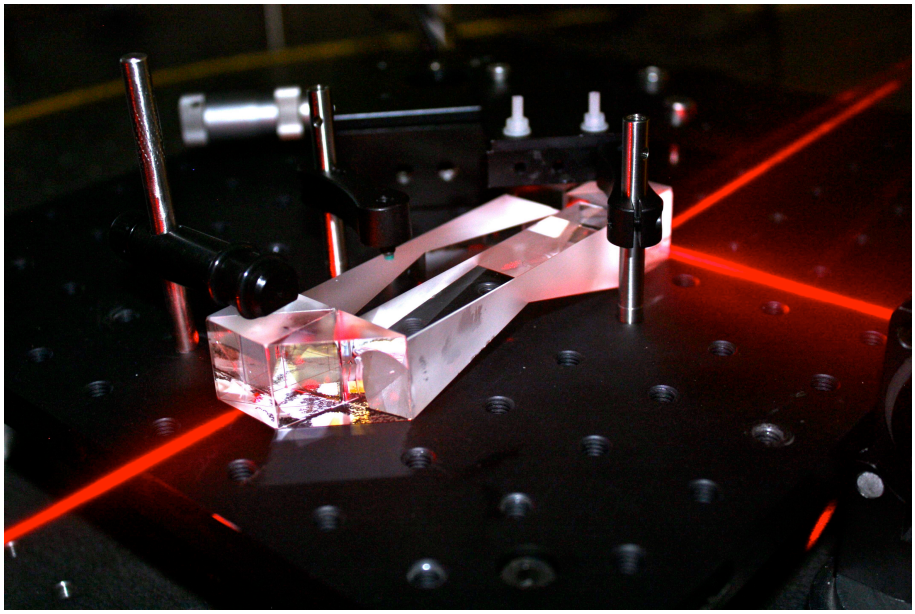

Figure 3.2: Image of the robust interferometer shown in figure 3.2 (a).

of any transmitted beam is inverted (figure 3.1 (b)). Considering these mirror planes, a different approach to alignment can be taken. The intersection of the mirror plane in each Dove prism defines the path an input beam is required to take for the two beams to be co-linear at the output ports, $A$ or $B$ in figure 3.1. Hence, by controlling direction of the input beam, the interferometer can be aligned without precise alignment of any of the constituent components. The requirement is that the whole beam is always contained within the aperture of the prisms. An additional fine control for the path length is required such that output beams completely constructively or destructively interfere at the one of output ports of the interferometer.

In our approach we use specially manufactured inverting prisms, previously discussed by Leach *et al.* [54]. The beam enters and exits each inverting prism at an optical face perpendicular to the optical axis. This allows for the introduction

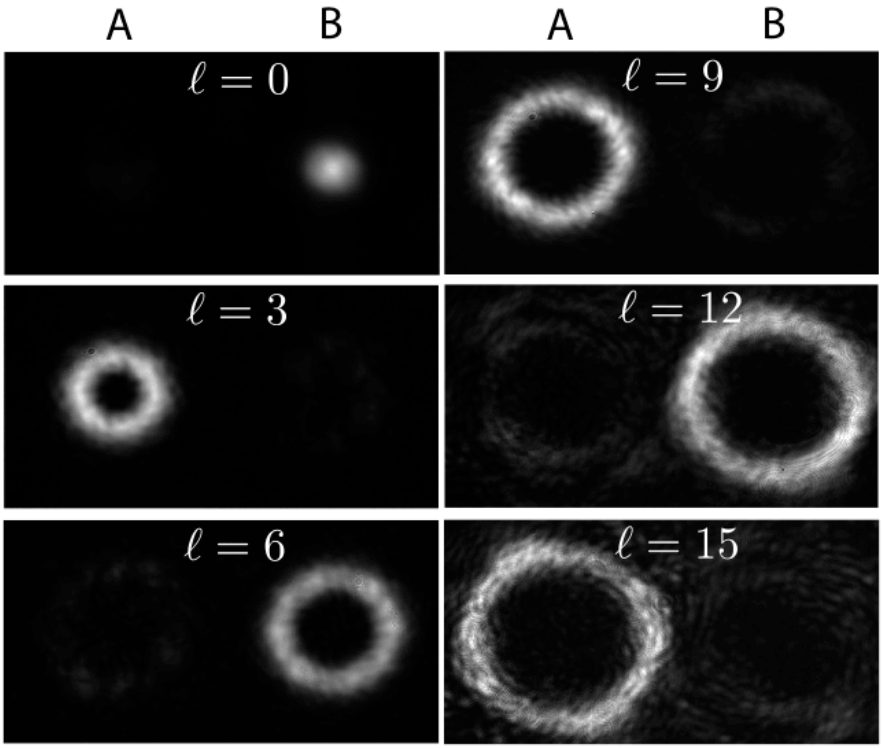


Figure 3.3: The interferometer routing odd and even helically-phased light beams into ports $A$ and $B$, respectively.

of right-angled prisms, as opposed to mirrors, meaning all optical surfaces can be bonded into a single, robust unit, shown in figure 3.1 (a).

We demonstrate the case of $\alpha = 90°$, for the sorting of even from odd values $\ell$-states. The intersection of the mirror planes from the prism $IP_1$ and $IP_2$, see figure 1 (b) and (c), was found through the use of external coupling mirrors, $M_1$ and $M_2$ in figure 1(a).

In our experimental implementation of the compact interferometer, we used Laguerre-Gaussian ($LG$) modes as our basis set of OAM. These modes were prepared by expanding a He-Ne laser beam to illuminate a $\ell$-fold fork diffraction

grating, encoded on a Spatial Light Modulator (SLM). To allow the precise control of constructive and destructive interference in the interferometer, the second right-angled prism, $RP_2$, was attached to a piezoelectric mount, giving fine control over the path difference within the interferometer. When the input mode is correctly aligned, the routing of odd and even $\ell$-valued $LG$ modes into the output ports $A$ and $B$, respectively is achieved. Experimental results are shown in figure 3.3. The large number of degrees of freedom previously required has been reduced to five degrees of freedom, position $(x, y)$ and tilt $(\alpha, \beta)$ of the input beam, and a small adjustment of the path length difference in the interferometer.

The performance of the interferometer in separating odd and even $\ell$-valued $\exp(i\ell\phi)$ modes was tested by measuring the intensity of the interference pattern in one of the output ports with a photodiode, while the path length of the interferometer was oscillated back and forth between constructive and destructive interference by driving the piezoelectric stage. The ability of the router to separate the input modes can be characterised by the fringe contrast [66]. The contrast is defined as $(v_{max} - v_{min})/(v_{max} + v_{min})$, where $v_{max}$ and $v_{min}$ are respectively the maximum and minimum measured voltages from the photodiode.

In our assessment of the performance of our interferometer we recognised that a potential limitation is imposed by the purity with which $\exp(i\ell\phi)$ modes can be produced by the SLM and associated optics. SLMs are themselves a source of aberration in the optical system since their flatness is typically specified at one or two optical wavelengths. In this experiment we used the central region of an optically-addressed SLM, which is typically flatter than the alternative technology, normally liquid crystal on silicon. Despite using the flattest of our SLMs and careful alignment of the associated optics, it is likely that residual aberrations will

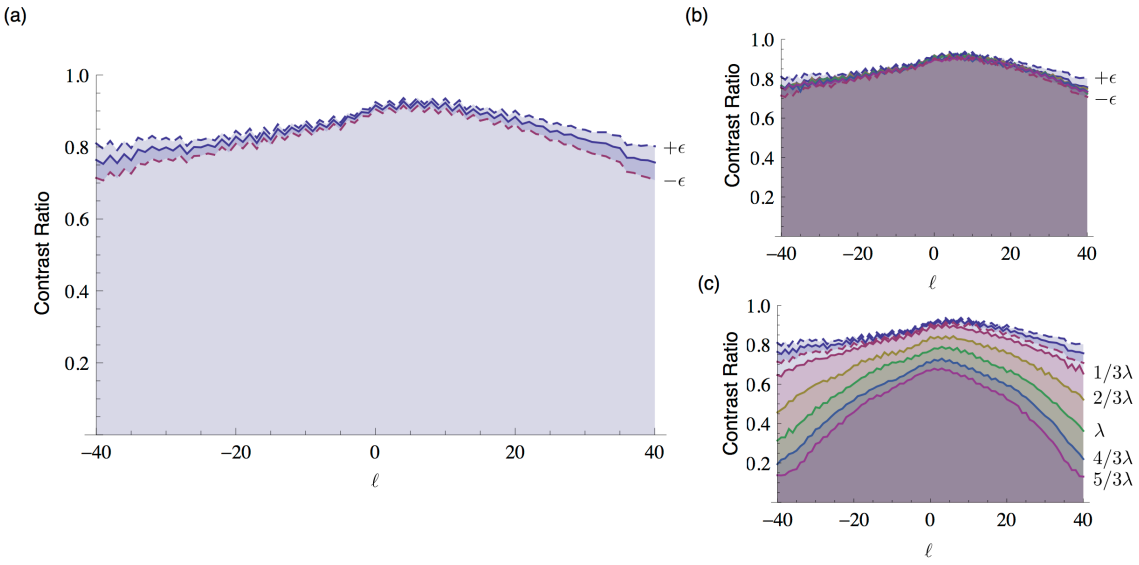


Figure 3.4: The contrast measured over the OAM mode range of $\ell = -40$ to $\ell = 40$, without, (a), and with, (b) and (c), additional aberrations. The error in the measured contrast ratio is determined by considering the standard deviation of the voltage received when no light is incident on the photodiode. In (b) and (c) for the effect of aberration on the contrast is shown for astigmatism and trefoil respectively. The magnitude of aberration was determined by the total phase height variation across the diameter of the beam incident on the SLM. The same magnitude of aberration was applied in the form of astigmatism and trefoil, with an approximate value of $1/3\lambda$, $1/3\lambda$, $2/3\lambda$, $\lambda$, $5/3\lambda$ and $4/3\lambda$, where $\lambda$ is the wavelength of the incident light.

lead to a degradation in the performance of the interferometer, especially at high values of $\ell$.

To investigate the effect of aberrations input modes over the range of $\ell = \pm 40$ were passed through the system with various degrees of additional astigmatism and trefoil aberrations which we encode on the SLM, see figure 3.4. For no additional aberrations, it was observed that for low values of $\ell$ the contrast is in the region of 90%, falling to around 75% at $\ell = \pm 40$. At these higher values of $\ell$ we note that trefoil aberration (figure3.4 (b)) has significantly more impact on the contrast than astigmatism. When an aberration is added to a beam carrying OAM, the beam is no longer a single $\ell$ valued mode and is instead a superposition of different $\ell$ valued modes, centred about the original value. As astigmatism is two-fold rotationally symmetric, the result in a superposition containing further modes with $\Delta\ell = \pm 2$, resulting in no observable degradation of the contrast obtained from the even/odd separation (see figure3.4 (b)). In comparison, trefoil aberrations are three-fold rotational symmetric resulting in a superposition containing further modes with $\Delta\ell = \pm 3$, and hence causing a noticeable degradation in the contrast of the even/odd separation.

Our development of a robust odd-even OAM router reduces the number of alignment degrees of freedom to simply those associated with the input light beam. Preserving the spatial structure of the input beam is important for many experiments, for example to demonstrate amplitude damping of Laguerre-Gaussian laser modes [31] and in the development of a linear optical CNOT gate for OAM [72, 28]. In each of these experiments interferometers similar to that outlined by Leach *et al.* were used, and would benefit from utilising a simplified routing technique similar to one presented in this chapter. One limitation with the method presented is that

it only routes odd and even modes to one of two outputs. To resolve this concern a change in the orientation angle $\alpha$ allows the routing of beams with different $\ell$ values into the two output ports [58]. Cascading multiple interferometers, with coupling mirrors between each stage, would allow the routing of a beam into one of many output ports where each corresponds to a different $\ell$ value of the input beam [58]. The routing of an OAM beam with the preservation of the helical structure is useful for data processes and transfer, as multiple gates can be used sequentially to carry out more complex operations on a input beam.

# 4

# Efficient Sorting of Orbital Angular Momentum States of Light

Interferometric sorting techniques, as discussed in chapters 2 and 3, are a photon efficient method of measuring the OAM carried by light [58, 52]. However, such approaches are technically challenging when the number of states one wishes to distinguish is large, as $N-1$ interferometers are required to distinguish $N$ states.

In an attempt to overcome this technical limitation, we were inspired by a com-

monly used optical element, a convex lens. A convex lens will readily discriminate tilted plane waves within direction space. Such a lens is all that is required to focus a plane wave to a spot in its focal plane, the transverse position depending on the transverse phase gradient of the plane wave. This allows multiple plane waves to be distinguished from each other using a detector array. The sorting of these transverse phase gradients suggests an approach for separating OAM states by transforming their azimuthal phase gradient, for which a change in mode index of $\Delta\ell = 1$ corresponds to an increment in $2\pi$, into a transverse phase gradient where a lens can then be used to distinguished the OAM state.

The key optical component in this approach is one that transforms azimuthal position in the input beam into a transverse position in the output beam, i.e. an optical element that transforms a helically-phased beam into a transverse phase gradient. This corresponds to the transformation of an input image comprising concentric circles into an output image of parallel lines. Mapping each input circle onto an output line gives the required deviation in ray direction and hence the phase profile of the transforming optical element. I discovered this type of transformation is an example of an optical geometric transformation which has been previously studied in the context of optical image processing [19]. This previous work outlined that a geometric transformation can only be implemented by a single optical element if the mapping is conformal. Taking $(x, y)$ and $(u, v)$ as the Cartesian coordinate systems in the input and output plane, respectively, for a mapping $(x, y) \mapsto (u, v)$ to be conformal it must meet the requirement

$$\frac{\partial u(x,y)}{\partial y} = \frac{\partial v(x,y)}{\partial x}. \tag{4.1}$$

An initial educated guess of the required transformation is from rectangular to polar coordinates, where $u(x,y) = r = \sqrt{x^2+y^2}$ and $v(x,y) = \theta = \arctan(y/x)$. However, such a transformation is not conformal as

$$\begin{aligned} \frac{\partial u(x,y)}{\partial y} &= \frac{\partial}{\partial y}\left(\sqrt{x^2+y^2}\right) = \frac{x}{\sqrt{x^2+y^2}}, \\ \frac{\partial v(x,y)}{\partial x} &= \frac{\partial}{\partial x}\left(\arctan\left(\frac{y}{x}\right)\right) = \frac{x}{x^2+y^2} \end{aligned} \tag{4.2}$$

and hence,

$$\frac{\partial r}{\partial y} \neq \frac{\partial \theta}{\partial x}. \tag{4.3}$$

It was required that the azimuthal phase gradient to be correctly mapped to a transverse phase gradient, therefore $v(x,y) = a\arctan(y/x)$. However, for the mapping to be a conformal mapping we require $u(x,y) = -a\ln(\sqrt{x^2+y^2}/b)$, known commonly as a log-polar transformation [86, 46]. Using the stationary phase approximation one can calculate the phase hologram that will map a point $(x,y)$ to a point $(u,v)$ in the Fourier transformed plane of that phase hologram [19]. Such a hologram can be obtained by solving the differential equations,

$$\begin{aligned} u(x,y) &= \frac{f}{k}\frac{\partial \phi_1(x,y)}{\partial x}, \\ v(x,y) &= \frac{f}{k}\frac{\partial \phi_1(x,y)}{\partial y}, \end{aligned} \tag{4.4}$$

where $k = \frac{2\pi}{\lambda}$ is the wavenumber, $\lambda$ is the wavelength of the light and $f$ is the focal length of the lens. The phase profile of the transforming optical element is then given by

$$\phi_1(x,y) = \frac{2\pi a}{\lambda f}\left[y\arctan\left(\frac{y}{x}\right) - x\ln\left(\frac{\sqrt{x^2+y^2}}{b}\right) + x\right], \tag{4.5}$$

where $\lambda$ is the wavelength of the incoming beam, and $f$ is the focal length of the Fourier-transforming lens. The parameter $a$ scales the transformed image to fill the output aperture in the $v$-direction, we choose $a = d/2\pi$, where $d$ is the width of the aperture of the phase profile. $b$ scales the transformed image in the $u$ direction and can be chosen independently of $a$.

However the resulting variation in optical path length means that the transformation introduces a phase distortion that needs to be corrected by a second element. The transforming system therefore comprises two custom optical elements, one to transform the image and a second, positioned in the Fourier plane of the first, to correct for the phase distortion.

The required phase distortion can be determined by calculating the far-field amplitude profile of a plane wave that has been passed through the first optical element. This amplitude was calculated by collaborator Gregorius Berkhout, through again, the use of the stationary phase approximation; it is given by

$$a_2(u,v) = \exp\left(i\phi_1(x,y) - i\frac{2\pi}{\lambda f}(xu+yv)\right)\frac{2\pi}{\sqrt{\left|\frac{\partial u}{\partial x}\frac{\partial v}{\partial y} - \left(\frac{\partial u}{\partial y}\right)^2\right|}}. \tag{4.6}$$

The second optical element, $\phi_2(u,v)$, that corrects this distortion is simply the inverse of the phase profile of $a_2$. Hence, $\phi_2 = -\arg a_2$, giving

$$\phi_2(u,v) = -\frac{2\pi ab}{\lambda f}\exp\left(-\frac{u}{a}\right)\cos\left(\frac{v}{a}\right), \tag{4.7}$$

where $u$ and $v$ are the Cartesian coordinates in the Fourier plane of the first element. Figure 4.1 (a) and (b) show the phase profiles of the transforming and

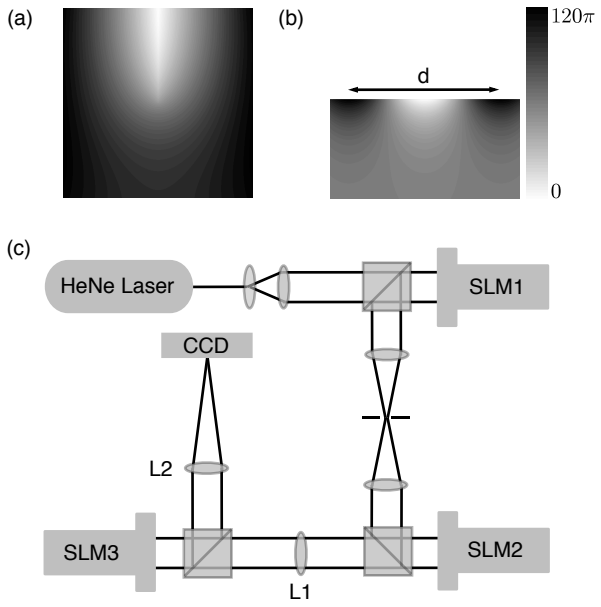


Figure 4.1: Phase profiles of (a) the transforming and (b) the phase-correcting optical element; d is the width of the aperture of the phase profiles. In (b) only that part of the phase-correcting element that is illuminated by the transformed beam is shown. In the experiment, the phase profiles are displayed on the spatial light modulators (SLMs) with $2\pi$ phase modulation. (c) Schematic overview of the setup. We use SLMs to both generate Laguerre-Gaussian beams (SLM1) and create the desired phase profiles for the transforming and phase-correcting optical elements (SLM2 and SLM3, respectively). L1 is the Fourier-transforming lens and L2 focusses the transformed beams. We use beamsplitters to ensure perpendicular incidence on the SLMs.

phase-correcting optical element, respectively. One can see that the transforming optical element contains a knife edge, corresponding to the "cut" point where the symmetry of the input beam is broken. The end of this line, i.e. the centre of the phase profile, defines the axis around which the OAM is measured.

A lens is inserted after the phase-correcting element to focus the transformed beam, which now has a $2\pi\ell$ phase gradient, to a spot in its focal plane. In the plane of this lens, the transformed beam is rectangular, meaning that the diffraction-limited focal spot is elongated in the direction orthogonal to the direction in which

the spot moves. The transverse position of the spot changes as a function of $\ell$ and is given by

$$t_\ell = \frac{\lambda f}{d}\ell. \tag{4.8}$$

I used diffractive spatial light modulators (SLMs) to create the desired phase profiles. For monochromatic light, an SLM can be programmed such that any desired phase profile is applied to the first-order diffracted beam, limited in complexity only by the spatial resolution of the SLM. Figure 4.1 (c) shows a schematic overview of the optical system. I use Laguerre-Gaussian (LG) beams as our OAM states. The first SLM, programmed with both phase and intensity information [85], was used to generate any superposition of LG beams. Using relay optics and an aperture to select the first-order diffracted beam, this input state is directed onto the transforming element, displayed on the second SLM, which performs the required geometrical transformation in the back focal plane of the Fourier-transforming lens. The value of $a$ in equation 4.5 was chosen such that the transformed beam fills 80% of the width of the phase corrector in order to avoid diffraction effects at its edges. A third SLM is used to project the phase-correcting element. The diffracted beam from this SLM has a transverse phase gradient dependent on the input OAM state. These direction states are focussed onto a CCD array by a lens and, as discussed above, the lateral position of the resulting elongated spots is proportional to the OAM state of the incident beam.

Figure 4.2 shows the modelled, observed phase, and intensity profiles at various places in the optical system for a range of OAM states. The modelled data is calculated by plane wave decomposition. In the second column, one can see that an input beam with circular intensity profile is unfolded to a rectangular intensity

profile with a $2\pi\ell$ phase gradient. As predicted, the position of the elongated spot changes with the OAM input state. I recorded the output of the mode sorter for input states between $\ell = -5$ and $\ell = 5$. The experimentally observed spots are in good agreement with the model prediction. Moreover, our system allows us to identify a superposition of OAM states, as can be seen in the final row of figure 4.2, where an equal superposition of $\ell = -1$ and $\ell = 2$ gives two separate spots in the detector plane at the position of $\ell = -1$ and $\ell = 2$. It can be seen that the spots are slightly broader than the modelled ones, which is due to aberrations introduced by the optical system.

To directly measure the state of any input beam, I defined eleven equally sized rectangular regions in the detector plane, all centred around one of the expected spot positions for the eleven input modes used in the experiment. By measuring the total intensity in each of these regions, I could determine the relative fraction of a specific OAM state in the input beam. Figures 4.3 (a) and (b) show the results for eleven pure input states, both modelled and observed, as shown in the third and fourth column of figure 4.2, respectively. Since the spots for two neighbouring modes slightly overlap, some of the light in a mode leaks into neighbouring regions, i.e. there is some cross talk between different modes. This cross talk shows up as the off-diagonal elements in figure 4.3. As described before, our experimental results show slightly broader spots than the modelled data and hence the off-diagonal elements are slightly greater then zero. It is, however, still possible to determine the input state of the light beam.

A commonly used measure to quantify the amount of cross talk between channels is the channel capacity, which is the maximum amount of information that can be reliably transmitted by an information carrier [87]. In an optical system,

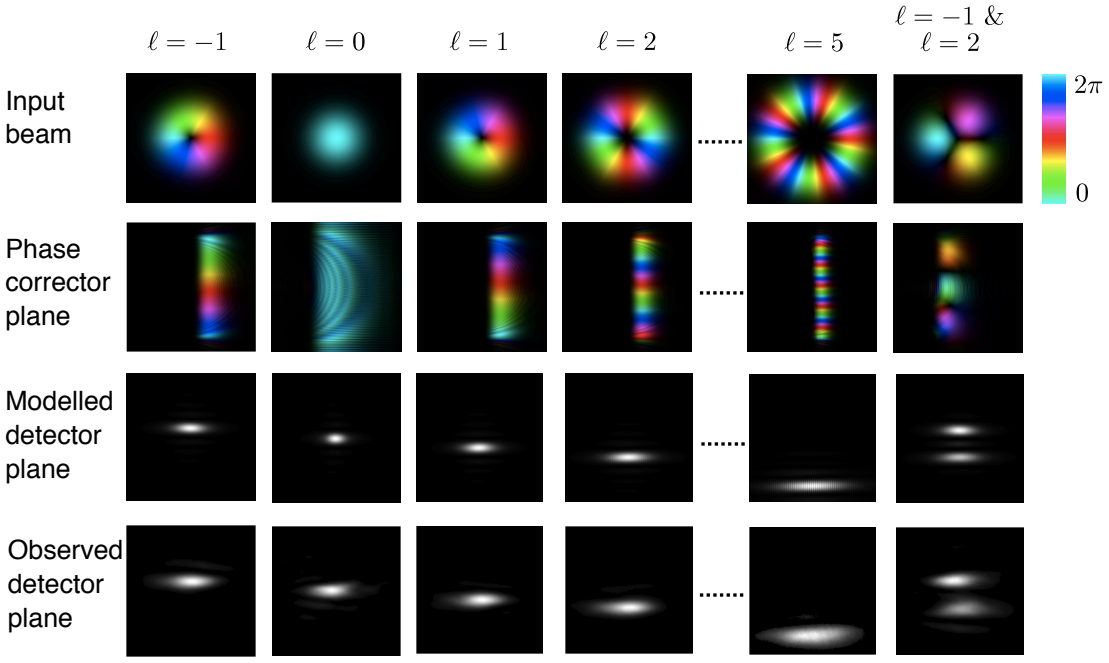


Figure 4.2: Modelled and observed phase and intensity profiles at various planes in the optical system. From left to right, the images show the modelled phase and intensity distribution of the input beam just before the transforming optical element and just after the phase-correcting element, and the modelled and observed images in the CCD plane for five different values of $\ell$. The final row shows the results for an equal superposition of $\ell = -1$ and $\ell = 2$. The last two columns are $6\times$ magnified with respect to the first two columns.

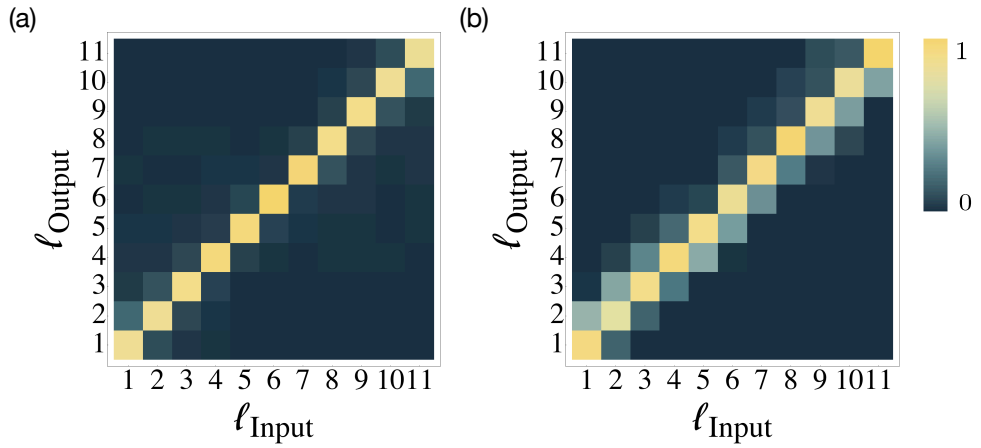


Figure 4.3: Total intensities in all detector regions for pure input OAM states from $\ell = -5$ to $\ell = 5$, for both the (a) modelled and (b) observed results. The regions all have the same size and are chosen such that they fill the entire aperture. The intensities are shown as a fraction of the total intensity in the input beam.

this channel capacity can be quoted as "bits per photon". If a photon can be in one of $N$ input states and its state can be measured perfectly at the output, the channel capacity takes the theoretical maximum value of $\log_2 N$.

Table 4.1 presents the channel capacity of the system for the modelled and observed results, calculated from the data shown in figure 4.3. A generic approach to minimise cross-talk is to increase the separation between channels. I therefore consider the case where only every other state, $\Delta\ell = 2$, and every third state, $\Delta\ell = 3$ are used. This approach gives fewer states within the $\ell$ range considered, but reduces overlap between different spots. In all cases, due to experimental imperfections, the channel capacity for the observed data is slightly lower than the modelled one, but for $\Delta\ell = 3$ it approaches it very closely, confirming again that this system is capable of sorting OAM states with high accuracy.

It should be noted that the optical transformation is only perfect for rays which are normally incident on the transforming element. Helically-phased beams are

| $\Delta\ell$ | **N** | $\log_2$ **N** | **Modelled** | **Observed** |
|---|---|---|---|---|
| 1 | 11 | 3.46 | 2.36 | 1.96 |
| 2 | 6 | 2.59 | 2.10 | 1.93 |
| 3 | 4 | 2.00 | 1.70 | 1.68 |

Table 4.1: Channel capacity calculated from the results shown in figure 4.3. The first three columns show the separation between the channels, $\Delta\ell$, the number of states taken into account, $N$ and the theoretical maximum value, $\log_2 N$. The last two columns correspond to the data shown in figure 4.3 (a) and (b), respectively.

inherently not of this type, the skew angle of the rays being $\ell/kr$ [76]. Although this skew angle is small when compared to the angles introduced by the transforming element, it might introduce a slight transformation error which increases with $\ell$. If the input is a ring-like intensity profile, the skew angle leads to a sinusoidal distortion from the expected rectangular output. This potential skew ray distortion is reduced by decreasing the propagation distance over which the transformation occurs, i.e. reducing $f$.

In its present form, this approach is limited by the fact that the resulting spots are slightly overlapping. This is because our transformation discards the periodic nature of the angular variable, using instead only a single angular cycle and producing an inclined plane wave of finite width, and similarly a finite spot width. One option for improvement is to modify the transformation to give multiple transverse cycles, which results in larger phase gradient and thus a larger separation between the spots, albeit at the expense of increased optical complexity. One approach to implementing this improvement would be to add a binary phase grating to the transforming elements, producing both positive and negative diffraction orders. By adjusting the pitch of the grating appropriately, two identical, adjoining copies of the reformatted image are created in the plane of the phase-corrector.

In this proof of principle mode sorting technique, comprising of two bespoke

optical elements, we have shown its ability to efficiently measure the OAM state of light, and presenting a platform for the development of this technique further. A concern with this implementation is that a 70% light loss associated with the two SLMs that comprise the mode sorter. This loss could, however, be eliminated by replacing the SLMs with equivalent custom-made refractive optical elements.

# 5

# Refractive elements for the measurement of the orbital angular momentum of a single photon

In the previous chapter the development of two diffractive optical elements, implemented on spatial light modulators (SLMs), that can be used to transform OAM states into transverse momentum states was discussed [10]. This was achieved through the use of a mapping from a position $(x, y)$ in the input plane to a position $(u, v)$ in the output plane, where $u = -a\ln(\sqrt{x^2+y^2}/b)$ and $v = a\arctan(y/x)$ [19, 46, 86]. A mapping of this type transforms a set of concentric rings at the

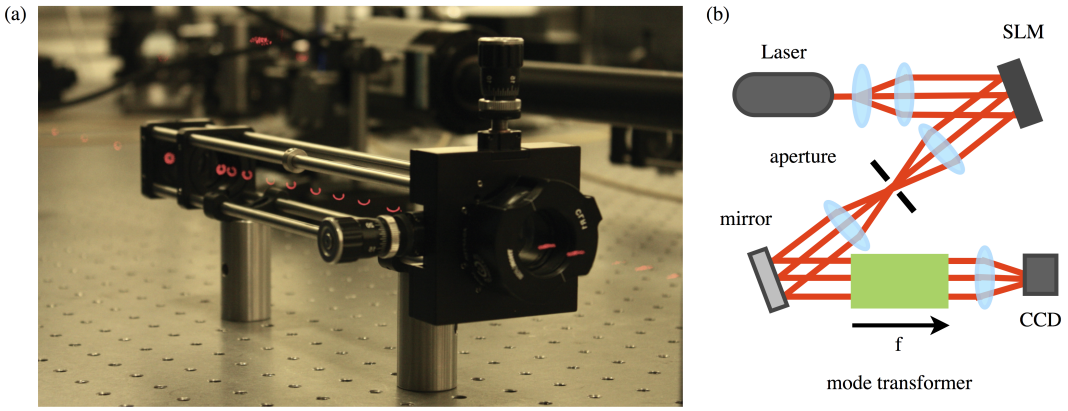


Figure 5.1: (a) Transformation of OAM states into transverse momentum states with refractive optical elements. An image of the beam was captured in several transverse planes and overlaid (in red) to give the image shown above. (b) A beam carrying OAM is prepared through the use of a $\ell$-forked hologram, realised using a spatial light modulator (SLM) and then passed through the two elements, represented as the green rectangle, required to perform the transformation of both the phase and intensity of the beam.

input plane into a set of parallel lines in the output plane. The combination of the two diffractive optical elements transforms both the phase and intensity of the beam in the form $\exp(i\ell\phi)$, to give a complex amplitude at the output plane of the form $\exp(i\ell v/a)$. A lens can then separate the resulting transverse momentum states into specified lateral positions, allowing for the efficient measurement of multiple states simultaneously [11, 51]. In the proof-of-principle demonstration outlined in chapter 4, approximately three quarters of the input light was lost due to the limited diffraction efficiency of the SLMs [10].

To overcome these limitations on efficiency I replaced the previously used diffractive optical elements with refractive elements which carry out the desired optical transformation (figure 5.1). The transmission efficiency of the combination of elements is approximately 85%, which makes them attractive for use with single photons. The number of components was also reduced through the integration

of the transform lens previously required between the diffractive optical elements into the transformation elements themselves. The height profiles for the refractive elements (figure 5.2) were derived from the equations defining their phase profile, $\phi_1$ and $\phi_2$ in equations 4.6 and 4.7 respectively, along with the addition of a lens term, indicated in equations 5.1 and 5.2 shown below.

When light of a particular wavelength, $\lambda$, propagates through a material of thickness $Z$ with a refractive index $n$, the effective optical path length changes with respect to the same distance of propagation in a vacuum. The change in path length can be expressed as a change in phase of $\Delta\Phi = 2\pi(n-1)Z/\lambda$, hence the first element requires a height profile of

$$Z_1(x,y) = \frac{a}{f(n-1)}\left[y\arctan\left(\frac{y}{a}\right) - x\ln\left(\frac{\sqrt{x^2+y^2}}{b}\right) + x - \frac{1}{a}\underbrace{\left(\frac{1}{2}(x^2+y^2)\right)}_{lens\ term}\right], \tag{5.1}$$

where $f$ is the focal length of the integrated lens. There are two free parameters, $a$ and $b$, which determine the scaling and position of the transformed beam. The parameter $a$ takes the value $a = d/2\pi$, ensuring that the azimuthal angle range $(0 \mapsto 2\pi)$ is mapped onto the full width of the second element, $d$. The parameter $b$ is optimised for the particular physical dimensions of the sorter. The second of these elements has a height profile

$$Z_2(x,y) = -\frac{ab}{f(n-1)}\left[\exp\left(-\frac{u}{a}\right)\cos\left(\frac{v}{a}\right) - \frac{1}{ab}\underbrace{\left(\frac{1}{2}(u^2+v^2)\right)}_{lens\ term}\right], \tag{5.2}$$

where $u$ and $v$ are the coordinates in the output plane. This element is placed

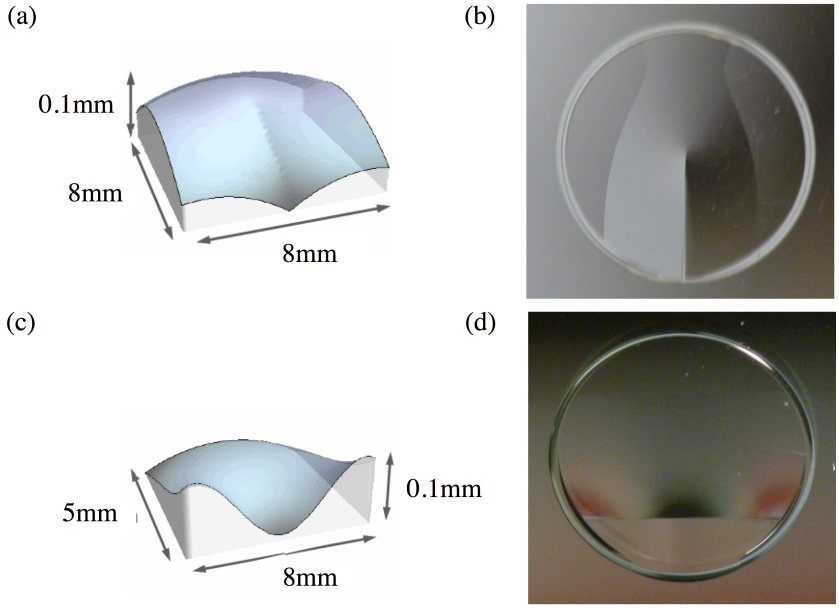


Figure 5.2: Height profiles (a,c) and photos (b,d) of refractive elements 1 (top) and 2 (bottom). The aperture size is $d = 8\,\text{mm}$, focal length $f = 300\,\text{mm}$ and the parameter $b = 0.0447$. The surfaces were made from PMMA (Poly methyl methacrylate), using a machined radius of 5.64 mm, angular spacing 1°, radial spacing of 5 $\mu$m, spindle speed of 500 RPM, roughing feedrate 5 mm/minute with a cut depth of 20 $\mu$m and finishing feedrate 1 mm/minute with a cut depth of 10 $\mu$m [30].

a distance $f$ behind the first element. Each surface is wavelength independent, but dispersion effects in the material manifest themselves as a change in the focal length of the integrated lens for different wavelengths. Hence, the system can be tuned to a specific wavelength by changing the distance between the elements.

The elements were diamond machined by collaborator David Robertson, using a Natotech, 3 axis (X,Z,C) ultra precision lathe (UPL) in combination with a Nanotech NFTS6000 fast tool servo (FTS) system to provide a fast (W) axis superimposed on the machine Z-axis. The machining programme was generated using proprietary code written within commercially available software, DIFFSYS.

This programme converts the input data, in the form of an (X,Y,Z) cloud of points, into the requisite UPL machine and FTS system machining files.

Generally, when machining freeform surfaces it is normal to separate out the symmetrical and non-symmetrical components to realise minimum departure, of the FTS tool and therefore maximise machining performance [30]. However, as the total sag height difference for each part was relatively small (115 $\mu$m for surface 1 and 144 $\mu$m for surface 2) and as both surfaces are highly asymmetric resulting in a small component of symmetric departure the elements were machined using FTS tool movement in W only. The surfaces are shown in figure 5.2 (b) and (d).

In the experiment I generated Laguerre-Gaussian (LG) beams by expanding a HeNe laser onto a $\ell$-forked hologram realised using a SLM by programming it with both phase and intensity information. The beam generated in the first order of the hologram was selected with an aperture and the plane of the SLM is imaged onto the plane of the first element. The beam was then passed through the elements transforming it into the form $\exp(i\ell v/a)$, giving a transverse direction state which is then focussed into an elongated spot on a camera. The transverse position of the spot is dependent on $\ell$.

An important consideration in any communication system is the cross talk between the channels in that system. To assess this the camera was portioned into $N$ adjacent regions, where each region is centred on one elongated spot, and the measured intensity of the pixels in the region was summed for each region. For a single input mode, one would expect the majority of the energy to be detected in the bin corresponding to the input mode and any energy readings in other regions represent cross talk between channels. Our transformation from orbital angular momentum states into transverse momentum states gives rise to inherent

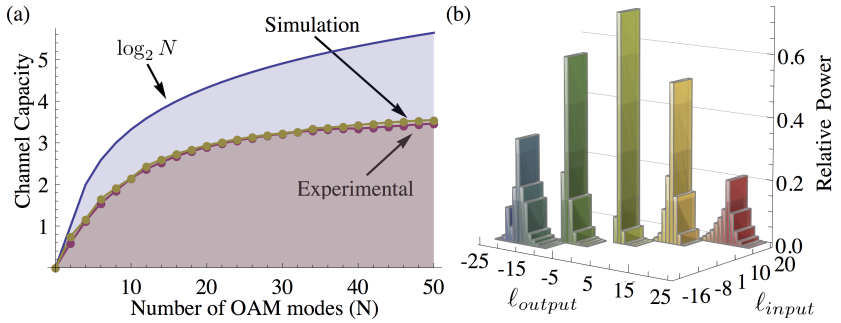


Figure 5.3: (a) Channel capacity for $N$ LG modes, where $N = 2, 4, 6, ..., 50$. Detector noise was measured with no light incident on the camera, which was overcome by setting a threshold with a signal to noise ratio of 3000 to 1. (b) The ratio of energy measured in each of the detector regions showing the degree of cross talk.

cross talk due to the diffraction limit. The inherent degree of cross talk can be deduced from Fourier theory, which predicts approximately 80% of the input light will be present in the bin corresponding to that input OAM mode value. A common method of evaluating the degree of cross talk in a communications system is the channel capacity, which is the maximum amount of information that can be reliably transmitted by an information carrier, as used in chapter 4 [87]. In a multi-channel system, a photon can be in one of $N$ input states and the maximum channel capacity value is $\log_2 N$ bits per photon.

To evaluate the range of modes the system was able to detect efficiently, the system was tested using LG beams over the mode range $\ell = -25$ to $\ell = 25$. The choice of LG beams allows the beam waist to be controlled, and the experimental result to be very closely matched to numerical modelling of the system. The channel capacity was measured for $N$ modes, where $N = 2, 4, 6, ..., 50$. For integer steps over the measurement range $\ell = -N/2$ to $\ell = N/2$ was used, while leaving $\ell = 0$ free as an alignment channel. The values measured are shown in figure 5.3. The optical transformation we utilise is only perfect for rays that are normally

incident on the transformation elements. Helically phased beams are inherently not of this type, and have a skew angle of the rays of $\theta_s = \ell/kr$, where $k$ is the wavenumber of the light and $r$ is the distance from the beam centre [76, 57]. A numerical simulation of the experimental setup was carried out using plane wave decomposition [10]. Comparing channel capacity values from the simulated and experimentally obtained results, with that of the maximum possible channel capacity, one sees the difference increases at higher mode ranges. These results are consistent with the larger skew angle at higher $\ell$ causing errors in the transformation, hence increasing the channel cross talk at these $\ell$ values. Simulations show that reducing the separation between the components or increasing the aperture size of the system can reduce these skew angle effects at higher $\ell$ values, hence reducing the cross talk within the system and is discussed in detail in chapter 6.

The optical efficiency of the transformation elements is very important for the use of such a technique within quantum optics. To test that the transformation elements were adequately efficient for use with single photons, I replaced the standard camera with an electron multiplying CCD (EMCCD) camera that is sensitive to single photons. The power of the input beam before the first element was attenuated to a power of approximately $2 \times 10^{-17}\,W$, corresponding to photon flux of approximately 75 photons per second entering the first element. The camera was set to capture 100 frames per second, hence on average we record less than one photon per measurement.

To verify that the measurements corresponded to the expected number of photons, I first measured the unattenuated power before entering the first element and at the camera plane giving a measured transmission efficiency of approximately 75%, 10% lower then the combination of transformation elements. This

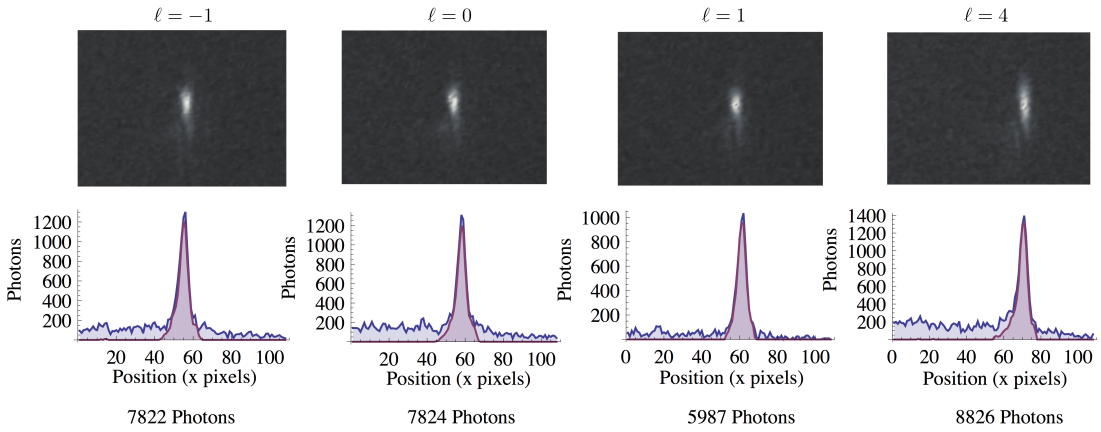


Figure 5.4: Using an EMCCD camera in single photon counting mode, images were generated by summing over 16383 frames. Noise is generated on every pixels in the camera even when no light is incident upon it, known as dark counts. The images shown are the raw captured images. The dark count rate was assessed by counting the photons over the same capture period with the camera shutter closed. A threshold was set with a value corresponding to the mean, plus one standard deviation, of the dark count rate. The corresponding graph is the sum of each column, in blue, and superimposed with the results when a Wiener Noise reduction filter is applied shown in red [100]. Summing under the red curve gives us an approximation of the number of photons received at the camera plane.

difference arises from the losses due to scatter of the other optical components. The efficiency could be further improved by adding anti-reflective coating to the elements. A measurement of the efficiency at the level of single photons was made by counting the number of photons detected over a large number of accumulated camera frames when used in single photon counting mode. The images produced are shown in figure 5.4. The quantum efficiency of the entire system (including the effects of all optical components and the efficiency of the EMCCD camera) was measured to be approximately 50%.

These modifications to the mode-sorter, such that it comprises of two refractive elements which can separate beams carrying OAM into discrete regions on a detector with a transmission efficiency of 85%. In the case of many photons, the experimental system was characterised to have a channel capacity of 1.85 bits per photon for 8 modes, 2.68 bits per photon for 16 modes and 3.26 bits per photon for 32 modes. An attenuated laser source, where on average there was less then one photon in the system within any measurement period, demonstrates the elements are capable of separating the OAM states of the input light at the level of single photons. This modified approach could be used to detect, or if used in reverse generate, OAM states used within quantum communications or quantum key distribution systems, increasing the amount of information one can encode onto a single photon.

# 6

# Increasing the OAM bandwidth of the mode-sorter

As discussed in chapter 4, the mode-sorter transforms azimuthal position in the input beam into a transverse position in the output beam. Key to the reliable position mapping is that the transformed coordinates of the light ray, $u$ and $v$ should depend only on the input coordinates $r$ and $\theta$ that determine the position at the input plane, and not on the ray's direction. Our mode-sorter works by the first element introducing a spatially dependent deviation to the ray direction,

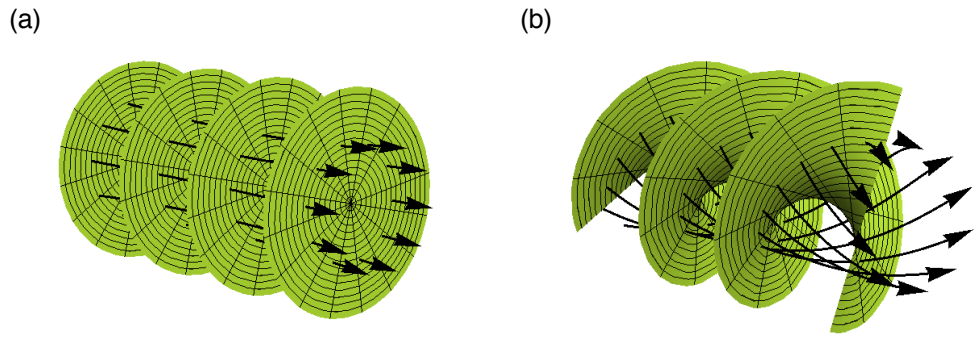


Figure 6.1: The local ray direction, shown as arrows, is perpendicular to the phase fronts, shown as green surfaces. (a) In beams with $\ell = 0$, the local ray direction has no azimuthal component. (b) In beams with $\ell \neq 0$, the local ray direction does have an azimuthal component. The figure is drawn for $\ell = 2$.

such that upon propagation to the second element the ray arrives at the required position with Cartesian coordinates $u$ and $v$. The role of the second element is to ensure that relative phase is preserved. The elements are designed to work perfectly for collimated beams, in which all light rays arrive at normal incidence at the first component. For non-collimated beams we require that the angular deviation introduced by the transformation dominates over any deviation from normal incidence with rays that arrive at the first element.

If the input beam is an annulus of radius $r$ and the separation between the two elements is $L$, then the angular deviation introduced by the sorter is of order $\tan^{-1}(r/L)$, which is approximately $r/L$ for small angles. Deviations from normal incidence of the rays direction in the incident beam can be due to beam divergence, alignment or other properties. Irrespective of their divergence, beams carrying OAM are never plane waves as they have an azimuthal component to the Poynting vector, discussed in chapter 1, giving such beams their angular momentum in

the direction of propagation (figure 6.1). For a beam described by an azimuthal phase term $\exp(i\ell\theta)$, the local skew angle of the Poynting vector in the azimuthal direction is given by $\tan^{-1}(\ell/kr)$ [76]. Close to the beam axis, i.e. for $r \approx 0$, this skew angle reaches 90°, and so the deviation introduced by the sorter cannot dominate, but conveniently OAM states with $\ell \neq 0$ are dark along their beam axis. It follows that for the sorter to work well for beams of radius $r$ one requires $\ell/kr \ll r/L$, which gives (with $k = 2\pi/\lambda$)

$$\ell \ll \frac{2\pi r^2}{L\lambda}. \tag{6.1}$$

It should be noted that the RHS of this equation reaches its maximum value when the radius of the input beam matches the radius of the optical element. The RHS is essentially the Fresnel number of the optical elements.

To maximise Fresnel number and therefore OAM bandwidth, the free-form optical elements are designed such that they have the largest aperture that can be achieved by our method of manufacture ($R = 12\,\text{mm}$) and the shortest possible separation between the optical elements ($L = 300\,\text{mm}$), which is limited by the maximum surface gradient that can be machined. The resulting Fresnel number is $F = R^2/L\lambda \approx 760$. However, for measuring laser beams of finite size it can be noted that the effective Fresnel number of the system is set by the radius of the optics, or the radius of the beam itself, whichever is the smaller. The elements were diamond machined using a Nanotech three-axis ultra-precision lathe in combination with a Nanotech NFTS6000 fast tool servo system to provide a fast axis superimposed on one of the axes of the lathe. The increase in the aperture size results in deeper cuts as overall thickness variation of the surface has increased. A

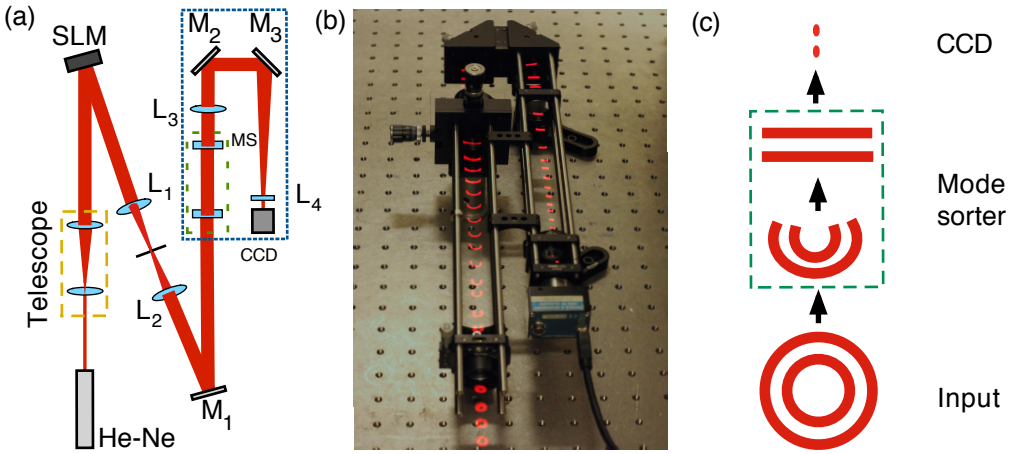


Figure 6.2: (a) A beam carrying OAM is prepared through the use of a $\ell$-forked hologram, realised using a spatial light modulator (SLM), and a Fourier filter (lenses $L_1$ and $L_2$ and the aperture between them) that selects the desired first diffraction order. The beam is then passed through the optical transformer, i.e. the two custom refractive components in the green dashed box. The spherical lens $L_3$ and the cylindrical lens $L_4$ complete the transformation of the beam. Together, the components in the blue dashed box form the mode sorter (MS). (b) Photo of the mode sorter realised in the lab. An image of the beam was captured in several transverse planes and overlaid (in red), showing the shape of the beam in those planes. (c) Schematic of the beam transformation performed by the mode sorter.

vacuum chuck is generally used in such a lathe; however, due to the large cut depth a semi-permanent bonding technique was used. A water-soluble wax, produced by Nexgen Optical, was used as the bonding agent as this can easily be de-bonded with the use of a standard ultrasonic system. The output plane of the mode sorter was focussed to the plane of the detector using a spherical lens ($L_3$ in figure 6.2; focal length $f_3 = 500\,\text{mm}$) in combination with a cylindrical lens ($L_4$; focal length $f_4 = 40\,\text{mm}$), giving a lateral displacement of $17.6\,\mu\text{m}$ for an increase $\Delta\ell = 1$ in OAM value and a radial magnification of 0.096.

I generated the input OAM test modes by the use of a simple forked diffraction grating created using a spatial light modulator (SLM) that is illuminated by the expanded Gaussian beam produced by a HeNe laser [6, 44]. This results in a helically phased beam with a Gaussian intensity distribution. To obtain radial control of the intensity distribution I apply a spatially dependent reduction of the contrast of the hologram, allowing the creation of a mode in the first-order diffracted beam that is a close approximation to the chosen Laguerre-Gaussian mode [55]. This approach allows control over the beam waist $w_0$ independent of the mode index $\ell$. The SLM is then imaged to the input pupil of the OAM mode sorter. Varying $w_0$ therefore allows measurement of the OAM bandwidth for different effective Fresnel numbers.

I generated a set of sequential input modes over the range $\ell = -28$ to $\ell = +28$ with a specific $w_0$. Three different values of $w_0$ were tested for the same set of $\ell$-values, corresponding to three different effective Fresnel numbers. A CCD array was placed at the focal plane of the final lens where adjacent, equally-sized, regions were defined, each corresponding to a specific $\ell$-value. The total intensity over all the pixels in each region was summed to give the relative power in each of the

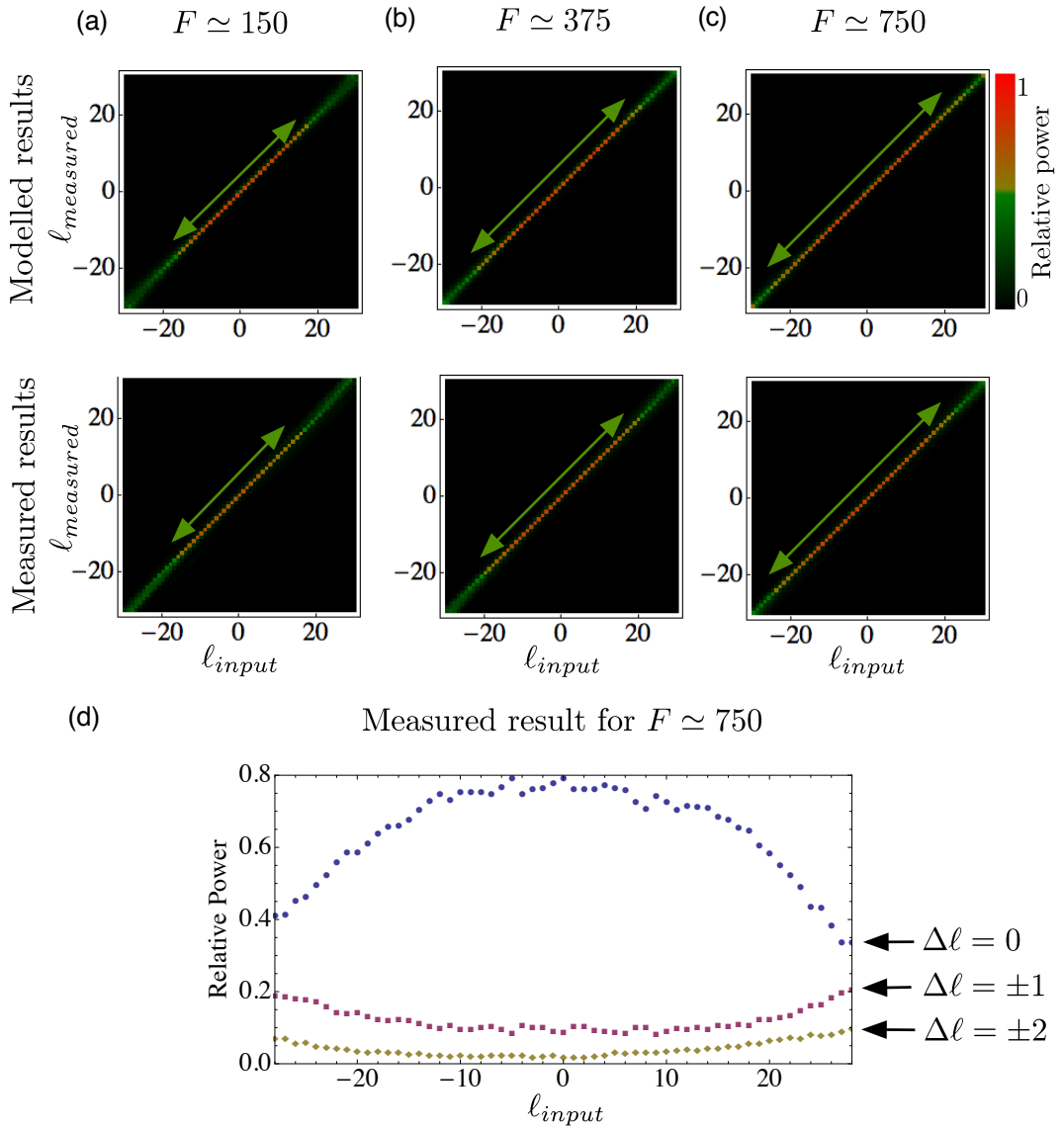


Figure 6.3: (a-c) Colour representation of the power in the bins corresponding to OAM states with $\ell = \ell_{\text{measured}}$ for incident pure OAM modes with $\ell = \ell_{\text{input}}$. The columns (a), (b) and (c) correspond to different effective Fresnel numbers of the system, which were achieved by changing the waist size $w_0$ of the input mode. In each column, modelled (top) and measured (bottom) results are shown. The green arrows indicate the measurement bandwidth where the measured relative power is greater then 0.5. (d) Fraction of power in the bins corresponding to $\Delta\ell = \ell_{\text{input}} - \ell_{\text{measured}}$. The top set of points (in blue) represents power that has been correctly identified; where $\ell_{\text{input}} = \ell_{\text{measured}}$ giving $\Delta\ell = 0$. The two lower sets of points are the sum of the power in the bins $\Delta\ell = \pm 1$ (in pink), where $\ell_{\text{measured}} = \ell_{\text{input}} + 1$ and $\ell_{\text{measured}} = \ell_{\text{input}} - 1$ , and $\Delta\ell = \pm 2$ (in brown) which both represent crosstalk.

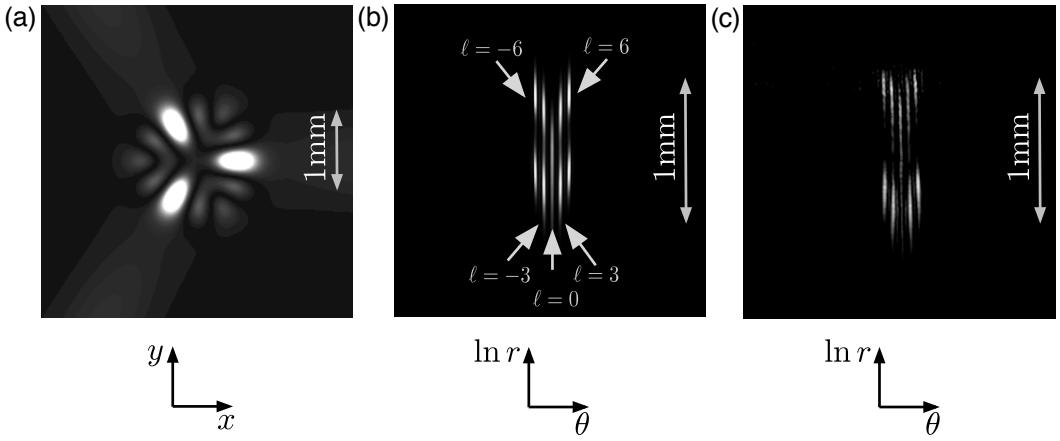


Figure 6.4: Simulated and measured radius-OAM spectrum of a light beam. (a) Simulated intensity cross-section of the incident light beam for a superposition of Laguerre-Gauss modes with $\ell = -6, -3, 0, 3, 6$ and waist size $w_0 = 2\,\text{mm}$ and with $\ell = -6, -3, 3, 6$ and waist size $w_0 = 0.4\,\text{mm}$. The contrast has been altered to increase the visibility of the darker parts of the beam. (b, c) Simulated (b) and measured (c) radius-OAM spectrum of the beam.

OAM modes. As discussed in chapter 4, this approach has some residual cross talk that can be deduced by considering the focal spot produced from a top-hat aperture [10, 53]. In this case, the transformation of a set of concentric rings of light at the input to parallel lines, with finite extent, at the output results in a Sinc distribution when such an output is focused. The secondary maxima of the Sinc distribution result in crosstalk into adjacent OAM channels. This predicts that, for low $\ell$ values, approximately 80% of the input light will be present in the correct bin [53]. Our results (figure 6.3 (a)) show an increase in crosstalk for higher $\ell$ values in the form of a blurring of the diagonal which is consistent with the higher skew angles present in such beams. When the effective Fresnel number is increased, this crosstalk at higher $\ell$ values is reduced (figure 6.3 (b,c)). All our experimental results are in close agreement with a simulation based upon plane-wave decomposition.

In addition to increasing the OAM measurement bandwidth, a further modification was presented, which allows measurement of the full radius-OAM spectrum, i.e. the OAM spectrum present at different radii $r$ in the incident beam, simultaneously for all values of $r$. The mode sorter maps any centred, thin, ring of light of radius, $r$, to a thin line with a corresponding $x$ coordinate. A subsequent spherical Fourier lens performs this Fourier transform and therefore allows measurement of the OAM spectrum, but loses all information about $r$. My solution was to combine the spherical Fourier lens with a cylindrical lens. This combination can be thought of as two orthogonal cylindrical lenses of different focal lengths, one performing an optical Fourier transform of the $y$ coordinate, the other imaging the $x$ coordinate. To show that our setup can measure OAM and $r$ simultaneously, I generated a superposition of 9 different modes. Both numerically modelled and experimentally measured radius-OAM outputs as measured by the CCD array are shown in figure 6.4. It should be noted that sorting of different beam waist can increase the available channels, but as the effective Fresnel number of the system is different for each value of $w_0$, smaller beams have a more restricted $\ell$ bandwidth.

In conclusion, I have presented a solution to increasing the available OAM bandwidth of a mode sorter based on optical transformation, and demonstrated that this works by measuring OAM spectra of over 50 $\ell$ values. With a minor modification this mode sorting technique can be modified such that the OAM spectrum can be measured as a function of $r$. I believe these improvements will increase the feasibility of this OAM measurement technique being implemented as a tool in the fields of optical communication and quantum optics.

# 7

# Measurement of light's OAM spectrum arising from misalignment

Pure OAM states are defined with respect to a specific axis, called the beam axis. This axis is the $z$ axis of the cylindrical polar-coordinate system in which the complex amplitude cross-section in a transverse plane ($z$ = const.) of a pure mode with a specific $\ell$ value can be written in the form $\exp(i\ell\theta)$. When described with respect to a measurement axis different than the beam axis, a pure OAM state becomes a well-defined superposition of a number of these states [98]. In

this experiment, the measurement axis is defined by the OAM mode-sorter. By creating pure OAM states and directing them at the analyser with different offsets and directions, we therefore create well-defined superpositions.

The pure OAM states used within this experiment were the Laguerre-Gaussian (LG) laser modes already mentioned in chapter 1. A LG mode is described by two indices, $\ell$ and $p$. In the waist plane of a LG mode the complex amplitude is given by

$$\begin{aligned}\Psi_{\ell,p}(x,y) = \quad & C_{\ell p}\left(\frac{2\left(x^2+y^2\right)}{{w_0}^2}\right)^{\frac{|\ell|}{2}} L_p^{|\ell|}\left(\frac{2\left(x^2+y^2\right)}{{w_0}^2}\right) \\ & \times \exp\left[\frac{-\left(x^2+y^2\right)}{{w_0}^2}\right] \exp\left[i\ell \mathrm{atan2}\left(y,x\right)\right], \end{aligned} \tag{7.1}$$

where $w_0$ is the waist size, $L_p^{|\ell|}(x)$ is the Laguerre polynomial for the mode indices $\ell$ and $p$, and $C_{\ell p}$ is the amplitude normalisation term [8, 2] given by

$$C_{\ell p} = \begin{cases} \frac{1}{w_0}\sqrt{2p!/[\pi(p+\ell)!]} & \text{for } \ell \geq 0, \\ \frac{1}{w_0}\sqrt{2p!/[\pi(p-\ell)!]} & \text{for } \ell \leq 0. \end{cases} \tag{7.2}$$

Note that the beam is described in Cartesian coordinates here, as this is convenient for the misalignments that were considered. The term $\exp(i\ell\theta)$ then takes the form $\exp[i\ell \mathrm{atan2}(y,x)]$ ($\mathrm{atan2}(y,x)$ is used in place of $\arctan(y/x)$, as arctan does not distinguish between angles that differ by $\pi$). As the LG modes form an orthonormal basis, any beam cross-section $\psi(x,y)$ can be written, using bra-ket notation ($\Psi_{\ell,p}(x,y) = |\ell p\rangle$, $|\psi\rangle = \psi(x,y)$), in the form

$$|\psi\rangle = \sum_{\ell=-\infty}^{\infty}\sum_{p=0}^{\infty}\langle \ell p|\psi\rangle|\ell p\rangle. \tag{7.3}$$

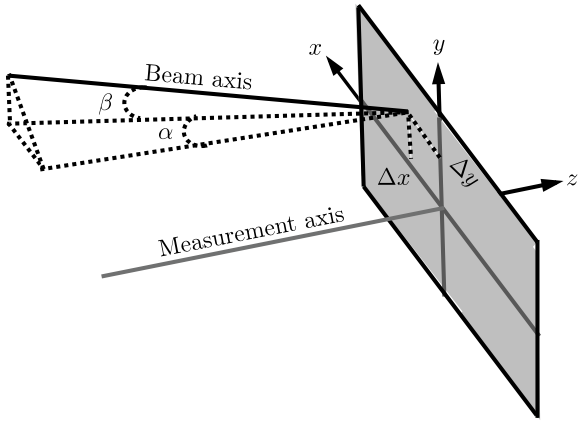


Figure 7.1: Relationship between beam axis and measurement axis. The beam axis is tilted with respect to the measurement axis by the angles $\alpha$ and $\beta$ in the $(x, z)$ and $(y, z)$ planes, respectively. In the plane $z = 0$, the beam axis is offset with respect to the measurement axis in the $x$ direction by $\Delta x$ and in the $y$ direction by $\Delta y$.

The power in the component $|\ell p\rangle$ is then given by the modulus squared of the coefficient for that component, namely

$$P_{\ell,p} = |\langle \ell p|\psi\rangle|^2. \tag{7.4}$$

The power in all components with the same value of $\ell$ is given by

$$P_\ell = \sum_{p=0}^{\infty} P_{\ell,p} = \sum_{p=0}^{\infty} |\langle \ell p|\psi\rangle|^2. \tag{7.5}$$

The set of these powers $P_\ell$ is the OAM spectrum one expects to measure.

These "misaligned" pure OAM states are also LG modes. The misalignment of the beam axis are with respect to the measurement axis described by the parameters $\Delta x$, $\Delta y$, $\alpha$ and $\beta$ as defined in figure 7.1. The complex amplitude of such a

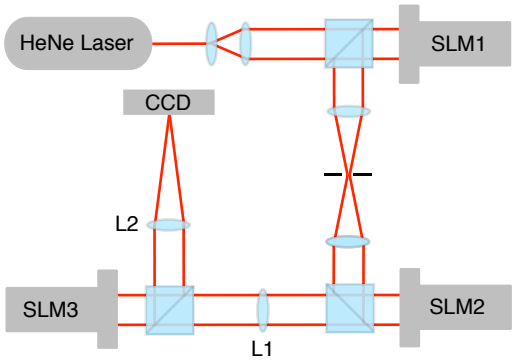


Figure 7.2: Schematic overview of the setup. SLMs are used to both generate Laguerre-Gaussian modes (SLM1) and create the desired phase profiles for the transforming and phase-correcting optical elements (SLM2 and SLM3, respectively). L1 is the Fourier-transforming lens and L2 focusses the transformed beams.

misaligned LG beam is

$$\psi(x,y) = \Psi_{\ell,p}(x-\Delta x, y-\Delta y)\exp\left[i\frac{2\pi}{\lambda}(x\sin\alpha + y\sin\beta)\right], \tag{7.6}$$

where $\Psi_{\ell,p}$ is the complex amplitude of an LG mode whose beam axis coincides with the measurement axis (equation 7.1), and $k = 2\pi/\lambda$, where $\lambda$ is the wavelength of the light. The corresponding OAM spectrum can then be calculated using equation (7.5).

I experimentally analysed the OAM spectrum through the use of the diffractive optical element based mode-sorter outlined in chapter 4. Such a mode-sorting technique relies on two diffractive optical elements with the phase profiles $\phi_1$ and $\phi_2$, where are generated from equations 4.6 and 4.7 respectively. Both of these phase profiles were displayed as holograms on separate spatial light modulators (SLMs), figure 7.2.

To assess the performance of the sorter, I generated an LG input beam using

an additional SLM (SLM1 in figure 4.1). Using relay optics, the first order beam is selected and directed onto the transforming hologram, i.e. the first element of the sorter. This configuration allows me to create a LG mode with a range of $\ell$ values with a variety of lateral or angular offsets. The required transformation was obtained at the back focal plane of the Fourier-transforming lens, L1. SLM3 is placed in this transformed plane, and is programmed with the phase-correcting hologram [48]. This resulted in a beam with a linear phase gradient, or combination of gradients, corresponding to the input superposition of OAM. This was then passed through a final lens which focusses the beam to an elongated spot in its focal plane. The key feature of this focussing is that the transverse position of this spot is dependent on the OAM state of the input beam. To allow for the accurate measurement of the superpositions, the detector is split into regions which are centred on each elongated spot with a size corresponding to the minimum separation between any two adjacent spots. This results in a small "dead space" between some regions, but over the entire detection area this accounts for a loss in detection efficiency of approximately 5%. In the setup 11 of these regions were defined, allowing any superposition of states containing the 11 pure OAM states with $\ell$ values between $-5$ and $+5$ to be analysed.

The OAM spectrum was analysed for several different combinations of lateral shift, $\Delta x$, of the beam position and tilt angle in $\Delta\alpha$, with respect to the axis of the analyser. The measurements made corresponded to the results predicted in [98]. First the spectrum from a pure mode was considered, then the case of a lateral beam displacement of $\Delta x = 0.5w_0$, where $w_0$ is the waist size of the LG beam, and then a tilt of $\Delta\alpha = 0.5\lambda/w_0$. These results are shown in figures 7.3 (a), (b) and (c). In addition to these experimentally recorded observations, we calculate

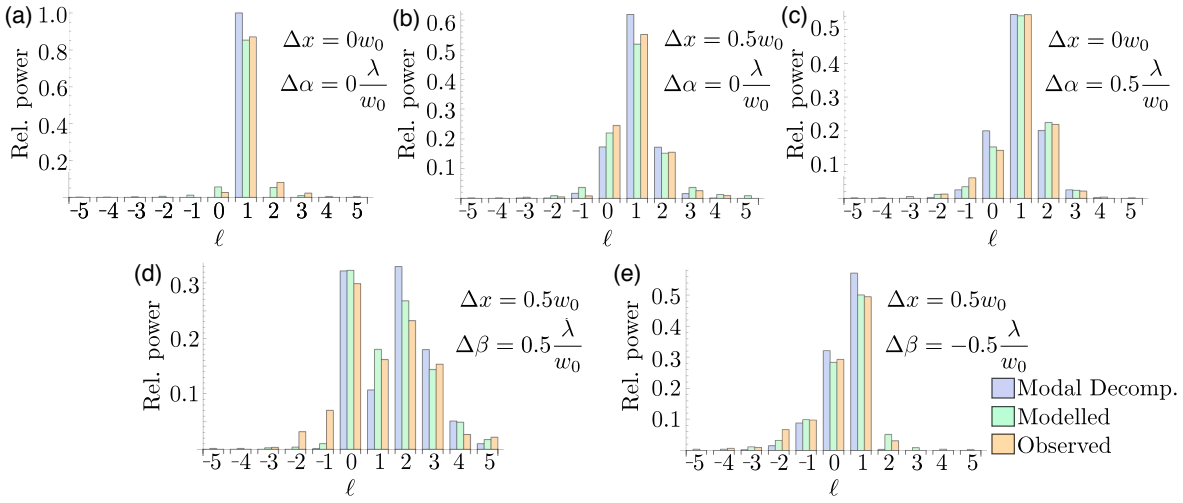


Figure 7.3: The spectrum over 11 states from $\ell = -5$ to $\ell = 5$ where several misalignment cases are considered. (a) Aligned measurement axis and beam axis; $(b)$ is a lateral movement of $x_0 = 0.5w_0$, $(c)$ is a tilt angle in $\alpha = 0.5w_0/\lambda$, $(d)$ is a combination of a lateral movement of $x_0 = 0.5w_0$ and a tilt in $\beta = 0.5w_0/\lambda$, and $(e)$ a tilt in $\beta = -0.5w_0/\lambda$. In each plot we compare the results for the modal decomposition yielding the expected modal content of the beam, a numerical modelling of the experimental setup (Modelled) and the experimentally obtained results (Observed).

the expected spectrum derived from the modal decomposition and a plane-wave decomposition modelling of the experimental configuration of the sorter. For each of these three cases, the resulting spectrum is centred around the original input value. In (d), the lateral displacement of $\Delta x = 0.5w_0$ is combined with a tilt of $\Delta\beta = 0.5\lambda/w_0$, giving an $\ell$-shift in the spectrum. Finally, in (e), a combination of lateral displacement of $\Delta x = 0.5w_0$ is combined with a tilt of $\Delta\beta = -0.5\lambda/w_0$, giving a $\ell$-shift in the spectrum in the the opposite direction as in (d).

Although the agreement between the modal decomposition, the modelling of the sorter and the experimental results are good, it is not perfect. The modal decomposition yields a precise spectrum against which the results should be judged. The difference shown by the modelled results stems from the fact that our sorter suffers from an inherent imperfection arising from the transformation from circular beams into rectangular beams with of a fixed width and height associated with them, discussed in chapter 4. This fixed aperture size results in an overlap between spots and therefore causes an inherent cross talk between states, which is seen as side-bands in 7.3 (a). Finally the observed results are further degraded due to the additional aberrations arising from the SLMs and the other optical components used within the sorter.

These results correspond well to the spectra obtained from modal decomposition of the beam, thereby confirming that our approach yields a useful measurement of the OAM spectrum. The cross talk arising from misalignment with respect to beam axis present an issue for using OAM as an encoding alphabet for communications, as this would increase errors at the receiver. This is a key issue, as even small amounts of misalignment results in a broadened OAM spectrum. However, the well-defined nature of the variance in OAM spectrum with respect

to the input misalignment suggests one could build a feedback system to maintain alignment with the transmitted beam.

# 8

# Influence of atmospheric turbulence on states of light carrying orbital angular momentum.

A fundamental concern for any free-space communications channel is the effect that atmospheric turbulence has on the cross-talk between channels. Atmospheric turbulence has been studied at great length by the astronomy community in relation to aberrations introduced to an image [7]. The natural, randomly time dependent variations in temperature and pressure of the atmosphere result in a

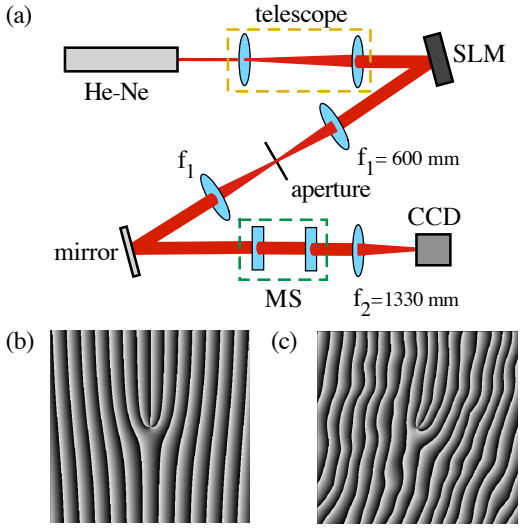


Figure 8.1: (a) A beam carrying OAM is prepared through the use of a $\ell$-forked hologram, seen in (b), realised using a spatial light modulator (SLM), illuminated by an expanded He-Ne laser. The first order beam is imaged onto the front aperture of an OAM mode sorter (MS) which converts OAM states into transverse momentum states with the use of two refractive optical elements. These transverse momentum states are then focused to specific spatial locations on a CCD. The power measured in each of these locations gives a measure of the OAM superposition incident on the mode sorter. (c) Thin phase turbulence is added to the $\ell$-forked hologram changing the OAM superposition measured by the system.

change in density of the atmosphere. Such a change in density results in a spatial dependent change of the refractive index leading to a phase distortion across a transmitted beam [94]. A phase distortion of this type can be considered as a phase screen, and is commonly referred to as thin phase turbulence [36].

In this chapter, the effects of atmospheric turbulence on a communications system utilising OAM modes as the information carrier are experimentally studied. I generate a single OAM mode using a spatial light modulator (SLM). Atmospheric turbulence is then simulated by the addition of a turbulent phase screen to the phase hologram displayed on the SLM, figure 8.1. Once the turbulence is applied, the phase aberrations results in a spread of the input mode power over neigh-

bouring OAM modes, resulting in cross talk between the channels. This spread in power was then measured for different turbulence strengths.

Phase screens corresponding to a particular turbulence strength were generated by collaborator Malcolm O'Sullivan through the use of Kolmogorov turbulence theory [36]. The aberrations introduced by atmospheric turbulence can be considered as normal random variables, where the ensemble average can be written as $\left\langle [\phi(\mathbf{r_1}) - \phi(\mathbf{r_2})]^2 \right\rangle$ and is known as the phase structure function [97]. $\phi(\mathbf{r_1})$ and $\phi(\mathbf{r_2})$ are two randomly generated phase fluctuations. From Kolmogorov statistics it can be shown that this ensemble average must meet the requirement that

$$\left\langle [\phi(\mathbf{r_1}) - \phi(\mathbf{r_2})]^2 \right\rangle = 6.88 \left| \frac{\mathbf{r}_1 - \mathbf{r}_2}{r_0} \right|^{5/3}. \tag{8.1}$$

The value $r_0$ is the Fried parameter, and is a measure of the traverse distance scale over which the refractive index is correlated [36]. To characterise the effect of turbulence on an optical system, a ratio $D/r_0$ is considered, where $D$ is that aperture of the system. This ratio sets two limiting cases, first when $D/r_0 < 1$ the resolution of the system is limited by its aperture, and second when $D/r_0 > 1$ the atmosphere limits the systems ability to resolve an object [36].

In 2005, Patterson predicted the spread in the OAM spectrum resulting from thin phase turbulence [80]. Considering a single OAM mode, $\psi_\ell$, transmitted through an ensemble average of many turbulent phase screens, the power, $s_\Delta$, in the particular mode, $\psi_{\ell+\Delta}$, is given by

$$s_\Delta = \frac{1}{\pi} \int_0^1 \rho \, \mathrm{d}\rho \int_0^{2\pi} \mathrm{d}\theta \, e^{-3.44\left[\left(\frac{D}{r_0}\right)\left(\rho \sin\frac{\theta}{2}\right)\right]^{5/3}} \cos \Delta\theta, \tag{8.2}$$

where $\Delta$ is an integer step in mode index of $\ell = 1$, and $\rho = 2r/D$ [97].

Within these experiments OAM modes were generated by use of a simple forked diffraction grating created using an SLM that is illuminated by the expanded Gaussian beam produced by a He-Ne laser. Rather than producing a pure Laguerre-Gaussian mode, this results in a helically phased beam that in the image plane of the SLM has a near Gaussian intensity distribution. This approach maintains the ratio $D/r_0$ independent of the mode index. A particular turbulent phase screen can then be added to this hologram to simulate the presence of atmospheric turbulence. The SLM is then imaged to the 8 mm diameter input pupil of the OAM mode sorter to decompose the resulting beam into its constituent OAM modes.

As previously discussed in chapter 5, the mode-sorter uses two refractive optical elements which transform OAM states into transverse momentum state. A lens then can focus these transverse momentum states into specific lateral positions. A CCD array was placed at the focal plane of this lens. Eleven adjacent, equally sized regions were selected, each region corresponding to a specific $\ell$-value. The total counts over all the pixels in each region was summed to give the relative power in each of the OAM modes. The power was measured across all the eleven regions and normalised with respect to the power measured for $l = 0$ with no turbulence applied. These powers were plotted as a function of the turbulence strength $D/r_0$.

A mode range of $\ell = -5$ to $\ell = +5$ was investigated, and for 100 randomly generated phase screens the average power in each OAM mode was measured, see figure 8.2. A range of turbulence levels characterised by $D/r_0$ were tested. As predicted by equation 8.2 the crosstalk between OAM modes increases with turbulence and in this mid/high turbulence regime it was found that the agreement between theory and the measurements were good. In the low turbulence regime

the cross-talk between modes arises from residual crosstalk in the mode sorter which arrises due to the diffraction limit as discussed in chapter (5) [10, 53]. The weightings of the power in the known input states described by an $N = 11$ element column vector $[I]$ are mapped by an $N \times N$ cross talk matrix onto the measured $N$ element output vector $[O]$ equation 8.3. For the case of zero residual crosstalk, this matrix would have a leading diagonal of 1s and 0s elsewhere. For finite crosstalk the coefficients $a - j$ etc., are measured at zero turbulence and then this matrix is used to predict the measured OAM output spectrum for an input OAM state subject to the atmospheric cross-talk from the Paterson model (equation 8.2).

$$\begin{bmatrix} O_0 \\ O_1 \\ \vdots \\ O_N \end{bmatrix} = \begin{bmatrix} 1-g & a & \dots & b \\ c & 1-h & \dots & d \\ \dots & \dots & \dots & \dots \\ e & f & \dots & 1-f \end{bmatrix} \begin{bmatrix} I_0 \\ I_1 \\ \vdots \\ I_N \end{bmatrix} \tag{8.3}$$

It is seen in figure 8.2, that at high turbulence values, where $D/r_0 \gg 1$, the average power is equally spread between all the possible detections modes. It should be noted that we are only considering the proportion of the power detected within each of the eleven summed regions on our CCD and not considering the power incident outside these regions.

Patterson's earlier work indicates that the probability of modal cross talk resulting from atmospheric turbulence is independent of the mode propagating through that turbulence. For each of the modes in our chosen region, the same set of turbulent phase screens were applied, and cross-talk measured (figure 8.3). It should be noted that the observed cross-talk is indeed similar for the range of

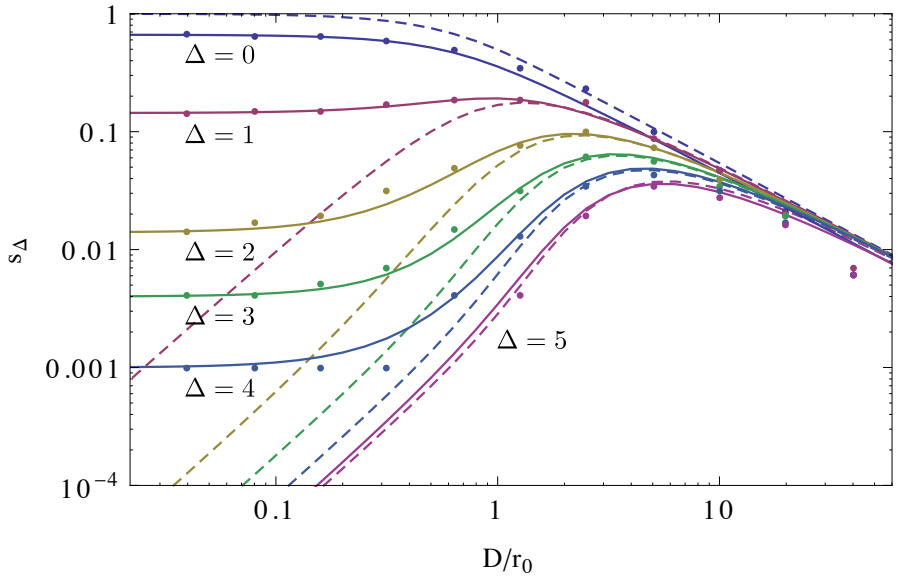


Figure 8.2: The average power ($s_\Delta$) in detected mode $\Psi_\Delta$ is plotted as a function of turbulence strength ($D/r_0$) for an input mode with $\ell = 0$ [see equation 8.2]. Experimental data (dots) is coplotted with the theoretical prediction given by equation 8.2 taking into account the inherent crosstalk of the mode sorter (solid lines). The original theory from [80] is also plotted for comparison (dotted lines).

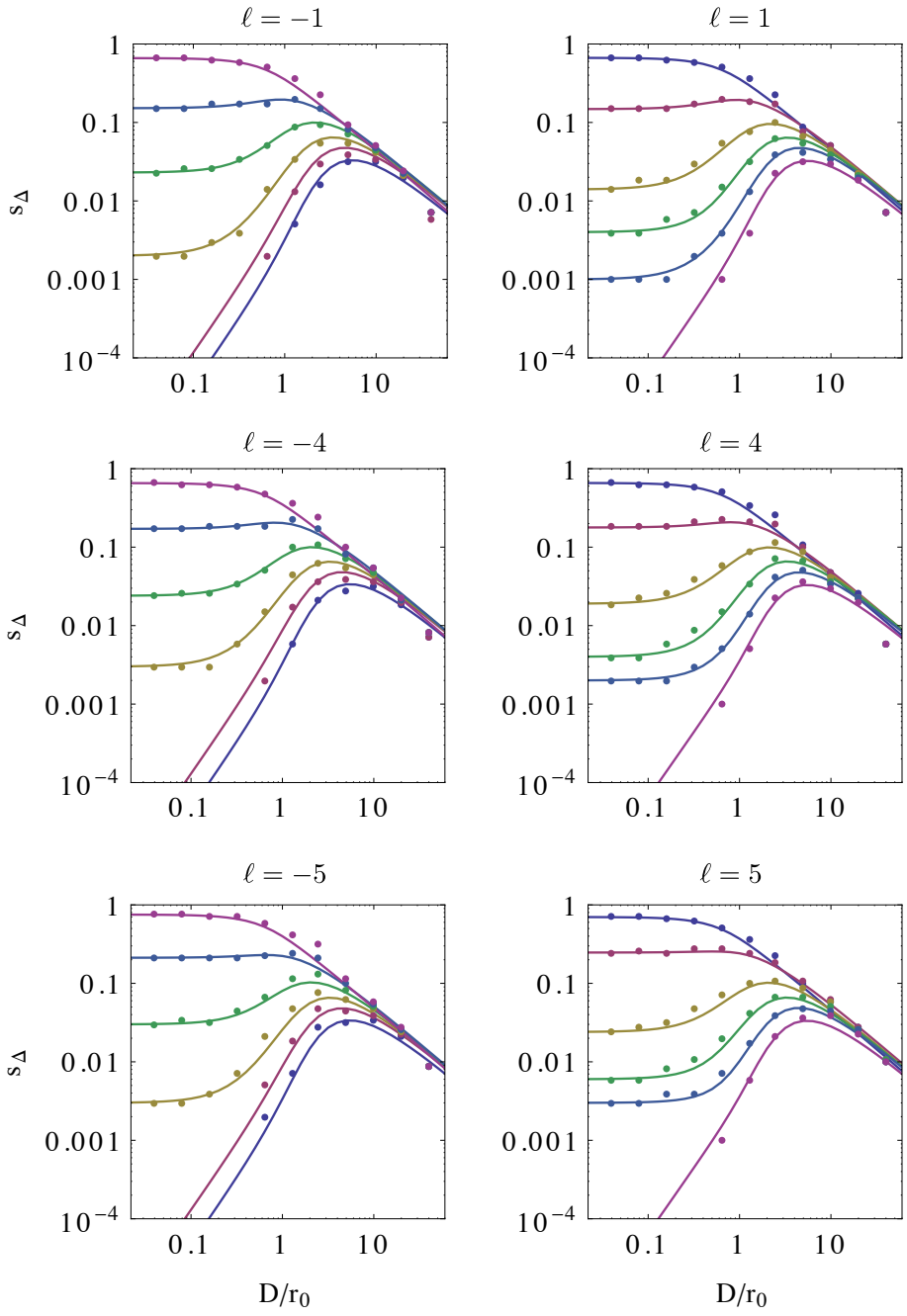


Figure 8.3: The spread in power resulting from atmospheric turbulence was measured for a range of different propagating OAM modes $\psi_\ell$.

OAM modes that were examined.

This experiment only considered the case were turbulence can be represented as a thin phase screen. Such an approach is widely used in astronomy, as when one considers the distance to an astronomical light source, the largest proportion of the turbulence is experienced, relatively, very close to the observer. In the case of long distance point to point communications on earth, turbulence is characterised more accurately by multi-plane turbulence, however, I expect similar principles to apply in the two cases.

Knowledge of the limits atmospheric turbulence impose on a free-space communications channel are very important for designing an optical system operating in such an environment. By experimentally characterising the effects of thin phase turbulence over a range of $\ell = -5$ to $\ell = +5$ it was shown that turbulence similarly degrades the quality of all the modes within this range. This result indicates that a system implementing adaptive optics to reduce the effects on turbulence, can operate independently of the communications channel. This independence arrises from the turbulence being reduced to a single phase error across the beam, as such, determining the phase error for a probe gaussian beam would allow a correction pattern to be generated that could be applied all higher order OAM modes. This probe beam could potentially be at a different wavelength or polarisation from those being used for encoding information, and the required turbulence corrections patterns could be determined simultaneously. The experimental data presented also indicates a potential working range of free space OAM channel and the expected crosstalk for that system.

# 9

# Detection of a spinning object using light's orbital angular momentum

In recent years, consideration has been given to the use of orbital angular momentum in imaging and remote sensing, where the detection of the angular momentum may reveal the structure or potentially the motion of the object [42, 95, 38, 93, 92]. This chapter presents an experiment showing that when light is scattered from a spinning object, the rotation rate of the object can be measured by analysing

frequency shifts in the orbital angular momentum of the light.

The linear Doppler shift is proportional to the relative velocity between the source and observer. There is also a rotational Doppler shift observable along the rotation axis for which the linear shift is zero. This rotational shift is proportional both to the rotation speed of the object and the light's angular momentum; by analysing the orbital angular momentum of light scattered from a spinning object we can observe a frequency shift many times greater than the rotation rate. Uniquely, this method can remotely detect the rotation of a body with an angular momentum vector parallel to the observation direction.

The Doppler shift is a well-known phenomenon, where the relative velocity $v$ between light source and observer gives a frequency shift $\Delta f$. The resulting frequency shift is $\Delta f_0 = v/c$, where is the unshifted frequency and $c$ is the speed of light. Less well-known than this linear effect is the rotational, or angular, Doppler effect [39, 15]. For a beam with helical phase-fronts, a rotation of angular frequency $\Omega$ between the source and observer shifts the frequency by

$$\Delta f = (\ell + \sigma)\frac{\Omega}{2\pi}, \tag{9.1}$$

where $\sigma = \pm 1$ for right- and left-handed circularly polarised light and $\sigma = 0$ for linearly polarised light, and hence $(\ell + \sigma)\hbar$ is the total angular momentum per photon [25]. All of this previous rotational work has been based on pure OAM states, explicitly rotated using specialist optical elements.

The standard linear Doppler shift applies when the relative motion between source and observer is along the direction of observation. For motion transverse to the direction of observation, a reduced Doppler shift can still be observed in the

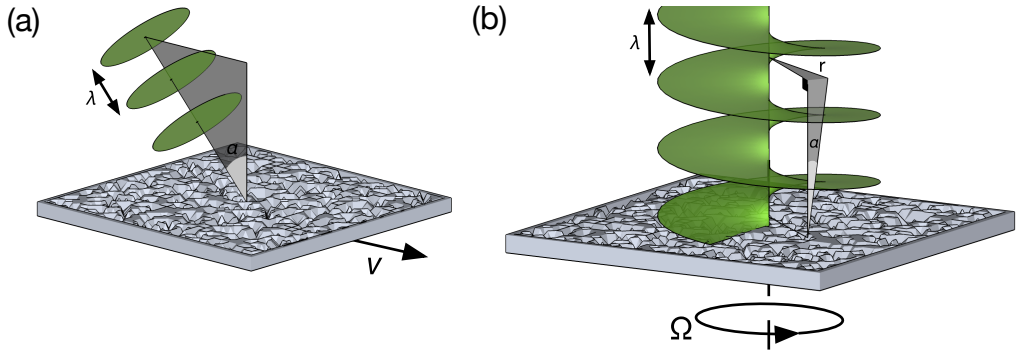


Figure 9.1: The light scattered from a moving surface can be Doppler shifted in frequency. This frequency shift can be observed for translation and, as recognised in this present work, rotation.

light scattered at an angle $\alpha$ from the surface normal. This reduced Doppler shift is given by

$$\Delta f = \sin\alpha \times f_0 \frac{v}{c}. \tag{9.2}$$

The observation of this frequency shift in light scattered from a moving object is the basis of speckle, or laser Doppler, velocimetry, and it is used for the remote sensing of the transverse velocity of moving surfaces [3] or fluids [65]. Central to many of these techniques is the illumination or viewing of the surface from two slightly different angles ($\pm\alpha$), where the frequency shift is measured between the light at these two angles (figure 9.1 (a)).

It is also possible to understand speckle velocimetry in the time domain. In illumination mode, the resulting interference between the two beams at $\pm\alpha$ creates straight-line fringes with period $\Lambda = \lambda/\sin 2\alpha$. The inhomogeneity of a rough surface moving across this fringe pattern will result in a slight modulation of the intensity of the scattered light with a frequency $f_{mod} = v/\Lambda$, which is exactly the same rate as anticipated from the differential Doppler shifts of the two beams given

by equation 9.2. The depth of the modulation depends upon the difference between the period of the fringes and the period of the surface texture, where the depth is maximised when the two periods match. These two complementary explanations of speckle velocimetry have an angular equivalent. In a helically-phased beam, the Poynting vector, and hence the optical momentum, has an azimuthal component at every position within the beam. The angle between the Poynting vector and the beam axis is $\alpha = \ell\lambda/2\pi r$, where $r$ is the radius from the beam axis (figure 9.1 (b)) [76, 96] . For a helically-phased beam illuminating a spinning object, it can be seen from equation 9.2 that the Doppler frequency shift of the on-axis scattered light is given as

$$\Delta f = \frac{\ell\lambda}{2\pi r} \times f_0 \frac{\Omega r}{c} = \frac{\ell\Omega}{2\pi}, \tag{9.3}$$

which is equivalent to equation 9.3 for linearly polarised light.

A superposition of two helically-phased beams with opposite values of $\ell$ create a beam cross-section with a modulated intensity of $2\ell$ radial petals [34]. Therefore, the intensity of the light scattered from the rough surface of a spinning disc will undergo a modulation of

$$f_{mod} = 2|\ell|\Omega/2\pi. \tag{9.4}$$

In the linear case, this modulation is the same frequency as would be observed from the interference of the two Doppler shifted components of equation 9.3. One would expect this frequency shift to be observed either in the case of illumination by a beam containing OAM and subsequent detection of scattered light, or for illumination by a plane-wave and detection of an OAM component. The experimental apparatus is shown in figure 9.2. For OAM illumination of the spinning object, a diode laser at 670 nm was coupled into a single-mode fibre, the output of was

collimated and used to illuminate a phase-only spatial light modulator (SLM). The SLM was programmed with a hologram to produce a superposition of two helically-phased beams with opposite signs of $\ell$. The phase contrast is adjusted over the SLM cross-section such that the radial intensity structure of the diffracted beam is a single annulus corresponding to a $p = 0$ Laguerre-Gaussian mode [55]. The plane of the SLM is re-imaged using an a-focal telescope to illuminate the spinning object. Relay mirrors allow the axis of the illuminating beam to be precisely aligned to the rotation axis of the object. The diameter of the beam superposition on the object is approximately 18 mm, which gives a petal period of approximately 2 mm for mode values of $\ell = \pm 18$. This petal beam illuminates a metallic surface attached to a plastic rotor, which is driven by a computer-controlled electric motor to run at speeds ranging from 200 - 500 radians per second. A lens and a large area photodiode were used collect light scattered from the metal surface. The output of the detector is digitised and Fourier-transformed to give the frequency components of the detected intensity modulation.

Figure 9.3 (b) shows the recorded modulation spectrum for the light scattered from the rotating surface when illuminated with a Laguerre-Gaussian superposition of $\ell = \pm 18$. The resulting power spectra were obtained from a data collection period of 1 second. A clearly distinguishable peak was observed at a frequency matching that predicted by equation 9.4. To further test the relationship predicted in equation 9.4, the rotation speed and value of were varied and compared to the results expected from the prediction, figure 9.3 (c).

It is interesting to note that the relative frequency shift of the +ve and -ve orbital angular momentum components gives an energy imbalance between the states, yet not necessarily a change in their angular momentum. The latter

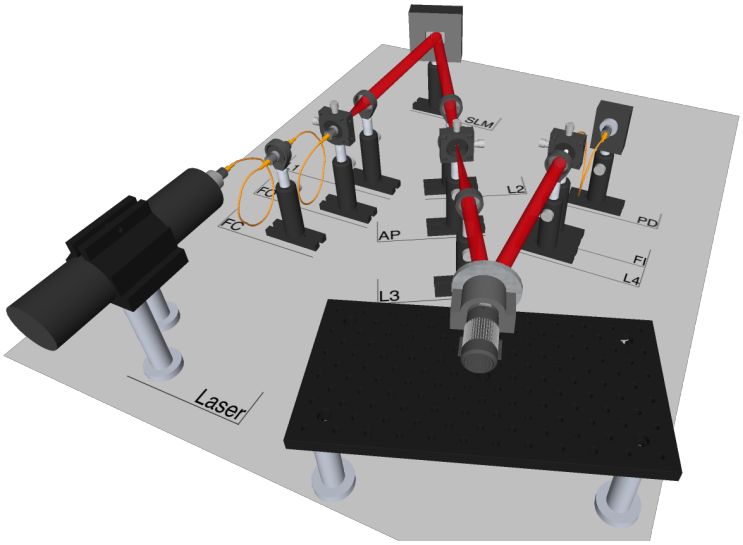


Figure 9.2: A diode laser at 670 nm is coupled into a single mode optical fibre, the output, FO, of which is collimated with a 40 mm lens, L1, and used to illuminate a spatial light modulator, SLM. The SLM is programmed to give a first-order diffracted beam, which is a superposition of opposite helically-phased beams that is selected using an aperture, AP. The plane of the SLM is re-imaged using a further lens, L3, onto the surface of the spinning disk. Light scattered from the disk is collected using a final lens, L4, and coupled into a multi-mode fibre that is connected to a photodiode, PD, where the variations in the light's intensity can be measured.

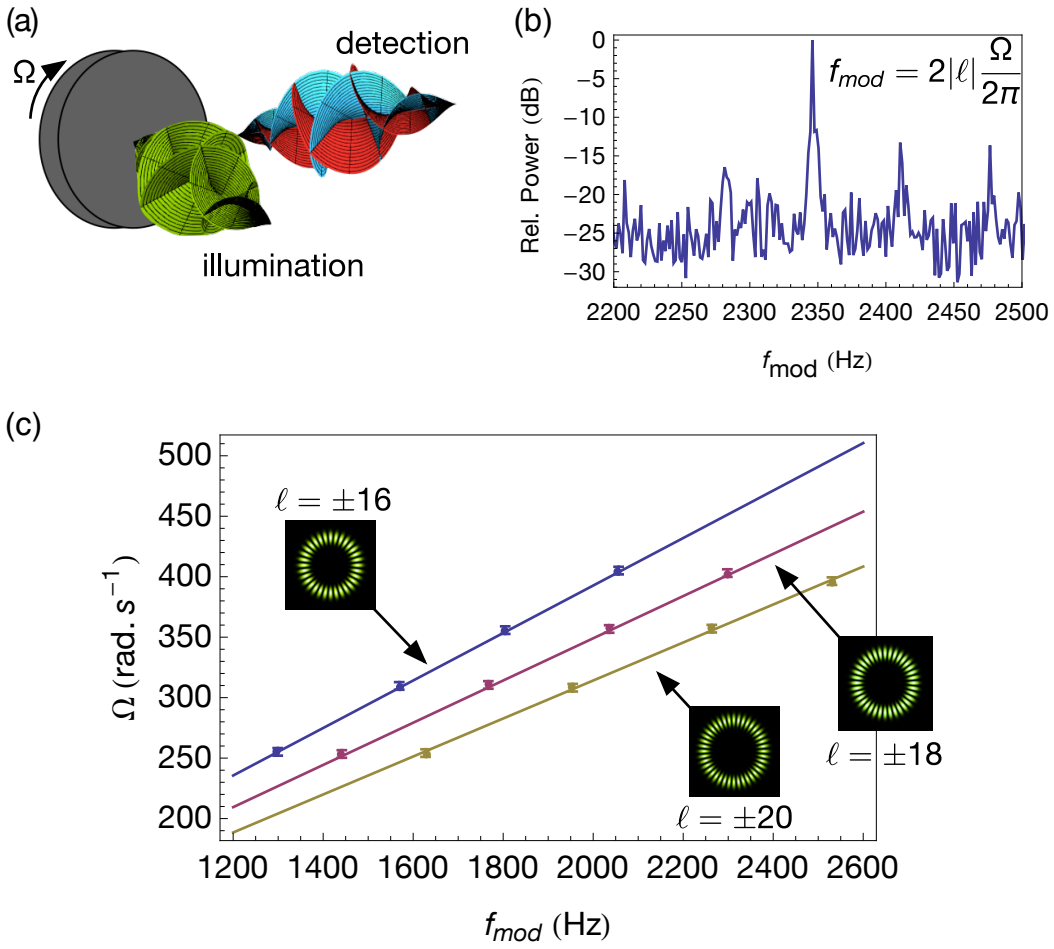


Figure 9.3: (A) A superposition of helically-phased beams with opposite signs of $\ell$ , incident on a surface rotating at a speed $\Omega$, results in a Doppler shift of the on-axis scattered light. The size of this shift is dependant on the value and sign of $\ell$ . For a given input superposition, shown in green, the light scattered from the positive $\ell$ beam will be blue-shifted and that from the negative beam will be red-shifted. (B) this differential shift will result in an intensity modulation at a particular frequency, $f_{mod}$ . (C) values of were measured for different rotation speeds $\Omega$ and values of $\ell$, shown as points, and were compared to the values predicted from equation 9.4, shown as solid lines.

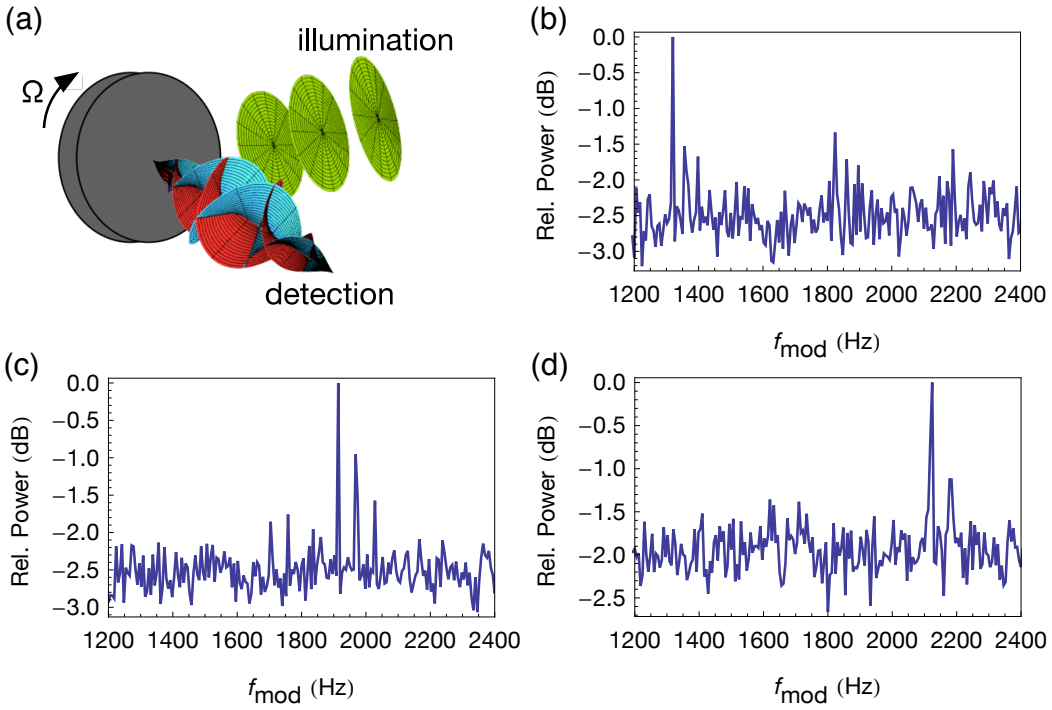


Figure 9.4: (A) light scattered from a uniformly illuminated spinning surface can be filtered to contain only specified modal components . When these components are interfered, an intensity modulation is observed. Three different rotation speeds were tested (b-d).

depends solely upon photon number in each mode, slight changes in which would not be observable in this experiment. Indeed, one would not expect the OAM to be altered by scattering from a rotating disk since the $\ell$-fold rotational symmetry of the mode remains $\ell$-fold symmetric even in a rotating frame [91].

The underlying mechanism introducing this frequency shift can be understood either with respect to the laboratory or the rotating frame. In the laboratory frame, the change in local ray direction between the incident and detected light means there is an azimuthal reaction force acting on the scattering surface. Doing work against this force is the energy-input required to shift the frequency of the light, not dissimilar in origin to the mechanism associated with the rotation of a mode converter [79]. The +ve and -ve OAM components undergo up- and down-shifts in frequency, which interfere to give the modulation in intensity recorded at the detector. In the rotating frame, the incident beams are themselves seen as rotating and hence are subject to a rotational Doppler shift, with the +ve and -ve OAM components again experiencing up- and down-shifts respectively. Scattering centres on the surface radiate both of the frequencies back to the detector, where they again interfere to give the observed modulation in intensity.

As mentioned earlier, the equivalent interpretation in terms of a Doppler shift or patterned projection applies both to OAM illumination and OAM detection. Consequently, it is possible to interchange the laser and detector. In this alternative configuration, the spinning object is illuminated directly with the expanded laser beam. Some of the scattered light is incident on the SLM, which is programmed with an identical hologram as to that used previously, to couple a superposition of $\pm\ell$ into the single-mode fibre. The SLM and the fibre are now acting as a mode filter to select only the desired superposition from the many

modes within the scattered light. The power of light in these desired modes is a small fraction of that illuminating the object, so the light transmitted through the fibre is only of low intensity. I measured the light transmitted by the using a photomultiplier, the output from which is Fourier-transformed as in the previous configuration. To enhance the signal, the metal surface was lightly embossed with a pattern of 36-fold rotational symmetry, resulting in a dominant overlap with the modal superposition of $\ell = \pm 18$ ($\Delta = 36$).

Figure 9.4 shows the frequency spectrum of the intensity modulation in the detected light as obtained over a data collection period of 5 minutes. Again the frequency of this peak can be predicted by equation 9.4 to reveal the rotational speed of the object. The subsidiary peaks at higher frequencies arise from a cross-coupling to higher mode indices that correspond to $\Delta = 37$ and $\Delta = 38$. From these results, it can be shown that an orbital angular momentum-based analysis of the scattered light makes it possible to infer the rotation speed of a distant object, even though the rotation axis is parallel to the observation direction. The high mode number of the orbital angular momentum state means that the recorded frequency is a factor of $2\ell$ higher than the rotation frequency itself. A similar advantage in using OAM has been noted previously for angle measurement in both classical [5] and quantum [32] regimes.

Although the Doppler shift, Doppler velocimetry and their application to the remote measurement of transverse velocity are well known, this is the first recognition that these phenomena have an angular equivalent. An analysis in terms of the orbital angular momentum gives a clear and intuitive understanding of the angular case. This understanding indicates possible applications in multiple regimes. Two application areas of particular promise are the potential for the remote sensing of

turbulence in back-scattered light and the possible application to astronomy for the remote detection of rotating bodies. For the case of back-scattered light, one could imagine a sensor placed on the nose of wind turbine allowing the detection of rotation within the atmosphere, allowing the turbine to prepare for potentially damaging winds. Within astronomy, many of the objects one observes are scattering objects with some simple examples being planets and asteroids. The angular form of Doppler Velocimtery could potentially be used to determine their rotations speeds based on the scattered light of these objects. While possible, such an astronomical application will likely be considerably challenging to implement.

# 10

# Conclusions

Since the original realisation, in 1992, that helically phased beams carry an orbital angular momentum (OAM), the optics community still considers the phenomenology and utilisation of OAM a hot topic [1, 103]. Researchers have continued to find novel ways to use this property of a light beam in many different research fields. The earliest use of this momentum was for the twisting of microscopic particles [43]. Soon after this early use of the orbital angular momentum content,

the helical phase structure of beams carrying OAM was seen as a useful property within microscopy, quantum optics, optical communications and potentially even astronomy [38, 62, 40, 42].

Currently, a key focus of the optics community is the use of OAM to increase the bandwidth in optical communications systems. The driving force behind my postgraduate studies has been the desire to maximise the information that can be carried by light. The issue that I aimed to tackle was the development of a simple and efficient method to measure the OAM carried by a light beam. When one starts out on a Ph.D., it begins with a question. One doesn't always realise at the begining what that question is, but I rapidly realised mine was, "How does one build a beam splitter for OAM?" In this thesis, I have outlined the achievements that I have made myself, and those made in collaboration with others, to answer this question.

Physically the closest example to a beam splitter for OAM was originally outlined by Leach *et al.*, which routes OAM to one of a number of potential output ports [58]. Chapter 3 presents an adaption of this interferometric-based method, utilising specially manufactured inverting prisms, where the optical face is perpendicular to the optic axis, right-angled prisms, as opposed to mirrors, to cycle the light around the interferometer. As the optical faces of the constituent components are parallel to each other, the components could be bonded together. Bonding the components made the system compact and robust. A realisation of each inverting prism having a specific mirror plane, around which the transverse cross section of any transmitted beam is inverted, lead to a different approach to the alignment of the system. The intersection of the mirror plane from each Dove prism defines a path an input beam is required to take for the two beams to be co-linear at the

output ports. Hence, by controlling only the input direction, the interferometer can be aligned, removing many of the previously required degrees of freedom. The routing of an OAM beam with the preservation of the helical structure is useful for data processes and transfer, as more complex operations can be carried out after the beam is routed to one of the output ports.

These interferometric sorting methods are efficient, but they are technically challenging to implement when the number of states one wishes to distinguish is large, as one requires $N-1$ interferometers to distinguish $N$ states. The complexity of many of the previously considered methods to measure OAM lead us to ask a question, "What is the simplest optical state separator we know of?" The answer? A convex lens. A convex lens will readily discriminate tilted plane-waves within direction space. Such a lens is all that is required to focus a plane-wave to a spot in its focal plane, whose transverse position depends on the transverse phase gradient of the plane-wave. The sorting of these transverse phase gradients suggests an approach for separating OAM states. Transforming the states azimuthal phase gradient, for which a change in mode index of $\Delta\ell = 1$ corresponds to an increment in phase of $2\pi$, to a transverse phase gradient where a lens can then be used to distinguished the OAM state. This transformation was achieved through the development of two bespoke diffractive optical elements, which transform the azimuthally-varying phase gradient of helically-phased beams into a beam with a transverse phase gradient. The combination of these two elements, referred to as the mode-sorter, map a point $(x, y)$ at the input plane, to a point $(u, v)$ at the output plane where $u(x, y) = -a\ln(\sqrt{x2 + y2}/b)$ and $v(x, y) = a\arctan(y)$. These transformed states are focussed onto a CCD array by a lens and, as discussed above, the lateral position of the resulting elongated spots is proportional to the

OAM state of the incident beam. However, the diffraction limit effects the efficiency of detection, as the focused spots slightly overlap for different states. Even with this limitation, this new method to distinguish between OAM modes has distinct advantages over the other commonly used methods, outlined in chapter 2.

The two bespoke diffractive optical elements had a further limitation, which was the efficiency of the SLM used to impart the required phase variation to carry out the transformation. To overcome this limitation the diffractive elements were replaced with specially manufactured refractive elements, increasing the transmission efficiency from around 25% to above 85%, making them attractive for use with single photons. An additional advantage to refractive elements was the ability to readily duplicate them and share them with collaborators. Nine institutions have started utilising this new mode sorting technique, and it is being used in a wide variety of experiments.

Early designs of the mode-sorter could efficiently distinguish OAM over a mode range of $\ell = \pm 10$. However, as $\ell$ is unbounded maximising the range over which the mode sorter works efficiently is an important goal. When beams with a high $\ell$ value were incident on the sorter there was increased crosstalk between adjacent detection modes. The mode sorter works by the first optical element introducing a spatially-dependent deviation to the ray direction, such that the ray arrives at a point on the output plane consistent with the desired transformation. This deviation is calculated assuming a ray arrives normal to the optical surface, although for beams carrying OAM with $\ell \neq 0$ this is not the case. A helical wavefront, where $\ell > 0$, results in an azimuthal component to the beam's Poynting vector. A local ray normal to this helical wavefront has a skew angle of $\ell/kr$ with respect to the beam axis where $k$ is the wavenumber and $r$ is radius where this ray is located.

Such skewed local rays result in an error in the transformation which is dependant on $\ell$. This error results in an increased spot size when the transformed modes are focused causing greater crosstalk between measured OAM modes. By increasing the deviation introduced by the first optical element, one can reduce the error introduced for a particular value of $\ell$, increasing the bandwidth over which the sorter can accurately measure the input beam's OAM spectrum. The deviation is linked with the Fresnel number of the system, and by increasing this characteristic number, the sorter has been shown to efficiently distinguish between more then 50 OAM modes.

The mode-sorter was primarily designed to distinguish between OAM modes with different $\ell$. A mode with a particular $\ell$ value can also vary in radius. With the addition of a cylindrical lens between spherical lens at the output of the sorter and the detector plane this radial component of an OAM mode can further be measured. The cylindrical lens is placed such that the $u(x, y)$ co-ordinate is imaged onto the detection plane, and radius can then be determined by the position of the focused spot along this co-ordinate.

Having developed a potential, albeit not perfect, beam splitter for OAM, such a device can be used to investigate the properties of optical beams. As such, I have presented investigations into the effects of misalignment of the optical beam with respect to a detector, and the degradation of a transmitted beam passing through atmospheric turbulence. These investigations studied two of the potential issues that would affect a real world communications channel based on OAM. The effects of both misalignment and turbulence, even at acute levels, result in a changed of the spatial profile of the light incident on one's detector causing considerable crosstalk between the measured OAM channels. Overcoming both of

these effects will be essential if OAM based communications is to become realistic option for free-space communications.

Although the use of OAM for communications has been the driving force behind much of my research, it has not been the only area of interest during my studies. In recent years, consideration has been given to the use OAM for remote sensing. The relative velocity of an object moving with respect to an observer can be readily determined by measuring the Doppler shift of light scatted from this object. However, for a wheel illuminated with a plane wave at the centre of rotation, one would see no frequency shift. Instead of plane-wave illumination, we illuminated the wheel with a beam carrying OAM, where a frequency shift of $|\ell|\Omega/2\pi$ is observed. Although Doppler shifts, Doppler velocimetry and their application to the remote measurement of transverse velocity are well known, this investigation presented the first recognition that these phenomena have an angular equivalent. This angular case has the potential for application in many regimes. Two potential applications are the remote sensing of turbulence in back-scattered light and the possible application for the remote detection of rotating bodies, in both terrestrial and astronomical settings.

The scientific community is finding uses for OAM in many area of research. During my studies I made some key developments that will hopefully lead to the wider use of OAM in, at least, the field of OAM phenomenology, optical communications and remote sensing. A question I'm often asked is, "Will we see the real-world implementation of OAM based communications links?" Unfortunately, the answer is not entirely clear. Development of methods to assure correct alignment and the mitigation of turbulence are central to success of such links. Undoubtedly research into overcoming these concerns will continue for many years and will

hopefully allow the answer to be yes. However, future research into OAM will not only focus on communications and I eagerly wait to see what new uses of OAM the optics and other scientific communities discover.

# Bibliography

[1] L Allen, M W Beijersbergen, R J C Spreeuw, and J P Woerdman. Orbital angular-momentum of light and the transformation of Laguerre-Gaussian laser modes. *Physical Review A*, 45(11):8185–8189, 1992.

[2] L Allen, M J Padgett, and M Babiker. The orbital angular momentum of light. *Progress In Optics, Vol Xxxix*, 39:291–372, 1999.

[3] T Asakura and N Takai. Dynamic laser speckles and their application to velocity measurements of the diffuse object. *Applied Physics*, 25(3):179–194, 1981.

[4] A Ashkin, J M Aziedzic, J E Bjorkholm, and S Chu. Observation of a single-beam gradient force optical trap for dielectric particles. *Optics Letters*, 11(5):288–290, 1986.

[5] S M Barnett and R Zambrini. Resolution in rotation measurements. *Journal of Modern Optics*, 53(5-6):613–625, 2006.

[6] V Y Bazhenov, M S Soskin, and M V Vasnetsov. Screw dislocations in light wave-fronts. *Journal of Modern Optics*, 39(5):985–990, 1992.

[7] J M Beckers. Adaptive Optics for Astronomy - Principles, Performance,

and Applications. *Annual Review of Astronomy and Astrophysics*, 31:13–62, 1993.

[8] M W Beijersbergen, L Allen, H E L O Vanderveen, and J P Woerdman. Astigmatic laser mode converters and transfer of orbital angular-momentum. *Optics Communications*, 96(1-3):123–132, 1993.

[9] Gregorius C G Berkhout and Marco W Beijersbergen. Method for Probing the Orbital Angular Momentum of Optical Vortices in Electromagnetic Waves from Astronomical Objects. *Physical Review Letters*, 101(10):100801, 2008.

[10] Gregorius C G Berkhout, Martin P J Lavery, Johannes Courtial, Marco W Beijersbergen, and Miles J Padgett. Efficient Sorting of Orbital Angular Momentum States of Light. *Physical Review Letters*, 105(15):153601, 2010.

[11] Gregorius C G Berkhout, Martin P J Lavery, Miles J Padgett, and Marco W Beijersbergen. Measuring orbital angular momentum superpositions of light by mode transformation. *Optics Letters*, 36(10):1863–1865, 2011.

[12] M V Berry and M R Dennis. Knotted and linked phase singularities in monochromatic waves. *Proceedings of the Royal Society of London Series A-Mathematical Physical and Engineering Sciences*, 457(2013):2251–2263, 2001.

[13] M V Berry, J F Nye, and F J Wright. The Elliptic Umbilic Diffraction Catastrophe. *Philoscophical Transactions of the Royal Society of London Series A*, 291:453–484, 1979.

[14] R A Beth. Mechanical Detection and Measurement of the Angular Momentum of Light. *Physical Review*, 50(2):115–125, 1936.

[15] I Bialynicki-Birula and Z Bialynicki-Birula. Rotational frequency shift. *Physical Review Letters*, 78(13), 1997.

[16] M Bourennane and A Karlsson. Quantum key distribution using multilevel encoding. *Physical Review A*, 64:012306, 2001.

[17] Robert W Boyd. *Nonlinear Optics; 2nd ed.* Academic Press, 2003.

[18] Nenad Bozinovic, Steven Golowich, Poul Kristensen, and Siddharth Ramachandran. Control of orbital angular momentum of light with optical fibers. *Optics Letters*, 37(13):2451–2453, 2012.

[19] O Bryndahl. Geometrical transformations in optics. *Journal of the Optical Society of America*, 64(8):1092–1099, 1974.

[20] T Čižmár and K Dholakia. Shaping the light transmission through a multimode optical fibre: complex transformation analysis and applications in biophotonics. *Optics Express*, 19(20):18871–18884, 2011.

[21] T Čižmár and K Dholakia. Exploiting multimode waveguides for pure fibre-based imaging. *Nature Communications*, 3(1027), 2012.

[22] P Coullet, L Gil, and F Rocca. Optical vortices. *Optics Communications*, 73(5):403–408, 1989.

[23] J Courtial, K Dholakia, D A Robertson, and L Allen. Measurement of the Rotational Frequency Shift Imparted to a Rotating Light Beam Possessing Orbital Angular Momentum. *Physical Review Letters*, 80, 1998.

[24] J Courtial and M J Padgett. Performance of a cylindrical lens mode converter for producing Laguerre-Gaussian laser modes. *Optics Communications*, 159:13–18, 1999.

[25] Johannes Courtial and K O'Holleran. Experiments with twisted light. *The European Physical Journal-Special Topics*, 145:35–47, 2007.

[26] Vincenzo D'Ambrosio, Eleonora Nagali, Stephen P Walborn, Leandro Aolita, Sergei Slussarenko, Lorenzo Marrucci, and Fabio Sciarrino. Complete experimental toolbox for alignment-free quantum communication. *Nature Communications*, 3:961, 2012.

[27] C G Darwin. Notes on the Theory of Radiation. *Proceedings of the Royal Society of London Series A*, 136(829):36–52, 1932.

[28] Li-Ping Deng, Haibo Wang, and Kaige Wang. Quantum CNOT gates with orbital angular momentum and polarization of single-photon quantum logic. *JOSA B*, 24(9):2517–2520, 2007.

[29] K Dholakia, N Simpson, M J Padgett, and L Allen. Second-harmonic generation and the orbital angular momentum of light. *Physical Review A*, 54(5):3742–3745, 1996.

[30] T A Dow, M H Miller, and P J Falter. Application of a fast tool servo for diamond turning of nonrotationally symmetric surfaces. *Precision Engineering*, 13(4):243–250, 1991.

[31] Angela Dudley, Michael Nock, Thomas Konrad, Filippus S Roux, and An-

drew Forbes. Amplitude damping of Laguerre-Gaussian modes. *Optics Express*, 18(22):22789–22795, 2010.

[32] R Fickler, R Lapkiewicz, W N Plick, M Krenn, C Schaeff, S Ramelow, and A Zeilinger. Quantum Entanglement of High Angular Momenta. *Science*, 338(6107):640–643, 2012.

[33] Daniel Flamm, Christian Schulze, Darryl Naidoo, Siegmund Schroter, Andrew Forbes, and Michael Duparre. All-Digital Holographic Tool for Mode Excitation and Analysis in Optical Fibers. *Journal of Lightwave Technology*, 31(7):1023–1032, 2013.

[34] S Franke-Arnold, A S Arnold, D Ellinas, J M Girkin, J Leach, V E Lembessis, P Ohberg, M J Padgett, and A J Wright. Optical ferris wheel for ultracold atoms. *Optics Express*, 15(14):8619–8625, 2007.

[35] Sonja Franke-Arnold, Stephen M Barnett, Eric Yao, Jonathan Leach, Johannes Courtial, and Miles J Padgett. Uncertainty principle for angular position and angular momentum. *New Journal of Physics*, 6:103, August 2004.

[36] D L Fried. Statistics of a Geometric Representation of Wavefront Distortion. *JOSA*, 55(11):1427–1431, 1965.

[37] M Friese, J Enger, and H Rubinsztein-Dunlop. Optical angular-momentum transfer to trapped absorbing particles. *Physical Review A*, 54(2):1593–1596, 1996.

[38] Severin Fürhapter, Alexander Jesacher, Stefan Bernet, and Monika Ritsch-Marte. Spiral phase contrast imaging in microscopy. *Optics Express*, 13(3):689–694, 2005.

[39] B A Garetz and S Arnold. Variable Frequency-Shifting of Circularly Polarized Laser-Radiation via a Rotating Half-Wave Retardation Plate. *Optics Communications*, 31(1):1–3, 1979.

[40] G Gibson, J Courtial, M J Padgett, M V Vasnetsov, V A Pas'ko, S M Barnett, and S Franke-Arnold. Free-space information transfer using light beams carrying orbital angular momentum. *Optics Express*, 12(22):5448–5456, 2004.

[41] Simon Groblacher, Thomas Jennewein, Alipasha Vaziri, Gregor Weihs, and Anton Zeilinger. Experimental quantum cryptography with qutrits. *New Journal of Physics*, 8:75, 2006.

[42] M Harwit. Photon Orbital Angular Momentum in Astrophysics. *Astrophys. J.*, 597:1266–1270, 2003.

[43] H He, M Friese, and N R Heckenberg. Direct Observation of Transfer of Angular Momentum to Absorptive Particles from a Laser Beam with a Phase Singularity. *Physical Review Letters*, 75(5), 1995.

[44] N R Heckenberg, R McDuff, C P Smith, and A G White. Generation of optical-phase singularities by computer-generated holograms. *Optics Letters*, 17(3):221–223, 1992.

[45] J M Hickmann, E J S Fonseca, W C Soares, and S Chavez-Cerda. Unveiling

a Truncated Optical Lattice Associated with a Triangular Aperture Using Light's Orbital Angular Momentum. *Physical Review Letters*, 105(5):053904, 2010.

[46] W J Hossack, A M Darling, and A Dahdouh. Coordinate transformations with multiple computer-generated optical-elements. *Journal of Modern Optics*, 34(9):1235–1250, 1987.

[47] B Jack, M J Padgett, and S Franke-Arnold. Angular diffraction. *New Journal of Physics*, 10(10):103013, 2008.

[48] Alexander Jesacher, Christian Maurer, Andreas Schwaighofer, Stefan Bernet, and Monika Ritsch-Marte. Near-perfect hologram reconstruction with a spatial light modulator. *Optics Express*, 16(4):2597–2603, 2008.

[49] E Karimi, B Piccirillo, E Nagali, and L Marrucci. Efficient generation and sorting of orbital angular momentum eigenmodes of light by thermally tuned $q$-plates. *Applied Physics Letters*, 94:231124, 2009.

[50] S N Khonina, V Kotlyar, and R Skidanov. Gauss-Laguerre modes with different indices in prescribed diffraction orders of a diffractive phase element. *Optics Communications*, 175:301–308, 2000.

[51] Martin P J Lavery, Gregorius C G Berkhout, Johannes Courtial, and Miles J Padgett. Measurement of the light orbital angular momentum spectrum using an optical geometric transformation. *Journal of Optics*, 13(6):064006, 2011.

[52] Martin P J Lavery, Angela Dudley, Andrew Forbes, Johannes Courtial, and

Miles J Padgett. Robust interferometer for the routing of light beams carrying orbital angular momentum. *New Journal of Physics*, 13(9):093014, 2011.

[53] Martin P J Lavery, David J Robertson, Gregorius C G Berkhout, Gordon D Love, Miles J Padgett, and Johannes Courtial. Refractive elements for the measurement of the orbital angular momentum of a single photon. *Optics Express*, 20(3):2110–2115, 2012.

[54] J Leach, M R Dennis, J Courtial, and M J Padgett. Laser beams: Knotted threads of darkness. *Nature*, 432(7014):165–165, 2004.

[55] J Leach, M R Dennis, J Courtial, and M J Padgett. Vortex knots in light. *New Journal of Physics*, 7(1):55, 2005.

[56] J Leach, B Jack, J Romero, M Ritsch-Marte, Robert W Boyd, A K Jha, S M Barnett, S Franke-Arnold, and M J Padgett. Violation of a Bell inequality in two-dimensional orbital angular momentum state-spaces. *Optics Express*, 17(10):8287–8293, 2009.

[57] J Leach, S Keen, M J Padgett, C Saunter, and G D Love. Direct measurement of the skew angle of the Poynting vector in a helically phased beam. *Optics Express*, 14(25):11919–11924, 2006.

[58] J Leach, M J Padgett, S M Barnett, S Franke-Arnold, and J Courtial. Measuring the orbital angular momentum of a single photon. *Physical Review Letters*, 88(25), 2002.

[59] Y Liu. Measuring the orbital angular momentum of elliptical vortex beams

by using a slit hexagon aperture. *Optics Communications*, 284:2424–2429, 2011.

[60] W Löffler, T Euser, E R Eliel, M Scharrer, P Russell, and J P Woerdman. Fiber Transport of Spatially Entangled Photons. *Physical Review Letters*, 106(24), June 2011.

[61] A Mair, A Vaziri, G Weihs, and A Zeilinger. Entanglement of the orbital angular momentum states of photons. *Nature*, 412(6844):313–316, 2001.

[62] A Mair, A Vaziri, G Weihs, and A Zeilinger. Multi dimensional Photon Entanglement of Quantum States with Phase Singularities. *Nature*, 412(315), 2001.

[63] Mehul Malik, Malcolm O'Sullivan, Brandon Rodenburg, Mohammad Mirhosseini, Jonathan Leach, Martin P J Lavery, Miles J Padgett, and Robert W Boyd. Influence of atmospheric turbulence on optical communications using orbital angular momentum for encoding. *Optics Express*, 20(12):13195–13200, 2012.

[64] J C Maxwell. A Dynamical Theory of the Electromagnetic Field . *Philosophical Transactions of the Royal Society of London*, 155:459–512, 1865.

[65] Roland Meynart. Instantaneous velocity field measurements in unsteady gas flow by speckle velocimetry. *Applied Optics*, 22(4):535–540, 1983.

[66] A A Michelson. Measurement of the velocity of light between Mount Wilson and Mount San Antonio. *The Astrophysical Journal*, 65(1), 1927.

[67] Gabriel Molina-Terriza, Liis Rebane, Juan P Torres, Lluis Torner, and Silvia Carrasco. Probing canonical geometrical objects by digital spiral imaging. *Journal of the European Optical Society-Rapid Publications*, 2:07014, 2007.

[68] A Mourka, J Baumgartl, C Shanor, K Dholakia, and E M Wright. Visualization of the birth of an optical vortex using diffraction from a triangular aperture. *Optics Express*, 19(7):5760–5771, 2011.

[69] A Mourka, M Mazilu, E M Wright, and K Dholakia. Modal Characterization using Principal Component Analysis: application to Bessel, higher-order Gaussian beams and their superposition. *Scientific Reports*, 3(1422), March 2013.

[70] G Nienhuis. Doppler effect induced by rotating lenses. *Optics Communications*, 132:8–14, 1996.

[71] J F Nye and M V Berry. Dislocations in Wave Trains. *Proceedings of the Royal Society of London Series A-Mathematical Physical and Engineering Sciences*, 336(1605):165–190, 1974.

[72] J L O'Brien, G J Pryde, A Gilchrist, and D F V James. Quantum Process Tomography of a Controlled-NOT Gate. *Physical Review Letters*, 93(8):080502, 2004.

[73] Kevin O'Holleran, Mark R Dennis, Florian Flossmann, and Miles J Padgett. Fractality of light's darkness. *Physical Review Letters*, 100(5):053902, 2008.

[74] Kevin O'Holleran, Mark R Dennis, and Miles J Padgett. Topology of Light's Darkness. *Physical Review Letters*, 102(14):143902, 2009.

[75] Kevin O'Holleran, Miles J Padgett, and Mark R Dennis. Topology of optical vortex lines formed by the interference of three, four, and five plane waves. *Optics Express*, 14(7):3039–3044, 2006.

[76] M J Padgett. The Poynting vector in Laguerre-Gaussian laser modes. *Optics Communications*, 121:36–40, 1995.

[77] M J Padgett, J Arlt, N Simpson, and Les Allen. An experiment to observe the intensity and phase structure of Laguerre-Gaussian laser modes. *American Journal of Physics*, 64(1):77–82, 1996.

[78] M J Padgett and Johannes Courtial. Poincare-sphere equivalent for light beams containing orbital angular momentum. *Optics Letters*, 24(7):430–432, 1999.

[79] Miles J Padgett. The mechanism for energy transfer in the rotational frequency shift of a light beam. *J. Opt. A: Pure Appl. Opt*, 6(5):S263–S265, April 2004.

[80] C Paterson. Atmospheric Turbulence and Orbital Angular Momentum of Single Photons for Optical Communication. *Physical Review Letters*, 94:153901, 2005.

[81] Bart-Jan Pors, C. H. Monken, Eric R. Eliel, and J P Woerdman. Transport of Orbital-Angular-Momentum Entanglement through a Turbulent Atmosphere. *Optics Express*, 19(7):6671–6683, 2009.

[82] J H Poynting. On the Transfer of Energy in the Electromagnetic Field.

*Philosophical Transactions of the Royal Society of London*, 175:343–361, 1884.

[83] J H Poynting. The wave motion of a revolving shaft, and a suggestion as to the angular momentum in a beam of circularly polarised light. *Proceedings if the Royal Society of London Series A-Containing Papers of A Mathematical and Physical Character*, 82(557):560–567, 1909.

[84] Brandon Rodenburg, Martin P J Lavery, Mehul Malik, Malcolm N O'Sullivan, Mohammad Mirhosseini, David J Robertson, Miles J Padgett, and Robert W Boyd. Influence of atmospheric turbulence on states of light carrying orbital angular momentum. *Optics Letters*, 37(17):3736–3737, 2012.

[85] J Romero, J Leach, B Jack, S M Barnett, M J Padgett, and S Franke-Arnold. Violation of Leggett inequalities in orbital angular momentum subspaces. *New Journal of Physics*, 12:123007, December 2010.

[86] Y Saito, S Komatsu, and H Ohzu. Scale and rotation invariant real-time optical correlator using computer generated hologram. *Optics Communications*, 47(1):8–11, 1983.

[87] C E Shannon. A mathematical theory of communication. *Bell Systems Technology Journal*, 27:623–656, 1948.

[88] N B Simpson, Les Allen, and M J Padgett. Optical tweezers and optical spanners with Laguerre-Gaussian modes. *Journal of Modern Optics*, 43(12):2485–2491, 1996.

[89] S Slussarenko, V D'Ambrosio, B Piccirillo, L Marrucci, and E Santamato. The Polarizing Sagnac Interferometer: a tool for light orbital angular momentum sorting and spin-orbit photon processing. *Optics Express*, 18(26):27205–27216, December 2010.

[90] M S Soskin, V N Gorshkov, M V Vasnetsov, J T Malos, and N R Heckenberg. Topological charge and angular momentum of light beams carrying optical vortices. *Physical Review A*, 56(5):4064–4075, 1997.

[91] Fiona Speirits, Martin P J Lavery, Miles J Padgett, and Stephen M Barnett. Optical Angular Momentum in a Rotating Frame. *In preperation.*

[92] Grover A Swartzlander, Jr, Erin L Ford, Rukiah S Abdul-Malik, Laird M Close, Mary A Peters, David M Palacios, and Daniel W Wilson. Astronomical demonstration of an optical vortex coronagraph. *Optics Express*, 16(14):10200–10207, 2008.

[93] Fabrizio Tamburini, Elettra Mari, Anna Sponselli, Bo Thide, Antonio Bianchini, and Filippo Romanato. Encoding many channels on the same frequency through radio vorticity: first experimental test. *New Journal of Physics*, 14(3):033001, 2012.

[94] V I Tatarski. Wave Propagation in a Turbulent Medium. McGraw-Hill, New York, 1961.

[95] L Torner, J P Torres, and S Carrasco. Digital spiral imaging. *Optics Express*, 13(3):873–881, 2005.

[96] G A Turnbull, D A Robertson, G M Smith, Les Allen, and M J Padgett.

The generation of free-space Laguerre-Gaussian modes at millimetre-wave frequencies by use of a spiral phaseplate. *Optics Communications*, 127(4-6):183–188, 1996.

[97] Glenn A Tyler and Robert W Boyd. Influence of atmospheric turbulence on the propagation of quantum states of light carrying orbital angular momentum. *Optics Letters*, 34(2):142–144, 2009.

[98] M V Vasnetsov, V A Pas'ko, and M S Soskin. Analysis of orbital angular momentum of a misaligned optical beam. *New Journal of Physics*, 7:46, 2005.

[99] Jian Wang, Jeng-Yuan Yang, Irfan M Fazal, Nisar Ahmed, Yan Yan, Hao Huang, Yongxiong Ren, Yang Yue, Samuel Dolinar, Moshe Tur, and Alan E Willner. Terabit free-space data transmission employing orbital angular momentum multiplexing. *Nature Photonics*, 6(7):488–496, 2012.

[100] N Wiener and I Extrapolation. Extrapolation, Interpolation, and Smoothing of Stationary Time Series. New York: Wiley, 1949.

[101] Max Born Emil Wolf. *Principles of Optics: Electromagnetic Theory of Propagation, Interference and Diffraction of Light, Fourth Edition.* Pergamon Press, 3rd edition, 1965.

[102] X Xue, HQ Wei, and A G Kirk. Beam analysis by fractional Fourier transform. *Optics Letters*, 26(22):1746–1748, 2001.

[103] Alison Yao and Miles J Padgett. Orbital angular momentum: origins, be-

haviour and applications. *Advances in Optics and Photonics*, 3(2):161–204, 2011.